Ab-initio description of charge, heat and thermoelectric transport in molecular junctions

Zur Erlangung des akademischen Grades eines
DOKTORS DER NATURWISSENSCHAFTEN
von der Fakultät für Physik des
Karlsruher Instituts für Technologie (KIT)

genehmigte

DISSERTATION

von

Dipl.-Phys. Thomas Julian Hellmuth

aus Konstanz

Datum der mündlichen Prüfung:	12. Dezember 2014
Referent:	Jun.-Prof. Dr. Fabian Pauly
Korreferent:	Prof. Dr. Gerd Schön

Contents

1 Introduction

With the development of the scanning tunneling microscope (STM) in 1982 [1], and the atomic force microscope (AFM) in 1986 [2], the idea to probe single molecules electrically and mechanically turned to an achievable goal. Already ten years earlier the theoretical concepts were developed, Aviram and Rathner proposed a molecular diode [3]. That diode should mimic the semiconductor p-n junction and substituent groups were used to withdraw (n doped) or accept (p doped) electrons of the molecular π-system [3].

But before single molecule functionalities could be probed, first the more stable metallic atomic-size contacts were formed [4]. Here it was found, that with increasing distance between the two gold electrodes, the conductance decreases stepwise and is further given by multiples of the conductance quantum $G_0 = 2e^2/h$. Rubio et al. [4] used an AFM to measure the force which is necessary to break a contact. They found this force to be 1.5 nN, for junctions which showed a conductance of $1G_0$. A combination of conductance measurements and transmission electron microscopy allowed to produce images of the contact configuration of a atomic contact [5, 6]. The electron microscope image in Fig. 1.1 (a) shows a configuration where an atomic gold chain connects the electrodes.

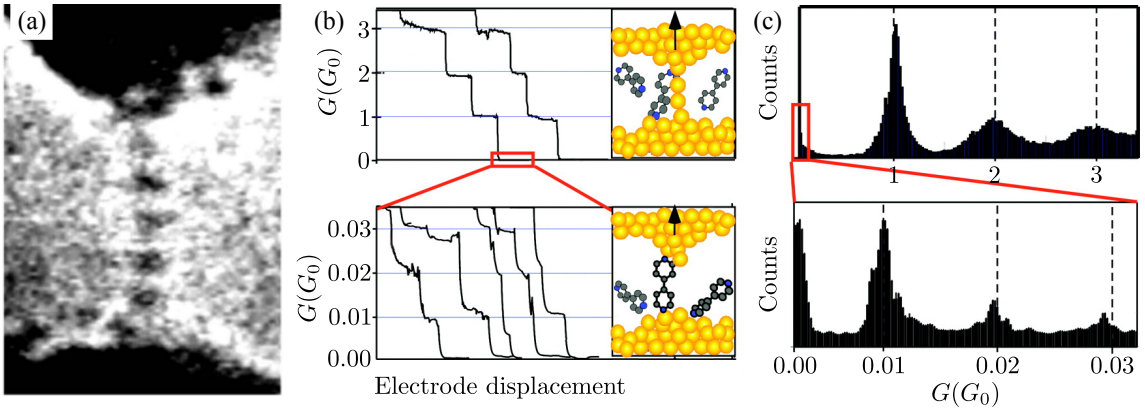

Figure 1.1: (a) Electron microscope image of a gold chain [6]. (b) Conductance as a function of the electrode displacement for a gold contact (top) and molecular junction (below). The corresponding junction geometry is shown on the right. (c) Conductance histograms that are constructed from several conductance measurements as shown in (b). (b,c) From Ref. [7] with slight modifications.

A significant part of the work, attempting to measure the conductance of a single molecule, was performed using a more stable mechanically controlled break junction (MCBJ) setup [8]. The stability of this device allowed the measurements to be carried out at room temperature. The MCBJ setup consists of a flexible substrate which serves as platform for two electrodes [9]. Those electrodes are mounted in such a way that their distance can be controlled by bending the substrate. To measure the conductance of a single molecule it is necessary to attach electrodes to that particular molecule. In this way it is possible to form the intended junction geometry, as shown in Fig. 1.1 (b). The challenge here is to synthesize anchor groups which establish the molecule-metal bond. Molecules equipped with those functional groups form self-assembled monolayers on a metallic surface.

In addition, the conductance of single molecules was measured using a STM setup as well [7]. One advantage of the STM setup is the low thermal contact between tip and substrate. Therefore it was possible to impose a temperature gradient across the molecule and measure the thermoelectric response [10]. In particular the Seebeck coefficient of a single molecule was measured. Originally the measurement of the Seebeck coefficient was performed to clarify the level alignment of the molecular orbitals with respect to the Fermi energy of the electrodes. Here a positive Seebeck coefficient corresponds to p-type (hole) charge carriers, so the transport mechanism is governed by the occupied molecular orbitals and vice versa. Already at this early stage the possibility of molecular thermoelectric energy conversion was pointed out [10]. Nowadays many research groups focus on the heat transport properties of molecular junctions. The efficiency of a thermoelectric device is characterized by the so-called figure of merit $ZT = S^2GT/\kappa$. To gain high yield from an energy converter, it is desirable to maximize ZT. Therefore materials have to be designed to show a high Seebeck coefficient S, a high electric conductance G but low thermal conductance κ. The heat conductance due to the electronic system is approximately given by the Wiedemann-Franz law. However, what is mostly neglected is the contribution to the heat conductance that originates from phonons.

In modern electronic devices it is important to control the heat flow on the nanoscale. Here it is crucial to remove the heat from the operating parts to maintain functionality. The local heating of a device can be probed using a STM equipped with a nanoscale thermocouple at its tip. With such a setup the local heat dissipation in the STM tip connected to single-molecule junctions was probed [11].

But despite of all these achievements, single molecule experiments suffer from the uncertainty that there is no direct way to explicitly determine the atomistic junction geometry. In case of the atomic size contacts it was possible to obtain electron microscope images of the contact, as shown in Fig. 1.1 (a). The conductance of a single-molecule junction is obtained by a statistical analysis of the measurements. For that reason the conductance is measured as a function of the electrode displacement, as shown in Fig. 1.1 (b). These measurements are summarized in conductance histograms as shown in Fig. 1.1 (c). The peak in the conductance histogram with the lowest conductance values is regarded as the single molecule conductance. After the single molecule conductance is found it is possible to stop the electrode displacement if that specific conductance is measured. Under the assumption that the conductance value corresponds to a unique junction geometry, it is possible to access the current voltage characteristic of a single molecule contact. To gain more insight into this particular issue combined efforts from theory and experiment are needed. First principles calculations are performed to shed more light on the properties of the metal-molecule interface as well as on the geometrical configuration of molecular junctions.

Outline

The thesis is divided into two major parts. These start after we give a short introduction to the methods which were used to describe electronic as well as phononic properties of the molecular junctions. Part I is devoted to our investigations on the electric properties of molecular junctions. During my work I used the schemes developed by Fabian Pauly for the elastic electron transport [12] as well as the inelastic electron tunneling spectrum calculations by Marius Bürkle and Janne Viljas [13, 14]. Part II focuses on the heat transport properties of molecular junctions. At the end the reader finds a summary of the presented work.

Discussing the electric properties of molecular junctions in Part I, we focus first on two anchor groups commonly used to establish the molecule-metal bond. Namely we focus on amine and thiol terminated octane molecules in Chap. 3. Motivated by measurements in the group of Prof. Scheer in Konstanz, we simulate the stretching of the molecular junctions. We calculate the mechanical stability, the conductance properties as well as the inelastic electron tunnel spectra of the molecular junctions. Next in Chap. 4 we investigate the elastic and inelastic transport properties of π-stacked molecules. In particular we use paracyclophane molecules, whose unique geometry is exploited to analyze π stacking. These molecules consist of benzene fragments whose distance is fixed by a scaffold constructed by ethane chains. The fact that those molecules bind to the electrodes directly via their π electrons deserves special attention. In Chap. 5 we analyze the properties of the inelastic electron tunneling spectra, for molecular junctions that show the destructive quantum interference. It leads to a suppressed elastic conductance, and we study the effect of electro-phonon-interaction on the conductance. We close the first part with Chap. 6, where we focus on the crossover from coherent to incoherent transport as the molecular length increases. Here we investigate polymers of different length and include decoherence by adding Büttiker probes.

In Part II we analyze the heat and thermoelectric transport through molecular junctions. In Chap. 7 we present our scheme which is used to calculate the phonon mediated heat transport. For that purpose we determine the phonon structure using density functional theory. That is the same level of theory, that was employed before, to obtain the electronic structure. Furthermore, we discuss the heat transport through atomic gold chains and compare our findings to a model that considers nearest neighbor interactions realized by spring constants. The focus turns to molecular junctions in Chap. 8, again. Here, we analyze the heat conductance of π-stacked molecular systems. We compare the phonon mediated heat transport to the contributions from electrons. Later we provide an estimate for the efficiency of the thermoelectric energy conversion using these molecules as material. Benzene derivatives are also considered in this context, in Chap. 9. Our focus in the latter studies is more on the influence of mechanical stress on the transport properties.

List of publications

Regular articles

- *Influence of vibrations on electron transport through nanoscale contacts*, M. Bürkle, J. K. Viljas, T. J. Hellmuth, E. Scheer, F. Weigend, G. Schön and F. Pauly, Phys. Status Solidi B **250**, 2468 (2013)

- *Charge Transport Characteristics of Diarylethene Photo-Switching Single-Molecule Devices*, Y. Kim, T. J. Hellmuth, D. Sysoiev, F. Pauly, T. Pietsch, J. Wolf, A. Erbe, T. Huhn, U. Groth, U. E. Steiner and E. Scheer, Nano Lett. **12**, 3736 (2012)

- *Characteristics of amine-ended and thiol-ended alkane single-molecule junctions revealed by inelastic electron tunneling spectroscopy*, Y. Kim, T. J. Hellmuth, M. Bürkle, F. Pauly and E. Scheer, ACS Nano **5**, 4104 (2011)

In preparation (draft available):

- *Elastic and inelastic charge transport through paracyclophanes*, T. J. Hellmuth, M. Bürkle and F. Pauly

- *Influence of dephasing on the conductance and thermopower of molecular wires*, F. Rochau, M. Kotiuga, T. J. Hellmuth, J.B. Neaton and F. Pauly

- *Thermoelectric transport through [2,2]paracyclophane-based single molecule junctions from first principles*, M. Bürkle, T. J. Hellmuth, F. Pauly and Y. Asai

Further plans:

- *Inelastic electron tunneling spectra in molecular junctions showing destructive quantum interference*, T. Novotny, T. J. Hellmuth, M. Bürkle and F. Pauly

- *Heat transport through 1,4-benzenedinitrile and 1,4-benzenediamine*, T. J. Hellmuth and F. Pauly

Acknowledgements

First, I would like to thank Fabian Pauly and Gerd Schön for offering me a PhD position. Without their support this thesis would not exist. I hope I was a good student.

I'm very thankful for all the opportunities and for all the support I received during the last years. I had the opportunities to visit numerous conferences and workshops.

Very important for this work was that I could visit Marius Bürkle at the National Institute of Advanced Industrial Science and Technology in Japan. He helped me in various ways.

I would like to thank also Tomáš Novotný for fruitful collaborations. We worked together on the quantum interference effect in molecular electronics.

I'm very thankful that I could work at the Institut für Theoretische Festkörperphysik and that I was always welcome in Konstanz at the Theory of Nanostructures Group.

Additionally I'm very glad that I could discuss with Andreas Heimes.

On the financial side, I acknowledge support from the Karlsruhe House of Young Scientists for my stay in Japan.

2 Concepts of molecular electronics

This chapter provides a short introduction to the fundamental concepts and methods used by our investigations in the field of molecular electronics. Here we give a summary of the basic schemes which were also discussed in several text books [15–21]. The system that we like to understand is a molecular junction. It consists of a molecule that is attached to two metal leads. The spatial configuration can be described by an electrode-molecule-electrode geometry. In the following we use ab-initio methods to describe the electronic as well as the phononic structure on the atomic scale.

We begin our discussion with the time-independent Schrödinger equation. To describe N electrons at the positions $\vec{r}_j$ and M nuclei at positions $\vec{R}_A$ in the infinite system the Schrödinger equation is:

$$\hat{H}\Psi_i\left(\vec{r}_1,\ldots,\vec{r}_N,\vec{R}_1,\ldots,\vec{R}_M\right) = E_i\Psi_i\left(\vec{r}_1,\ldots,\vec{r}_N,\vec{R}_1,\ldots,\vec{R}_M\right). \tag{2.1}$$

The Hamilton operator $\hat{H}$ contains five parts. The kinetic energy of the electrons $\hat{T}_e$, the kinetic energy of the nuclei $\hat{T}_n$, the Coulomb energy of the electrons $\hat{V}_e$, the Coulomb energy of the nuclei $\hat{V}_n$ and the Coulomb energy of nuclei and electrons $\hat{V}_{n-e}$. In atomic units the Hamiltonian is:

$$\hat{H} = \underbrace{\underbrace{-\sum_{j=1}^{N}\frac{\nabla_j^2}{2}}_{=T_e} \underbrace{-\sum_{A=1}^{M}\frac{\nabla_A^2}{2M_A}}_{T_n}}_{\text{kinetic energy}} + \underbrace{\underbrace{\sum_{j<k}^{N}\frac{1}{|\vec{r}_j-\vec{r}_k|}}_{V_e} + \underbrace{\sum_{A<B}^{M}\frac{Z_A Z_B}{\left|\vec{R}_A-\vec{R}_B\right|}}_{V_n} \underbrace{-\sum_{j=1}^{N}\sum_{A=1}^{M}\frac{Z_A}{\left|\vec{r}_j-\vec{R}_A\right|}}_{V_{n-e}}}_{\text{potential energy}}. \tag{2.2}$$

The operator $\nabla_{j/A}$ is the gradient with respect to the coordinate of electron j or the coordinate of the nucleus A. The mass of nucleus A is M_A and the corresponding charge is Z_A. As we will see in the next chapters there are some approximations and schemes to treat Eq. (2.1) as accurately and fast as possible.

Born Oppenheimer approximation

To separate the degrees of freedom of nuclear and electronic movement we use the Born-Oppenheimer approximation as explained in Refs. [22]. The idea is that the faster and lighter weighted electrons follow the much heavier nuclei on a short timescale. Therefore the motion of the electrons is calculated first treating the position of the nuclei as con-

stant. To treat that in a mathematical language we consider the wavefunction as a product of a part $\Psi_e^{(i)}$ describing the electrons and a part $\Phi_n^{(i)}$ describing the nuclei

$$\Psi_i\left(\vec{r}_1,\ldots,\vec{r}_N,\vec{R}_1,\ldots,\vec{R}_M\right)=\Phi_n^{(i)}\left(\vec{R}_1,\ldots,\vec{R}_M\right)\Psi_e^{(i)}\left(\vec{r}_1,\ldots,\vec{r}_N;\vec{R}_1,\ldots,\vec{R}_M\right). \tag{2.3}$$

With that ansatz it is possible to obtain a Schrödinger equation describing electrons and one that only treats the nuclear degree of freedom. The electronic part is:

$$\left[\sum_{j=1}^{N}\frac{\nabla_j^2}{2m_e}+\sum_{j<k}^{N}\frac{1}{|\vec{r}_j-\vec{r}_k|}-\sum_{j=1}^{N}\underbrace{\sum_{A=1}^{M}\frac{Z_A}{\left|\vec{r}_j-\vec{R}_A\right|}}_{V_{\text{ext}}(\vec{r}_j)}\right]\Psi_e^{(i)}=E_e^{(i)}(\vec{R}_1\cdots,\vec{R}_M)\Psi_e^{(i)}, \tag{2.4}$$

Here it is worth to mention that the electronic properties still depend on the position of the nuclei, but not on their dynamics. The language is such that the electronic properties depend parametrically on the position of the nuclei. The Coulomb potential, that describes the interaction of electrons and nuclei, is thus considered as an external potential $V\left(\vec{R}_1,\ldots,\vec{R}_M\right)$ of charges at fixed positions.

The nuclei follow:

$$\left[\sum_{A=1}^{M}\frac{\vec{P}_A^2}{2M_A}+\sum_{A<B}^{M}\frac{Z_AZ_B}{\left|\vec{R}_A-\vec{R}_B\right|}+E_e^{(i)}(\vec{R}_1\cdots,\vec{R}_M)\right]\Phi_n^{(i)}=H_n\Phi_n^i=E_n^{(i)}\Phi_n^{(i)}. \tag{2.5}$$

Here the interaction between nuclei is changed by the electrons and forms a effective potential V.

Here we used the approximation that the term, which couples Eq. (2.4) and Eq. (2.5):

$$\sum_{A=1}^{M}\frac{1}{2M_A}\left[\Phi_n\vec{P}_A^2\Psi_e+2\left(\vec{P}_A\Phi_n\right)\left(\vec{P}_A\Psi_e\right)\right], \tag{2.6}$$

can be neglected.

2.1 Density functional theory

In this section we briefly introduce density functional theory (DFT) following closely Ref. [16]. This method is widely used to calculate an approximate solution for the ground state of the electronic Schrödinger equation given in Eq. (2.4). But its fundamental concepts, the two Hohenberg-Kohn (HK) Theorems [17], are applied in a broader context. We only give a motivation for the HK Theorems. The interested reader finds their proofs in the literature [18–21].

Hohenberg-Kohn Theorem 1

The external potential $V_{ext}(\vec{r})$ is a unique functional of $n\left(\vec{r}\right)$, apart from a trivial additive constant.

The electron density of the ground state is given by:

$$n\left(\vec{r}\right)=N\int \mathrm{d}\vec{r}_2\cdots\mathrm{d}\vec{r}_N\left|\Psi_e^{(0)}\left(\vec{r},\vec{r}_2,\ldots,\vec{r}_N\right)\right|^2 \tag{2.7}$$

Here and in the following we omit the dependence of the electronic ground state wave function $\Psi_e^{(0)}$ on the core positions $\vec{R}_A$.

To extract from $n(\vec{r})$ the potential $V_{ext}(\vec{r})$ we need the charge and the position of the nuclei as well as the number of electrons in the system. The number of electrons is determined by the norm of the electron density. Both the charge and the position of the nuclei can be extracted from $n(\vec{r})$ due to the cup condition at the core position in $n(\vec{r})$ [23], in principle. If we can write down the external potential $V_{\text{ext}}(\vec{r})$, we know the entire Hamiltonian of the system and therefore we might be able to solve the Schrödinger equation. Theoretically that scheme allows to determine all properties of the electron system from the solution of the Schrödinger equation. In the density functional theory we then restrict ourselves to determine the ground state energy E_0. The just described scheme is often illustrated by:

$$n(\vec{r}) \Rightarrow \left\{\vec{R}_A, Z_A, N\right\} \Rightarrow V_{\text{ext}}(\vec{r}) \Rightarrow \hat{H} \Rightarrow E_0 \tag{2.8}$$

So the ground state energy is given as a functional of the ground state electron density $E_0 = E[n(\vec{r})]$.

Hohenberg-Kohn Theorem 2

The functional that delivers the ground state energy is minimized by the ground state electron density.

$$E_0 \leq E[\tilde{n}(\vec{r})] \tag{2.9}$$

The second HK theorem gives us a tool to search for the ground state electron density by minimizing the energy functional that is assumed to be known. So it is possible to invert the scheme from Eq. (2.8) and therefore we have a bijective map:

$$n(\vec{r}) \Leftrightarrow E_0. \tag{2.10}$$

Kohn-Sham Approach

The basic idea leading to the Kohn-Sham (KS) equations is to approximate the kinetic energy of the interacting electrons by the kinetic energy of a system formed from noninteracting particle. Therewith it is possible to obtain one fraction of the energy functional within an iterative scheme described in the following.

We can write the energy functional as:

$$E[n] = T_s[n] + \frac{1}{2}\int \mathrm{d}\vec{r}\int \mathrm{d}\vec{r}'\frac{n(\vec{r})\,n(\vec{r}')}{|\vec{r}-\vec{r}'|} + \int \mathrm{d}\vec{r} n(\vec{r})\,V_{\text{ext}}(\vec{r}) + E_{xc}[n] \tag{2.11}$$

Here $T_s[n]$ is the kinetic energy of the noninteracting electrons. The second term is the classical Coulomb interaction of the electrons and the third is the Coulomb interaction of the electrons with the nuclei. Everything we do not know is absorbed in the exchange-correlation functional $E_{xc}[n]$.

The KS wave functions $\phi_i(\vec{r})$ are the solutions of the one electron Schrödinger equation

$$\underbrace{\left(-\frac{\hbar^2}{2m_e}\nabla^2 + V_{\text{eff}}(\vec{r})\right)}_{=F_{\text{KS}}}\phi_i(\vec{r}) = \epsilon_i\phi_i(\vec{r})\,. \tag{2.12}$$

That equation describes noninteracting electrons. The effective external potential V_{eff} is fixed by demanding that the ground state electron density of the interacting system coincides with the ground state density of the KS system (i.e. a noninteracting electron system).

To calculate the ground state density of the KS system we sum over the occupied KS orbitals - the first N orbitals with the lowest KS energies ϵ_i

$$n\left(\vec{r}\right) = \sum_{i}^{N} \left|\phi_i\left(\vec{r}\right)\right|^2 . \tag{2.13}$$

We insert that expression in the energy functional. Using a Lagrange multiplier it is ensured that the KS orbitals are orthonormal and the Euler-Lagrange equations give an expression for the effective potential $V_{\text{eff}}\left(\vec{r}\right)$

$$V_{\text{eff}}\left(\vec{r}\right) = \frac{\delta E_{xc}\left[n\left(\vec{r}\right)\right]}{\delta n\left(\vec{r}\right)} + \sum_{i}^{N} \int \mathrm{d}\vec{r}_1 \frac{\left|\phi_i\left(\vec{r}_1\right)\right|^2}{\left|\vec{r}_1 - \vec{r}\right|} + V_{\text{ext}}\left(\vec{r}\right). \tag{2.14}$$

The first part is called the exchange-correlation potential V_{xc}. Because the effective potential depends on the KS orbitals, the solution can only be found self-consistently.

The KS scheme provides an approximation to the kinetic energy of the interacting electron system. But the left-over, unknown terms are just duped into the exchange correlation part E_{xc} of the functional. Practical applications need some approximation for E_{xc}. The most widely used approximations are called the local density approximation (LDA) and the generalized gradient approximation (GGA) functionals.

Local basis functions

To solve the KS equations it is convenient to introduce a set of local basis functions $\{\varphi_\mu\}$. We expand the KS-Orbitals in this set of functions

$$\phi_i\left(\vec{r}\right) = \sum_{\mu}^{L} c_{\mu i} \varphi_\mu\left(\vec{r}\right), \tag{2.15}$$

In our case those φ_μ are Gauss functions as implemented in TURBOMOLE [24]. These functions approximate the orbitals known from the hydrogen atom. Practically the benefit of this choice is that integrals of Gauss functions have an analytic solution. Clearly the prize is that the basis set is not orthogonal and the overlap matrix

$$S_{\mu\nu} = \int \mathrm{d}\vec{r} \varphi_\mu\left(\vec{r}\right) \varphi_\nu\left(\vec{r}\right). \tag{2.16}$$

is in general not diagonal. If we expand the molecular orbitals ϕ_i in terms of the local basis functions φ_μ, we can write the KS equations (see Eq. (2.12)) as

$$\sum_{\nu}^{L} \left(F_{\mu\nu} - \epsilon_i S_{\mu\nu}\right) c_{\nu i} = 0, \tag{2.17}$$

where the Kohn-Sham matrix is

$$F_{\mu\nu} = \int \mathrm{d}\vec{r} \varphi_\mu\left(\vec{r}\right) F_{\text{KS}} \varphi_\nu\left(\vec{r}\right). \tag{2.18}$$

Gradients of the total energy

Within DFT it is also possible to predict the structure of molecules. Therefore it is necessary to find the spacial arrangement of the nuclei with the lowest total energy E (including nucleus-nucleus Coulomb interactions). Usually the (local) minimum is found by shifting the atoms along the gradients of E and calculating the total energy of the new geometry again. This iterative scheme is standard for DFT implementations, and it is referred to as optimizing a structure.

2.2 Elastic electron transport

In the following we will investigate molecular junctions which are build out of two leads on the left and right side attached to a molecule in the center. An example is shown in Fig. 2.1. In this section we will give a short introduction to the basic scheme to describe those molecular junctions following Refs. [12, 15]. Here the ballistic electron transport is treated within the Landauer-Büttiker formalism using a Greens function scheme. First it is assumed that the direct interaction between the left and right electrode can be neglected compared to the coupling between the electrodes and the molecule. Using a local basis set allows to separate the Hamiltonian H and the overlap matrix S in blocks coupling L, C and R:

$$H = \begin{pmatrix} H_{LL} & H_{LC} & 0 \\ H_{CL} & H_{CC} & H_{CR} \\ 0 & H_{RC} & H_{RR} \end{pmatrix}; \quad S = \begin{pmatrix} S_{LL} & S_{LC} & 0 \\ S_{CL} & S_{CC} & S_{CR} \\ 0 & S_{RC} & S_{RR} \end{pmatrix}. \tag{2.19}$$

In the following we will apply the Greens function formalism to describe the transport of electrons. The Greens function, that describes the kinetics of electrons in the center can be expressed as:

$$G^r_{CC}(E) = \left[S_{CC}E^+ - H_{CC} - \Sigma^r_L(E) - \Sigma^r_R(E)\right]^{-1} = \left[G^a_{CC}(E)\right]^\dagger. \tag{2.20}$$

Here $E^+ = E + i\eta$ with $\eta > 0$ allows to select the retarded rather than the advanced Greens function. The interaction of electrons between C and the lead $X = \{R, L\}$ can be described using the embedding self energies Σ_X and the linewidth broadening matrices Γ_X :

$$\Sigma^r_X(E) = (ES_{CX} - H_{CX})\, g^r_{XX}(E)\, (ES_{CX} - H_{XC}), \quad \Gamma_X = 2\mathrm{Im}\{\Sigma^r_X\} \tag{2.21}$$

where we used the Greens function g to describe the properties of electrons in the decoupled leads. It is given by

$$g^r_{XX}(E) = \left[S_{XX}E^+ - H_{XX}\right]^{-1}. \tag{2.22}$$

The current through this system is given by:

$$I = \frac{2e}{h}\int \mathrm{d}E \underbrace{\mathrm{Tr}\left\{\Gamma_L(E)\, G^r_{CC}(E)\, \Gamma_R(E)\, G^a_{CC}(E)\right\}}_{=T_{\mathrm{el}}(E)} (f_L(E) - f_R(E)). \tag{2.23}$$

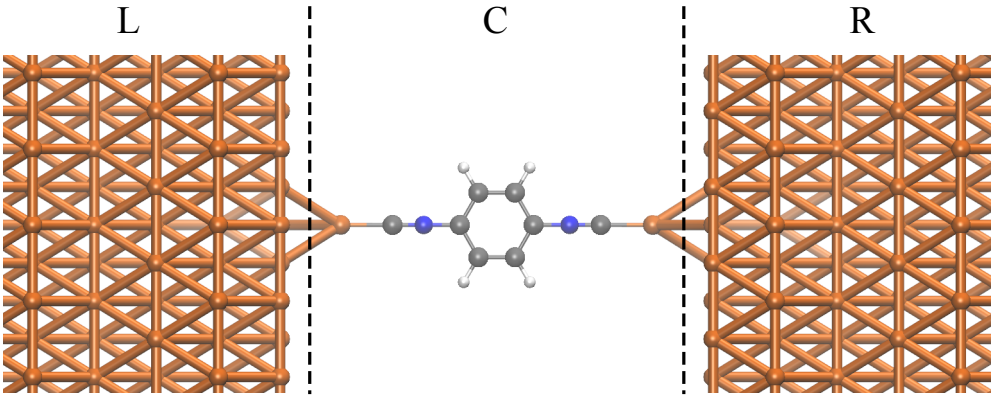

Figure 2.1: L: metal lead on the left, C: central part or extended molecule (usually a molecule plus metal atoms), R: metal lead on the right.

Here we used the Fermi function $f_X(E) = [\exp\{(E-\mu_X)/k_BT_X\}+1]^{-1}$ for the left and right electrode $X \in L, R$, which are considered to be at equilibrium.

The conductance in the Landauer-Büttiker picture is:

$$G = G_0 T_{\text{el}}(E_F) = G_0 \text{Tr}\left\{\Gamma_L(E_F)\, G^r_{CC}(E_F)\, \Gamma_R(E_F)\, G^a_{CC}(E_F)\right\} \tag{2.24}$$

Where we introduce the conductance quantum $G_0 = 2e^2/h$.

2.3 Elastic phonon transport

Similarly as we treated the electric transport through molecular junctions in Sec. 2.2 we will derive the phonon transport through molecular junctions in this section. Following Refs. [25–27], we use a Greens function scheme to describe the ballistic phonon transport. We start with the Hamilton operator for the nuclei from Eq. (2.5). Using the harmonic approximation to describe the potential energy V around the ground state geometry gives

$$H_n = \sum_{A=1}^{M} \frac{\vec{P}_A^2}{2M_A} + V\left(\vec{R}_1, \ldots, \vec{R}_M\right) \approx \sum_{l=1}^{3M} \frac{P_l^2}{2M_l} + \frac{1}{2}\sum_{l,s}^{3M} Q_l \left.\frac{\mathrm{d}^2 V}{\mathrm{d}R_l \mathrm{d}R_s}\right|_{Q=0} Q_s. \tag{2.25}$$

Here the index l denotes collectively the atomic sites A and the three Cartesian coordinates. The displacement of the nucleus from its ground state position R_l^0 is given by $Q_l = R_l - R_l^0$. With $Q = 0$ we refer to the geometry where all displacement Q_l are zero. Clearly the first order term $\sim \mathrm{d}V/\mathrm{d}R|_{Q=0}$ vanishes. The second derivatives can be combined in the Hessian matrix. The indices l and s include all M atoms and their 3 Cartesian coordinates. By using mass weighted coordinates,

$$q_l = \sqrt{M_l} Q_l \quad \text{and} \quad p_l = \frac{P_l}{\sqrt{M_l}}, \tag{2.26}$$

the Hamiltonian becomes

$$H_n = \frac{1}{2}\sum_l p_l^2 + \frac{1}{2}\sum_{ls} q_l K_{ls} q_s, \quad K_{ls} = \left.\frac{1}{\sqrt{M_l M_s}} \frac{\mathrm{d}^2 V}{\mathrm{d}R_l \mathrm{d}R_s}\right|_{Q=0}. \tag{2.27}$$

Here we introduced the force constant matrix K. In the mass-weighted coordinates the canonical commutation relations are

$$[q_k, p_l] = i\hbar\delta_{kl}, \quad [q_k, q_l] = 0, \quad [p_k, p_l] = 0. \tag{2.28}$$

We separate the terms in the Hamiltonian H_n in L, C and R as indicated by Eq. (2.19).

To find the phonon heat current we calculate the energy that flows out of lead L

$$J = -\dot{E} = -\left\langle \dot{H}_{LL} \right\rangle = -\frac{i}{\hbar}\left\langle [H, H_{LL}] \right\rangle = \sum_i^C \sum_j^L \left\langle p_j q_i \right\rangle K_{ij}. \tag{2.29}$$

We describe the displacement q_l of the nuclei l using a Greens function scheme. The real time Greens functions are defined as:

$$D^r_{kl}(t,t') = -\frac{i}{\hbar}\Theta(t-t')\left\langle [q_k(t), q_l(t')] \right\rangle \tag{2.30}$$

$$D^a_{kl}(t,t') = \frac{i}{\hbar}\Theta(t'-t)\left\langle [q_k(t), q_l(t')] \right\rangle \tag{2.31}$$

$$D^<_{kl}(t,t') = -\frac{i}{\hbar}\left\langle q_l(t') q_k(t) \right\rangle \tag{2.32}$$

$$D^>_{kl}(t,t') = -\frac{i}{\hbar}\left\langle q_k(t) q_l(t') \right\rangle \tag{2.33}$$

It is a bit unusual to use the displacement rather than the phonon creation operator. But since the q_l fulfill the commutation relations in Eq. (2.28) and appear quadratic in the Hamiltonian, there is no restriction. The phonon current is

$$J = i\hbar\frac{\partial}{\partial t}\sum_{i}^{L}\sum_{j}^{C} D_{ij}^{<}(t,t')K_{ij}\big|_{t=t'}. \tag{2.34}$$

Further we will switch to the frequency space using the Fourier transformation

$$f(\omega) = \int dt e^{i\omega t} f(t), \tag{2.35}$$

$$f(t) = \int \frac{d\omega}{2\pi} e^{-i\omega t} f(\omega). \tag{2.36}$$

Assuming steady state, the Greens function depends only on the time difference and the Fourier transformation gives

$$J = \int_0^\infty \frac{d\omega}{2\pi}\hbar\omega \mathrm{Tr}\left(K_{CL}D_{LC}^{<}(\omega) - D_{CL}^{>}(\omega)K_{LC}\right). \tag{2.37}$$

Here, $D_{ij}^{<}(-\omega) = D_{ji}^{>}(\omega)$ was used, and Tr is the trace of the matrix.

Now it is most convenient to get rid of terms that couple L and C. Therefore the equation of motion for the Greens function $G^{\lessgtr}$ is calculated by applying the Langreth rules to the equation of motion of the time-ordered contour Greens function. Finally, we also use the basic expression $D^r - D^a = D^> - D^<$ and find:

$$J = \int_0^\infty \frac{d\omega}{2\pi}\hbar\omega \mathrm{Tr}\left(\Pi_L^{>}(\omega)D_{CC}^{<}(\omega) - \Pi_L^{<}(\omega)D_{CC}^{>}(\omega)\right), \tag{2.38}$$

here the phonon embedding self energy Π is

$$\Pi_X^{\gtrless,a,r}(\omega) = K_{CX}d_X^{\gtrless,a,r}(\omega)K_{XC}, \tag{2.39}$$

where $X \in \{L,R\}$ and the $d_X(\omega)$ are the Greens function of the uncoupled leads. Because the leads are macroscopic systems, we assume that they are in equilibrium. Therefore the phononic energy states are occupied according to the Bose function

$$b_X(\omega) = \frac{1}{e^{\hbar\omega/k_BT_X} - 1}. \tag{2.40}$$

The lead Greens functions $d_X^{\lessgtr}(\omega)$ are

$$d_X^{<}(\omega) = b_X(\omega)\left(d_X^r(\omega) - d_X^a(\omega)\right) \tag{2.41}$$

$$d_X^{>}(\omega) = \left(b_X(\omega)+1\right)\left(d_X^r(\omega) - d_X^a(\omega)\right) \tag{2.42}$$

We use the Keldysh equation for the central Greens function $D_{CC}^{<}$ and the current is

$$J = \int_0^\infty \frac{d\omega}{2\pi}\hbar\omega \underbrace{\mathrm{Tr}\left\{\Lambda_L(\omega)D^r(\omega)\Lambda_R(\omega)D^a(\omega)\right\}}_{=T_{\mathrm{ph}}(\omega)}\left(b_L(\omega) - b_R(\omega)\right). \tag{2.43}$$

Here the coupling $\Lambda_X(\omega) = 2\mathrm{Im}\left\{\Pi_X^r(\omega)\right\}$ was used and we introduced the phonon transmission $T_{\mathrm{ph}}(\omega)$.

2.4 Thermoelectric transport coefficients

In the last sections we presented the derivation of the electron and phonon current through the molecular junction. With them at hand the thermoelectric properties can be calculated. First we treat the electronic degree of freedom. Here the transport coefficients due to voltage gradients ΔV or temperature gradients ΔT can be summarized by:

$$\begin{pmatrix} I \\ Q \end{pmatrix} = \begin{pmatrix} G & L \\ M & K \end{pmatrix} \begin{pmatrix} \Delta V \\ \Delta T \end{pmatrix}, \tag{2.44}$$

where I is the electron current from Eq. (2.23) and the heat current Q due to electrons is [15, 28]

$$Q = \frac{2}{h} \int \mathrm{d}E \, (E - E_F) \, T_{\mathrm{el}}(E) \, [f_L(E) - f_R(E)] \, . \tag{2.45}$$

To provide a vivid interpretation, each electron carries the heat energy of $(E - E_F)$ through the junction. In linear response we can expand the difference of the Fermi function in the first order of $\Delta\mu = \mu_L - \mu_R = -e\Delta V$ as well as $\Delta T = T_L - T_R$. We set $T = (T_L + T_R)/2$ and $\mu = (\mu_L + \mu_R)/2 \approx E_F$. Then the transport coefficients can be calculated. The temperature dependent conductance is

$$G = \left. \frac{I}{\Delta V} \right|_{\Delta T = 0} = G_0 \int \mathrm{d}E \left(-\frac{\partial f}{\partial E} \right) T_{\mathrm{el}}(E) = G_0 K_0, \tag{2.46}$$

the Seebeck coefficient can be calculated using

$$S = -\left. \frac{\Delta V}{\Delta T} \right|_{I=0} = \frac{L}{G} = -\frac{K_1}{eTK_0}, \tag{2.47}$$

and the heat conductance of the electronic system is

$$\kappa_{\mathrm{el}} = -\left. \frac{Q}{\Delta T} \right|_{I=0} = -\left(K - \frac{ML}{G} \right) = \frac{2}{hT} \left(K_2 - \frac{K_1^2}{K_0} \right) \tag{2.48}$$

Here, we used the integrals

$$K_n = \int \mathrm{d}E T_{\mathrm{el}}(E) \left[-\frac{\partial f}{\partial E} \right] (E - \mu)^n \, . \tag{2.49}$$

Additionally, the phonons contribute to the heat transport as well. The phonon current J in Eq. (2.43) is the amount of heat transported through the contact by the phonons. Therefore in linear response the phonon heat conductance is:

$$\kappa_{\mathrm{ph}} = -\left. \frac{J}{\Delta T} \right|_{I=0} = k_B \int_0^\infty \frac{\mathrm{d}\omega}{2\pi} T_{\mathrm{ph}}(\omega) \hbar\omega \left(\frac{\mathrm{d}b(\omega)}{\mathrm{d}T} \right) . \tag{2.50}$$

With the described thermoelectric transport coefficients we are able to estimate the efficiency of a thermoelectric device build with molecular junctions. For this purpose usually the figure of merit

$$\mathrm{ZT} = \frac{GS^2T}{\kappa_{\mathrm{el}} + \kappa_{\mathrm{ph}}} \tag{2.51}$$

is used [29].

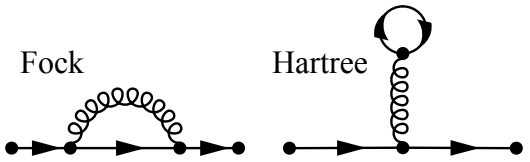

Figure 2.2: Diagrams of first order in the electron-phonon interaction. They contribute to the inelastic electronic current. The solid line is a electron propagator and the wiggly line is the phonon propagator

2.5 Inelastic electron current due to electron-phonon scattering

Following Refs. [13, 14] the electron-phonon interaction in molecular junctions is treated in the C part of the geometry that is sketched in Fig. 2.1. The full Hamiltonian is:

$$\hat{H} = \hat{H}_e + \hat{H}_n + \hat{H}_{n-e} \tag{2.52}$$

The electron-phonon interaction can be written with electron creation (annihilation) operators d ($d^\dagger$) and phonon creation (annihilation) operators b ($b^\dagger$), as

$$\hat{H}_{n-e} = \sum_{ij} \sum_{\alpha} d_i^\dagger \lambda_{ij}^\alpha d_j \left(b_\alpha + b_\alpha^\dagger\right) \tag{2.53}$$

The electron-phonon interaction λ is calculated by

$$\lambda_{ij}^\alpha = \left(\frac{\hbar}{2\omega_\alpha}\right) \sum_l \langle j| \left.\frac{\partial \hat{H}}{\partial R_l}\right|_{\vec{R}^0} |i\rangle \frac{C_l^\alpha}{\sqrt{M_l}}, \tag{2.54}$$

where C^α is the eigenvector of the force constant matrix K, defined in Eq. (2.27). The C^α are given by

$$KC^\alpha = \omega_\alpha^2 C^\alpha, \quad \left(C^\alpha\right)^T C = 1. \tag{2.55}$$

Here ω_α is the phonon frequency. The perturbation theory yields two corrections to the Eq. (2.23):

$$\delta I_{\text{el}} = \frac{4e}{\hbar} \int \frac{\mathrm{d}E}{2\pi} \text{Tr}\left\{\Gamma_L G^r \Sigma^>_{\text{e-vib}} G^r \Gamma_R G^a\right\} \left(f_L - f_R\right) \tag{2.56}$$

$$I_{\text{inel}} = \frac{2e}{\hbar} i \int \frac{\mathrm{d}E}{2\pi} \text{Tr}\left\{G^a \Gamma_L G^r \left[f_L \Sigma^>_{\text{e-vib}} - \left(f_L - 1\right) \Sigma^<_{\text{e-vib}}\right]\right\} \tag{2.57}$$

Here $\Sigma_{\text{e-vib}}$ is the self-energy due to the Hartree and Fock diagrams, shown in Fig. 2.2, that is the first non-vanishing order in the electron phonon interaction. The expression for $\Sigma_{\text{e-vib}}$ and further details on the formalism can be found in Refs.[13, 14].

Part I

Properties of molecular junctions revealed by electron transport

3 Characteristics of amine-ended and thiol-ended alkane single-molecule junctions revealed by inelastic electron tunneling spectroscopy

In this chapter we present our results obtained in collaboration with the group of Prof. Elke Scheer (University of Konstanz). On the experimental side Youngsang Kim measured properties of molecular junctions to characterize different anchor groups.

In molecular electronics anchor groups are used to bind molecules to metal electrodes. To investigate the properties of two different anchor groups, which are widely used in molecular electronics, we focus on two octane molecules synthesized with thiol- and amine-anchors. They are called octane-dithiol (ODT) and octane-diamine (ODA), respectively.

To analyze the properties of amine and thiol anchors, we model the mechanics of the experimental setup, as described in Sec. 3.1. In Sec 3.2 we show the calculated opening curve and discuss the conductance mechanism. In Sec 3.3 we present the calculated inelastic electron tunneling spectroscopy (IETS), in which we analyze the metal anchor group vibration modes as well as the agreement with experiments.

3.1 Modeling molecular junctions: geometrical and mechanical properties

The most commonly used techniques to measure the conductance of single molecules are either the scanning tunneling microscope or the MCBJ method. In the group of Prof. Scheer MCBJs are used [30]. The MCBJ setup is shown in Fig. 3.1 (a). It is build as follows. A 80 nm thick gold layer is deposited on top of a flexible substrate. The form of the gold layer is shaped such that the central part is narrow. Ideally the conductance through the central part is due to a few gold atoms. The substrate below this constriction is etched away to form a free standing bridge, well separated from the substrate. If the substrate is bent, the free-standing bridge is stretched. A rod is used to bend the substrate. This rod pushes against the substrate from below. The contact breaks if the substrate is bent strongly enough. The distance between the two electrodes can be controlled with the rod.

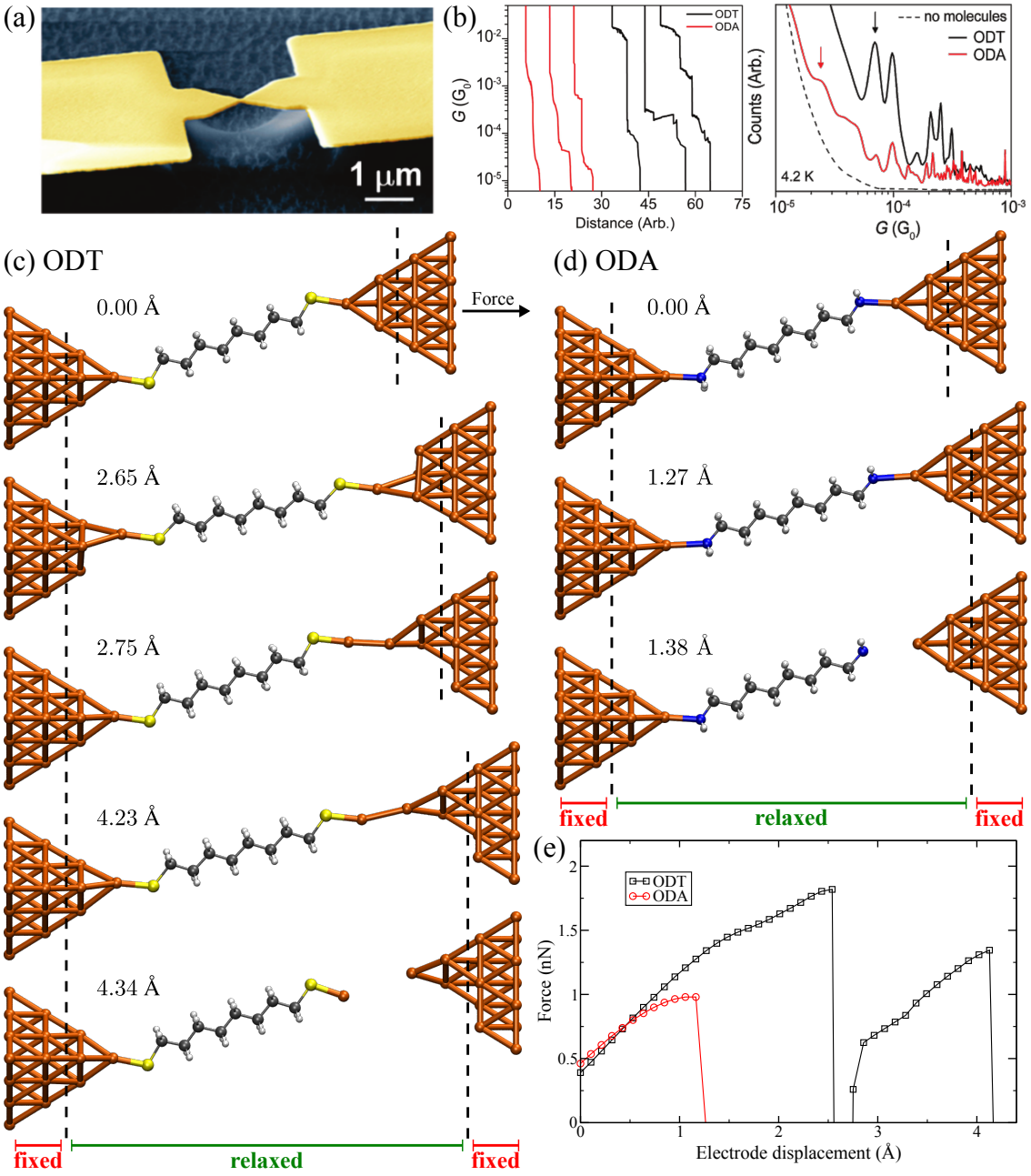

Figure 3.1: (a) Scanning electron microscopy image of a mechanically controllable break-junction (MCBJ). (b) Conductance traces of ODT (black) and ODA (red) molecular junctions and the conductance histogram obtained from many conductance traces. Junction geometries for ODT (c) and ODA (d) at different electrode displacements and evolution of the force (e) that acts on the electrode during the stretching process. In (c) and (d) the displacement distance, measured with respect to the initial geometry, is listed above the respective junction structure. At the first ODT structure the direction of the force is indicated - in that direction the gold electrode is pulled. At the bottom, fixed and relaxed junction regions during the stretching process are indicated.

To measure the conductance of a single-molecule junction, the molecules are provided to the region of the free standing bridge in solution. The molecules bind to the surface of the gold electrodes. After removing the solution, a mono-layer of molecules remains. The contact is opened and closed repeatedly, while the conductance is recorded. Here the conductance G is measured as a function of the electrode displacement. Examples of the so-called conductance traces are plotted in Fig. 3.1 (b). Due to the statistical character of the experiments the conductance is analyzed using conductance histograms. The junctions with the lowest stable conductance, as indicated by the position of the lowest conductance peak, are supposed to correspond to single-molecule junctions.

To calculate the electrical as well as mechanical properties of the molecular junctions we use DFT as implemented in TURBOMOLE. We used the BP86 functional [31, 32] and the def2-SV(P) basis set [33]. The total energy is converged to a precision better than 10^{-6} a.u., the structure optimizations are carried out till the maximum norm or the gradients have fallen below 10^{-4} a.u.. The position of atoms in the electrodes is fixed as indicated in Fig. 3.1.

In theory, we model the process of pulling the electrodes apart, in order to describe the mechanical deformation during the pulling process. Especially on an atomic scale we gain insight how the junction is deformed and eventually breaks upon stretching. The extended central cluster (ECC) that mimics the molecular junction at different electrode displacements, is shown in Fig. 3.1. At the first geometry the electrode displacement is by definition 0.00 Å. That geometry is constructed so that the molecule is not elongated. To construct this ECC we start from a geometry where the molecule is situated in front of one gold electrode. From that geometry we extract the gold-molecule binding geometry, after we minimized the gradients. In case of the ODT molecule we protect the second thiol anchor by means of a hydrogen atom. In a second step the ECC geometry is formed using the just extracted binding motives. After relaxing this structure we obtain the ECC geometry labeled as 0.00 Å in Fig. 3.1. Both gold electrodes attached on the left and right side are modeled using 20 gold atoms. From those, 16 atoms are located at fixed positions. The fixed atoms are at the fcc lattice positions. We describe transport along the $\langle 111 \rangle$ lattice direction of gold. Therefore the electrodes are oriented accordingly.

To model the stretching of the molecular junction, the fixed gold atoms are shifted by 0.1 a.u. on both sides. Then we relax the new geometry. That procedure is repeated until the contact breaks. Analyzing the deformations during the pulling process, we find that the amine anchors do not deform the gold electrodes. The rupture is at the amine gold bond. The picture is different, if we use thiol anchors. Here the sulfur-gold bond is so strong that the gold electrode is deformed. A gold chain is pulled at an electrode displacement of around 2.75 Å. The contact breaks at an electrode displacement of around 4.34 Å. The rupture occurs at the gold-gold bond of the pulled chain and a gold atom from the electrodes stays with the molecule, as shown in Fig. 3.1. This shows that the thiol-gold bond is much stronger than the amine-gold bond.

To make a more precise statement, we calculate the force that is necessary to pull the electrodes apart. That force is plotted in Fig. 3.1 (e). We determine that force by calculating the total energy of the ECCs at each electrode displacement. From that the force is determined by differentiating the total energy with respect to the electrode displacement using finite differences. Here we find that the sulfur-gold bond withstands at least 1.8 nN, before the gold chain is pulled out of the electrode at about 2.75 Å. In addition we determine that the pulled gold chain resists a force of approximately 1.3 nN before the rupture occurs. The force a gold chain can withstand is measured as 1.5 nN using a AFM [34]. On the other hand the amine-gold bond breaks much earlier at an electrode displacement

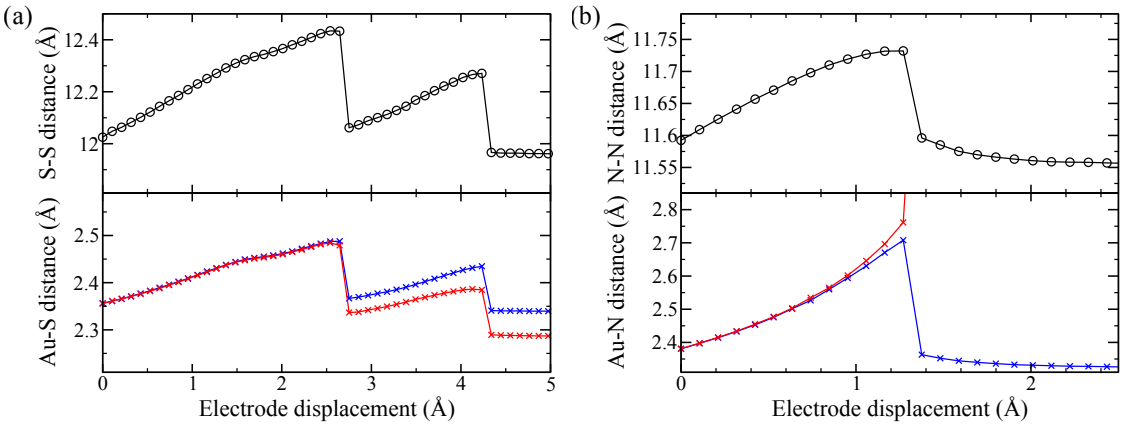

Figure 3.2: Molecule length and bond lengths at the molecule-electrode interfaces as a function of the electrode displacement for (a) ODT and (b) ODA junctions, respectively.

of about 1.4 Å. At that point the force is approximately 1 nN.

According to our theoretical investigations, the binding energy of the amine-gold bond (0.92 eV) is significantly weaker than that of the thiol-gold bond (1.76 eV) for the binding in top position as shown in Fig. 3.1. We determine the binding energy by cleaving the Au-molecule-Au junction geometry labeled 0.00 Å in Fig. 3.1 at one of the Au-molecule bonds. Then we subtract the total energy of the intact system from the sum of the separate parts.

In Fig. 3.2 we show various characteristic lengths in the molecular contacts as a function of the electrode displacement. For ODT these are the Au-S distances at each interface between the sulfur and the gold atom closest to it and the molecule length measured as the distance between the sulfur atoms. For the ODA junction we show the Au-N distance, accordingly as well as the N-N distance, that mimics the molecular length. We find that the Au-S bonds in ODT are elongated by ~ 0.15 Å at most as compared to their initial values, while the Au-N bonds in ODA are stretched by ~ 0.3 Å before contact rupture. The stronger Au-S bonds also lead to larger elongations of the alkane molecule. Thus, we find for ODA that the N-N distance changes by ~ 0.15 Å during stretching (the N-N distance change from 11.6 Å to 11.75 Å), while the modification can amount up to 0.4 Å for ODT (the S-S distance change from 12 Å to 12.4 Å).

3.2 Conductance as a function of the electrode displacement

In experiment the conductance is measured while the electrodes are pulled apart. For a better understanding, we performed simulations of the stretching of ODT and ODA single-molecule junctions using a DFT-based scheme. Besides the equilibrium structures at the different elongation stages, we determined the conductance within the Landauer-Büttiker formalism. We find it to range between $1 \cdot 10^{-4} G_0$ and $3 \cdot 10^{-4} G_0$ for ODT contacts and between $4 \cdot 10^{-5} G_0$ and $6 \cdot 10^{-5} G_0$ for ODA, as shown in Fig. 3.3 (a). Analyzing the conductance histogram measured in the experiments reveals a conductance of $(7.0 \pm 1.2) \cdot 10^{-5} G_0$ for the ODT molecule and a conductance of $(3.0 \pm 0.5) \cdot 10^{-5} G_0$ for the ODA molecule. Compared to the experiment, the conductance is overestimated in both cases by a factor of around 3. This may be related to uncertainties in the description of the alignment of the molecular states and the metal Fermi energy, as well as the band gap problem of DFT [35–38]. However, the deviations appear acceptable, considering the

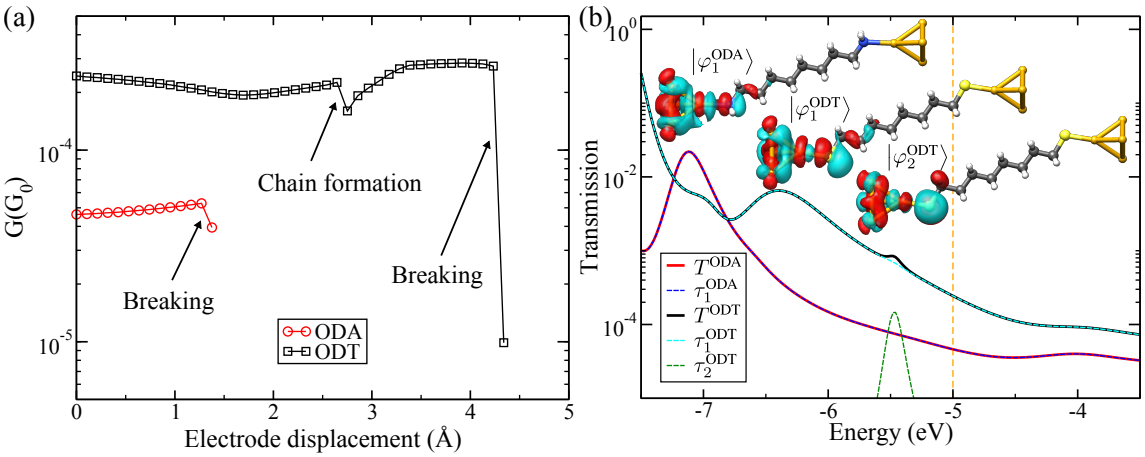

Figure 3.3: (a) Calculated conductance of ODT and ODA junctions as a function of the electrode displacement. The kink in the ODT trace around 2.8 Å indicates the formation of a gold chain. The simulated atomic arrangements, shortly before and after the chain forms, are shown in Fig. 3.1. (b) Transmission for electrode displacement of 0.0 Å. The solid lines show the total transmission, the dashed lines show the contribution of a single transmission channel. The inset shows the isosurface plots of the eigenwavefunctions that correspond to the plotted transmission channels at the Fermi energy.

lack of knowledge with respect to the precise contact geometry. The reduced conductance, by a factor of around 5, for similar junction geometries of ODA as compared to ODT is in qualitative agreement with the experimental observations and previous reports in the literature [38, 39].

In order to determine the transport properties, we compute the energy-dependent transmission as shown in Fig. 3.3 (b), for the electrode displacement of 0.00 Å. We obtain the conductance in units of $G_0 = 2e^2/h$ as the value of the transmission at the Fermi energy E_F. Following the scheme of Ref. [12], we extract bulk parameters, as needed for the construction of the surface Green's functions, from spherical 429 atom gold clusters in a separate step. The spherical Au_{429} clusters also yield the value $E_F = -5$ eV for the BP86 functional.

Analyzing the energy-dependent transmission in Fig. 3.3 (b) we find that the transmission at the Fermi energy is dominated by one transmission channel for both ODA and ODT. It can be described by a Lorentz-like shape. For ODT there is a second transmission channel τ_2^{ODT} approximately 0.5 eV below the Fermi energy. The corresponding scattering state of that transmission channel $\left|\varphi_2^{\mathrm{ODT}}\right\rangle$ at the Fermi energy is shown in the inset of Fig. 3.3 (b). Here the π state of the sulfur couples to the electrodes. This results in an apparently almost blocked transmission channel at the Fermi energy. While the transmission at the Fermi energy is clearly dominated by the first transmission channel the second transmission channel results in a small kink in the transmission at the corresponding resonance energy. The first transmission channel utilizes the σ orbitals of the ODT and their resonance energy is about 1.4 eV below the Fermi energy. Similar to ODT, we find the charge transport to be hole-like for the ODA junctions, where the resonance dominating the conductance is positioned $\sim$ 2 eV below E_F and arises mainly from hybridized molecular electronic states located on the amines with σ character. We find that the transport for both ODT and ODA is dominated by electronic states with a high weight on the anchoring groups of the molecules and is slightly more off-resonant for ODA than ODT.

In experiments the electrode displacement can be measured in an indirect manner. It is

the length of the conductance plateau in the opening curves. For ODT a statistical analysis results in 30 ± 11 Å while for ODA only 11 ± 3 Å are measured. In contrast the simulations for ODT revealed a plateau length of about 4.4 Å, while it is for ODA with about 1.4 Å clearly smaller. Although the relative change between ODT and ODA agrees with experiment, the discrepancy in the absolute values between experiment and the theory is a factor of about 10. We attribute this to the fact that we start in our calculations with rather straight molecules bonded to the ends of gold tips, as shown in Fig. 3.1. In the experiments, the molecules can be twisted and stretched upon elongation, or their anchoring group may "slide" along the metallic electrodes on both sides toward the tip ends. This explains why the plateau length measured for ODA is peaked at around 12 Å, the length of the isolated ODA molecule (N-N distance shown in Fig. 3.2). For ODT deformations of the metal electrode can arise in addition, which we cannot account for entirely in the calculations due to the limited amount of flexible atoms in the Au electrodes. Nevertheless, the experimental and theoretical results consistently suggest that strong mechanical deformations of the gold electrodes are involved for ODT, possibly including the formation of a gold chains, while such deformations are essentially absent for ODA.

In the calculated opening curve, shown in Fig. 3.3 (a), we find a kink feature for the ODT molecular junction. That feature is at the electrode displacement of around 2.75 Å where the gold chain is pulled from the electrodes. In case of ODA we find a smooth conductance plateau. We use the appearance of kinks in the conductance plateaus as an indication of chain formation or, more generally, a mechanical deformation of the gold electrodes. The measured conductance traces were analyzed in that respect. The measured conductance plateaus usually exhibit a negative slope throughout the whole stretching process, as shown in Fig. 3.1 (b). Therefore, we identify a kink by a change of the conductance-distance slope from negative to positive. The analysis of the measured conductance traces reveals that the kink feature is present in 45% of the ODT junctions, while only 15% of the ODA junctions revealed that feature. Hence, the low percentage of the kinks in ODA junctions signals that the amine anchors do not cause strong mechanical deformations of the gold electrodes during stretching.

3.3 Inelastic electron tunneling spectra

To gain more insights into the geometry realized in the molecular junctions we calculate the IETS. Following the experiments, we calculate the IETS at 4.2 K and broaden our calculated spectra by an ac voltage of 6 mV (root-mean-square) [41, 42]. We normalize the second derivative of the $I(V)$ curve by the differential conductance in order to compensate for the conductance change of the molecular junction. The IETS amplitude is defined as

$$\text{IETS} = \frac{\mathrm{d}^2 I}{\mathrm{d}V^2} \Big/ \frac{\mathrm{d}I}{\mathrm{d}V}.$$

In Fig. 3.4 (a) and (b) we show the measured as well as calculated IETS for the ODT and ODA molecular junction. Here we show the low-energy regime of the IETS spectra, that is for voltage below 200 mV, which is regarded as the "fingerprint regime" of a molecular junction, because the fundamental vibrational modes typically fall in this energy range. We observe prominent molecular vibrational peaks for both ODT and ODA molecular junctions. Due to the many modes contributing to the IETS for voltages below 25 mV, these energies are excluded from the discussion here. But we will come back to them when we consider the interface vibrational modes.

The calculated IETS spectra were obtained for the geometries with an electrode displacement of 0.00 Å, as shown in Fig 3.2. We compare them to experimental spectra

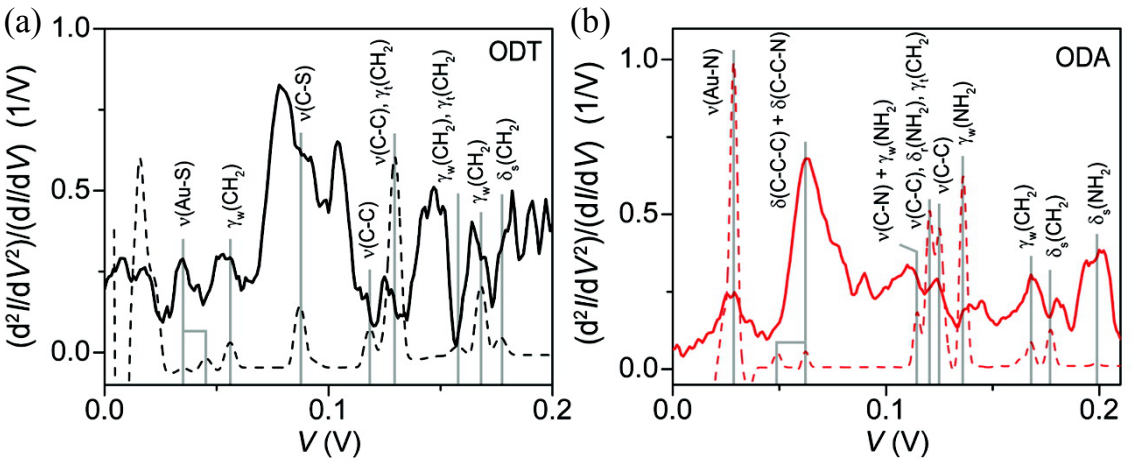

Figure 3.4: Comparison of experimental (solid lines) and theoretical (dashed lines) IETS spectra of (a) ODT and (b) ODA single-molecule junctions. Experimental results are obtained from the lock-in second-harmonic signals at 4.2 K. The vertical lines show the peak positions in the theoretically obtained spectra, and modes of the same character are summarized by horizontal lines. The character of the modes is specified by the symbols explained in the text. The separation by a comma means that the peak is due to several modes, while "+" is used to indicate the mixed character of a mode. Figure from Ref. [40].

taken from the middle of stretching experiments, because in this situation a straight, but not strongly elongated molecular junction can be assumed.

In the IETS we indicate the character of the mode that contributes most to the peak. Those modes, identified by the comparison between theory and experiment, are summarized in Tab. 3.1. According to our analysis, the peak at around 35 mV in Fig. 3.4 (a) results from the ν (Au-S) stretching mode and those at 29 mV in Fig. 3.4 (b) from the ν (Au-N) stretching mode. They signal that both amine and thiol end groups are robustly bonded to the gold electrodes. Further main peaks in the experimental IETS at around 53, 78, 125, 164, and 182 mV for the Au-ODT-Au junction are attributed to $\gamma_{\mathrm{w}}(\mathrm{CH_2})$ wagging, ν(C-S) stretching, ν(C-C) stretching and $\gamma_{\mathrm{t}}(\mathrm{CH_2})$ twisting, $\gamma_{\mathrm{w}}(\mathrm{CH_2})$ wagging, and $\delta_{\mathrm{s}}(\mathrm{CH_2})$ scissoring, respectively, in accordance with previous studies [43–53]. For the Au-ODA-Au junction we assign the main peaks at 63, 110, 124, 139, 168, 180, and 200 mV to combined δ(C-C-C) and δ(C-C-N) bending, combined ν(C-N) stretching and $\gamma_{\mathrm{w}}(\mathrm{NH_2})$ wagging, ν(C-C) stretching, $\gamma_{\mathrm{w}}(\mathrm{NH_2})$ wagging, $\gamma_{\mathrm{w}}(\mathrm{CH_2})$ wagging, $\delta_{\mathrm{s}}(\mathrm{CH_2})$ scissoring, and $\delta_{\mathrm{s}}(\mathrm{NH_2})$ scissoring, respectively.

As expected, the higher energy modes above 100 meV, affecting mainly the C and H atoms of the molecule, appear at similar energies for ODA and ODT, however with different amplitudes in the IETS. Modes including motions of the $\mathrm{NH_2}$ groups appear in a broad energy range. We observe that some modes appearing in the experimental spectra are absent in the theoretical ones and vice versa. This discrepancy is due to the fact that only single spectra are compared, likely corresponding to different contact configurations. Choosing the peak at 104 mV in the spectrum of ODT as an example, it has been shown [52] that the $\delta_{\mathrm{r}}(\mathrm{CH_2})$ rocking modes, to which we ascribe the peak, may be excited only in certain configurations, which lift particular symmetries. Other prominent features, not explained by our calculations, could be due to combined $\gamma_{\mathrm{w}}(\mathrm{CH_2})$ wagging and $\gamma_{\mathrm{t}}(\mathrm{CH_2})$ twisting modes at 147 meV for ODT and $\delta_{\mathrm{r}}(\mathrm{CH_2})$ rocking modes at 90 meV for ODA.

In the following we concentrate on metal-anchor group vibrations. The different behavior of thiol-ended and amine-ended molecular junctions is further elucidated, when we

ODT			
Mode	Description	Experiment	Theory
ν(Au-S)	Au-S stretching	35	35, 45
$\gamma_w(CH_2)$	CH_2 wagging	53	56
ν(C-S)	C-S stretching	78	86
ν(C-C)	C-C stretching		118
ν(C-C), $\gamma_t(CH_2)$	C-C stretching, CH_2 twisting	125	130
$\gamma_w(CH_2)$, $\gamma_t(CH_2)$	CH_2 wagging, CH_2 twisting		157
$\gamma_w(CH_2)$	CH_2 wagging	164	168
$\delta_s(CH_2)$	CH_2 scissoring	182	178
ODA			
Mode	Description	Experiment	Theory
ν(Au-N)	Au-N stretching	29	29
δ(C-C-C) + δ(C-C-N)	C-C-C bending with C-C-N bending	63	50, 64
ν(C-N) + $\gamma_w(NH_2)$	C-N stretching with NH_2 wagging	110	115
ν(C-C), $\delta_r(NH_2)$, $\gamma_t(CH_2)$	C-C stretching, NH_2 rocking, CH_2twisting		121
ν(C-C)	C-C stretching	124	126
$\gamma_w(NH_2)$	NH_2 wagging	139	137
$\gamma_w(CH_2)$	CH_2 wagging	168	169
$\delta_s(CH_2)$	CH_2 scissoring	180	178
$\delta_s(NH_2)$	NH_2 scissoring	200	199

Table 3.1: Summary of the vibrational modes assignment in the IETS spectra of ODT and ODA molecular junctions, shown in Fig. 3.4. The peak position in the IETS spectra is given in mV, as found in the experiment and in theory. We describe the character of the vibration modes. If we separate modes by a comma, there are several contributing to the same peak. If we use "+" or "with", a single mode has a mixed character.

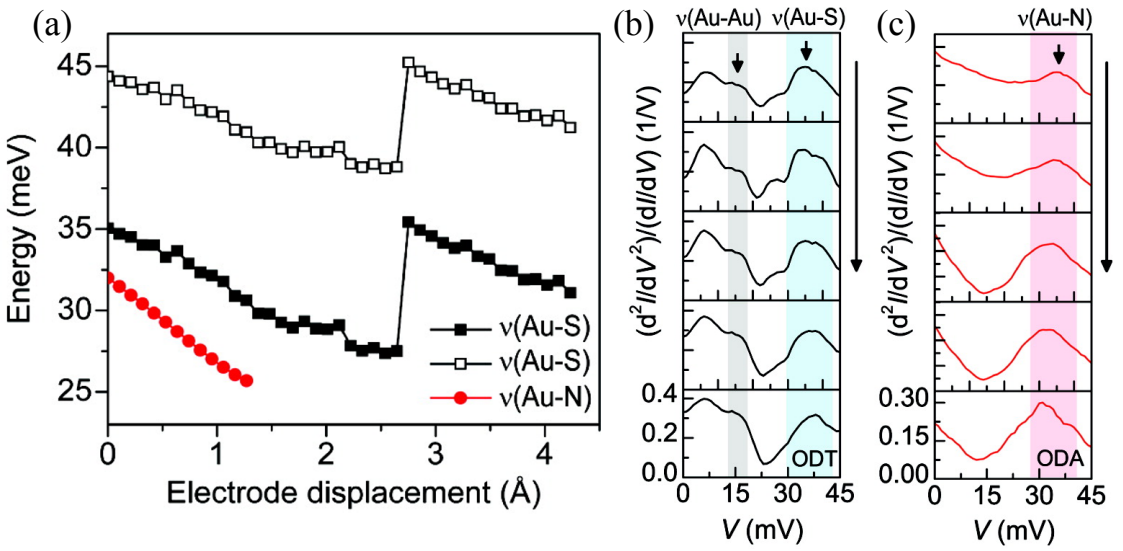

Figure 3.5: (a): Vibrational energies of gold–anchor group stretching modes as a function of the electrode displacement for ODT and ODA molecular contacts. The ν(Au-S and ν(Au–N) modes shown are those causing the peaks in the calculated IETS spectra in Fig. 3.4. (b) and (c) show the evolution of the measured IETS spectra, obtained at the lowest conductance plateaus for dc bias voltages up to 45 mV, for the stretching (in the order of the arrow) of a single-junction realization for ODT and ODA, respectively. Y-axes are of the same scale in each panel. Figure from Ref. [40].

compare the ν(Au-S) and ν(Au-N) vibrational modes in the IETS spectra for increasing electrode separation. The evolution of the energy of the ν(Au-S) and ν(Au-N) vibrations for ODT and ODA junctions is shown in Fig. 3.5 (a). These modes lead to the peaks in the computed IETS spectra in Fig. 3.4. We find a substantial red shift of the ν(Au-S) and ν(Au-N) vibrational energies upon stretching for both kinds of junctions. In Fig. 3.5 (b) and (c) the measured IETS below 45 mV is presented for increasing stretching distance in the order from top to bottom. In Fig. 3.5 (b) the ν(Au-S) mode is very stable, and no significant change of vibrational energy during the stretching of the junction can be noticed. In contrast, in the Au-ODA-Au junction of Fig. 3.5 (c), the energy of the ν(Au-N) mode is red-shifted by more than 5 mV with increasing electrode separation. The ν(Au-N) mode shows a behavior in good agreement with the experiment. In contrast, the decreasing frequency of the ν(Au-S) modes during the elastic stages does not comply with the experimental observations. However, we expect that the calculations underestimate the deformability of the gold electrodes due to the limited reservoir of mobile gold atoms assumed for practical reasons. Indeed, when stress is released by pulling gold atoms out of the electrodes in the plastic stages, we observe a "revival", i.e., an increase, of the ν(Au-S) vibrational frequencies. The experiments hence suggest that the force constants of the Au-S stretching modes stay effectively constant on the experimental time scales due to the mechanical deformations of the metal electrodes. Overall, this comparison of ν(Au-S) and ν(Au-N) modes with the help of the experimental IETS measurements clearly demonstrates that the Au–N bond is significantly weaker than the Au–S bond.

3.4 Conclusions

In this chapter we presented our investigations of the different properties of two anchor groups often used in molecular electronics. In our simulations of the junction stretching, we determined the force that is applied at the molecule metal interface. Here the thiol

anchors withstand more than 1.8 nN, that is twice as much as the amine anchors. We found that the thiol-gold bond is strong enough to pull a gold atom from the electrode at the junction rupture. The electrode deformation due to the stretching of the Au-ODT-Au contact was found to create features in the opening traces, which were also observed in the experiments. The IETS was calculated and the vibrational modes leading to peaks were analyzed.

In summary, the detailed comparison of theoretical and experimental IETS spectra reveals the complex interplay of molecular conformation and inelastic transport. Changing the anchoring group has an important influence on the vibrational spectrum and the possibility to excite modes electrically.

4 Electron transport through π-stacked molecules

In this chapter we present our detailed study of the electric transport properties of molecular π-electron systems. We focus on the transport perpendicular to the π system of benzene molecules which are connected to gold electrodes. In the literature there is a series of recent publications [54–59] concerning π-stacked systems in molecular electronics that indicates a vivid scientific interest in this topic. We decided to choose a system that includes a small number of atoms while it is still realistic to be realized in experiments. Thereby we minimize the amount of computing power but we are still able to compare our results to experiments. Under these requirements we chose paracyclophane molecules which are shown in Fig. 4.1 (a). We consider paracyclophanes that include two, three or four benzenes rings which are clipped together by short ethane chains. Measurements of their conductance are already available [60].

The structure of this chapter is as follows: We describe the properties of the paracyclophane molecules briefly in the first section of this chapter. Then we focus on the electric transport in Sec. 4.2, where we analyze the conductance with a special focus on the conduction mechanism. The influence of electron vibration coupling on the charge transport is then investigated in Sec. 4.3. For our studies of the heat and thermoelectric transport properties of these molecules we refer the reader to Chap. 8.

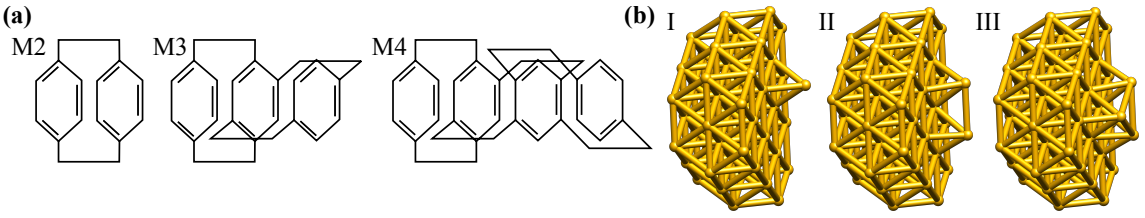

Figure 4.1: (a) Chemical structure of the investigated molecules which consists of two (M2), three (M3) and four (M4) benzene rings linked via ethane chains, such that their π systems overlap. (b) Gold clusters used to model the electrodes. On a plane gold surface we add one (I), two (II) or three (III) adatoms. The transport is directed parallel to the $\langle 111 \rangle$ direction of the gold fcc lattice.

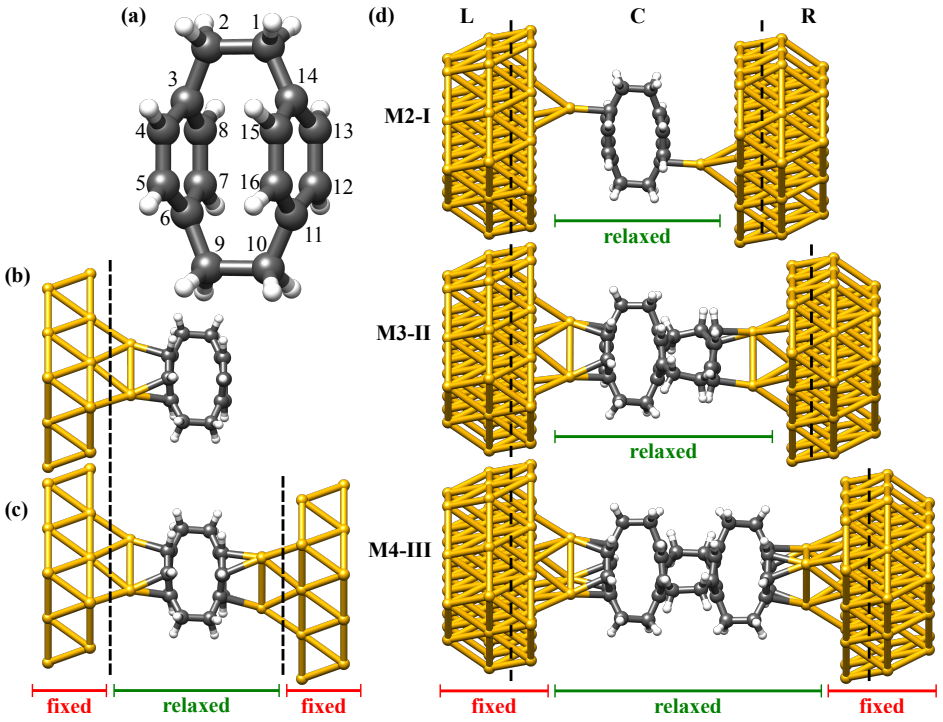

Figure 4.2: Example for ECCs used in our study. We show how we divide the ECC structure into L, C and R regions, by means of black dashed lines.

4.1 Geometry of paracyclophane molecules connected to electrodes

To calculate the geometry as well as the electronic structure of the ECC, we use DFT with the PBE functional [31, 32] and the empirical dispersion correction [61]. As basis set we use the def-SV(P) basis [33], which is of split valence quality. The total energies are converged to a precision better than 10^{-7} atomic units while the geometry optimization is carried out as long as the norm of gradients is bigger than 10^{-5} atomic units.

First we draw our attention to the smallest molecule used in this study. That is the paracyclophanes M2 which is shown in Fig. 4.2 (a). We measure the angles as well as the bond length of the optimized geometry as summarized in Tab. 4.1. Here we find a reasonable agreement for all calculated distances with literature [54, 62, 63]. Also the bending of the benzene plane $\alpha = 12.0°$ is close to the literature values. The twist angle of the two benzene fragments $\gamma_{14-1-2-3} = 0.47°$ is small compared to the literature. The reason for this might be the rather small basis set that is applied. However, since that angle increases if the molecule is attached to electrodes in the ECC geometry to about $5°$, we can accept that deviation.

We construct the ECC to mimic the geometry of a molecular junction, as shown in Fig. 4.2 (d). Because the detailed atomistic structure of the contact geometry is not provided by experiments, we use different electrode geometries to account for different binding motifs, that might be realized in experiments. As shown in Fig. 4.1 (b), we choose 3 different geometries for the electrodes, which differ in the number of adatoms on top of the gold surface. The electrodes are cut out of a fcc lattice structure with lattice constant $a = 4.08$ Å, including 49 gold atoms plus adatoms on both sides.

We use the procedure shown in Fig. 4.2 (b-c) to construct the ECC. First we calculate the ground state geometry of the molecules M2, M3 or M4 in front of one electrode of type III. The molecule was located above the adatoms. From the relaxed geometry

	PBE+D	B3LYP [63]	Siesta (PBE) [54]	MP2 [62]	exp. [63]
d_{1-2} (Å)	1.61	1.611	1.609	1.5856	1.593
d_{2-3} (Å)	1.51	1.503	1.510	1.5080	1.508
d_{3-4} (Å)	1.41	1.400	1.404	1.4033	1.399
d_{3-8} (Å)	1.41	1.399	1.404	1.4033	1.399
d_{4-5} (Å)	1.40	1.389	1.397	1.3952	1.396
d_{3-14} (Å)	2.80	2.827	2.793	2.7664	2.782
d_{8-13} (Å)	3.11	3.156	3.106	3.0727	3.097
$\gamma_{14-1-2-3}$	0.47	0	8.85	21.82	12.6
$180° - \gamma_{5-8-4-3} = \alpha$	12.01	13.0	-	-	12.5

Table 4.1: Comparison of our calculated geometry with theory and experiments. The atoms are numbered as shown in Fig. 4.2 (a).

we construct the position of the second electrode by inverting at the central point of the molecule. The obtained geometry is shown in Fig. 4.2 (c). The ECCs with electrode I and II are obtained by removing the respective gold atoms. The equilibrium structure is determined while varying the position of all atoms in the region marked as "relaxed" in Fig. 4.2. All the positions of the atoms marked as “fixed” are frozen during the geometry optimization. Finally we add a third layer of gold atoms in the fixed region to obtain the ECCs, as shown in Fig. 4.2 (d).

In total we construct 9 different ECCs, where each of the three molecule is combined with each of the three electrode geometries. Here we restrict ourself to ECCs with the same electrodes on the left and right side.

The bond between gold electrodes and paracyclophane molecule does not utilize special anchor groups that are usually necessary to establish the molecule-metal bond in molecular electronics. We analyze that binding energy E_b of the bond between electrodes and molecule. That energy is calculated by cutting off one electrode from the ECC and determining the total energy of the fragments,

$$E_b = E_{\text{ECC}} - E_1 - E_2. \tag{4.1}$$

The total energy of the ECC structure is E_{ECC}. The total energy of the electrode (ECC minus one electrode) is E_1 (E_2). Here we neglect the basis set superposition error. We summarized the calculate binding energies in Tab. 4.2. We find that the typical binding energy of paracyclophanes to gold electrodes is high compared to those determined for octane with amine-anchors (about 0.92 eV) and lower than for thiol-anchors (about 1.76 eV) [40]. Our results are almost twice the value reported by Ref. 60, where the binding energy between gold dimers and paracyclophane was calculated. The binding between molecule and electrode involves the benzene π orbitals that point towards the electrodes. Due to the stress applied by the ethane chains, by fixing the distance between the benzens, the π electrons of the outer benzenes are pushed out of the molecule. This allows to form a direct metal π bond.

4.2 Charge transport

In this section we describe the charge transport through paracyclophane molecules. In order to describe the molecular electron energies accurately, we add the DFT+Σ correction. The obtained electronic structure is used to calculate the transmission, the conductance as well as the transmission eigenchannels. We find that the transmission of the

E_b	I	II	III
M2	1.30 eV	1.39 eV	1.29 eV
M3	1.39 eV	1.60 eV	1.54 eV
M4	1.43 eV	1.68 eV	1.61 eV

Table 4.2: Binding energy E_b.

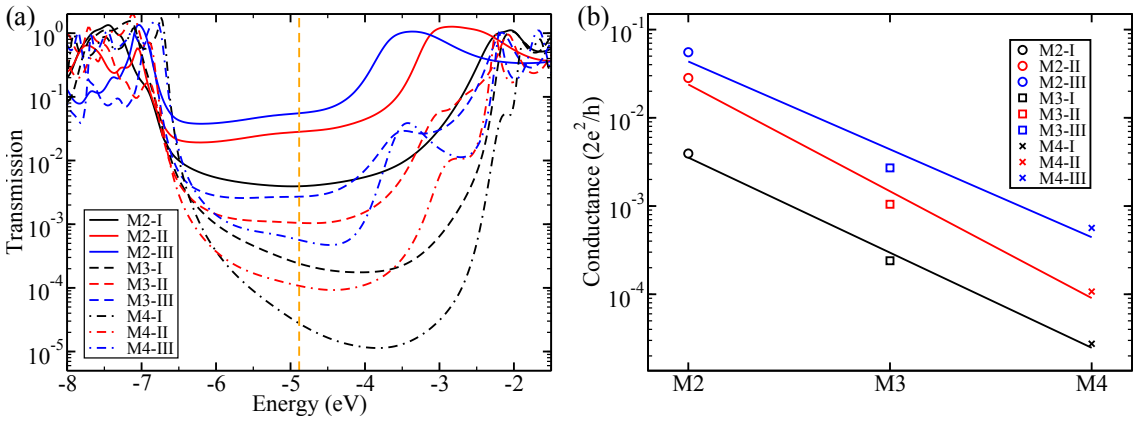

Figure 4.3: Transmission as a function of energy (a) and conductance as a function of the molecular length (b). The Fermi energy $E_F = -4.884$ eV is indicated by the orange dashed vertical line.

paracyclophanes is mostly carried by their π electron system. This can be seen by analyzing the transmission eigenchannels.

4.2.1 Correction of the level alignment due to image charge effects in metal electrodes

We use DFT with a self energy correction, known as DFT+Σ, to determine charge transport properties of the molecular contacts in the framework of the Landauer-Büttiker formalism [64–67]. The DFT+Σ approach was introduced in molecular electronics to cure some known deficiencies of DFT [67, 68]. It is well known that DFT, using GGA functionals, tends to underestimate the highest occupied molecular orbital (HOMO)-lowest unoccupied molecular orbital (LUMO) gap. Usually that results in a overestimated conductance of the molecular junctions, compared to experiments. DFT+Σ tries to overcome such deficiencies by correcting the HOMO-LUMO gap.

For the isolated molecule, the HOMO energy ϵ_H shall coincide with the ionization potential (IP) and the LUMO energy ϵ_L shall be the electron affinity (EA). Those energies are calculated using:

$$\text{IP} = E(Q = +e) - E(Q = 0), \quad \text{EA} = E(Q = 0) - E(Q = -e) \tag{4.2}$$

Here $E(Q = +e)$ is the total energy of the molecule with one electron removed, $E(Q = -e)$ is the total energy of the molecule with one extra electron and $E(Q = 0)$ is the total energy of the uncharged molecule.

If the molecule is located close to a conducting surface, then image charges will be induced in the metal. Here it is important that the spatial probability distribution of electrons occupying certain molecular levels is not uniform. For that the energy of that orbitals is shifted accordingly. To approximate that effect, we calculate the charges on the molecule inside the ECC. Therefore we extract from the Hamiltonian H and the overlap matrix S

	I	II	III
α	$0.04G_0$	$0.39G_0$	$0.43G_0$
β	2.49	2.79	2.29

Table 4.3: α and β obtained by an exponential fit to the conductance shown in Fig. 4.3 (b).

the part that belongs to the molecule. By using the extracted H^{mol} and S^{mol} we solve the KS equations for this subsystem:

$$\sum_{\mu} \left(H^{\text{mol}}_{\nu\mu} - \epsilon_m S^{\text{mol}}_{\nu\mu} \right) c_{\mu m} = 0 \tag{4.3}$$

To find the corrections for the HOMO and LUMO levels, we calculate the local charges by using the Mulliken population analysis. Those charges of the molecular orbital m, localized on atom A are:

$$Q^m_A = \sum_{\mu \in A} \sum_{\nu} c_{\nu m} S^{\text{mol}}_{\nu\mu} c_{\mu m}, \tag{4.4}$$

where the first sum runs over all basis functions located on atom A. The energy shift for occupied orbitals Δ_{occ} and unoccupied orbitals Δ_{virt} due to image charges is then calculated by using classical electrostatics as in Ref. [67]. Finally the energy of the KS orbitals of the ECC is shifted as:

$$\Sigma_{\text{occ}} = -IP - \epsilon_H + \Delta_{\text{occ}}, \quad \Sigma_{\text{virt}} = -EA - \epsilon_H + \Delta_{\text{virt}}. \tag{4.5}$$

With this shift we correct the HOMO-LUMO gap of the isolated molecules and consider we add the classical contribution to image charge effects. For the image charge effects we use the charge distribution of the HOMO (LUMO) for all occupied (virtual) orbitals, respectively.

4.2.2 Conductance

In Fig. 4.3 (b) we show the conductance as a function of the molecule length. With increasing number of stacked benzene rings N (i.e. $N = 1$ for M2, $N = 2$ for M3, $N = 3$ for M4) we find that the conductance decays exponentially as given by

$$G(N) = \alpha \exp\left\{-\beta \cdot N\right\}. \tag{4.6}$$

We summarize the results of the best fits in Tab. 4.3. For different types of binding motives the decay β is similar, but the contact conductance α increases with increasing number of ad-atoms.

To compare with experiments we average over the different electrode geometries and find: $\bar{\beta}_{th} = 2.52$ and $\bar{\alpha}_{th} = 0.29G_0$. Therefore our results are in reasonable agreement with experiment $\beta_{exp} = 1.94$ and $\alpha_{exp} = 0.060G_0$ [60].

4.2.3 Transmission and transmission eigenchannels

The energy-dependent transmission of the molecular junctions is shown in Fig. 4.3. The resonances of the transmission are about 2 eV above and below the Fermi energy. The width of the resonances reveals the coupling strength of the conducting molecular orbitals, that results from a comparison with the single level model. Here we find that the width decreases with increasing molecular length. The narrowing of the resonances is the dominant reason that results in a decrease of the conductance for longer molecules.

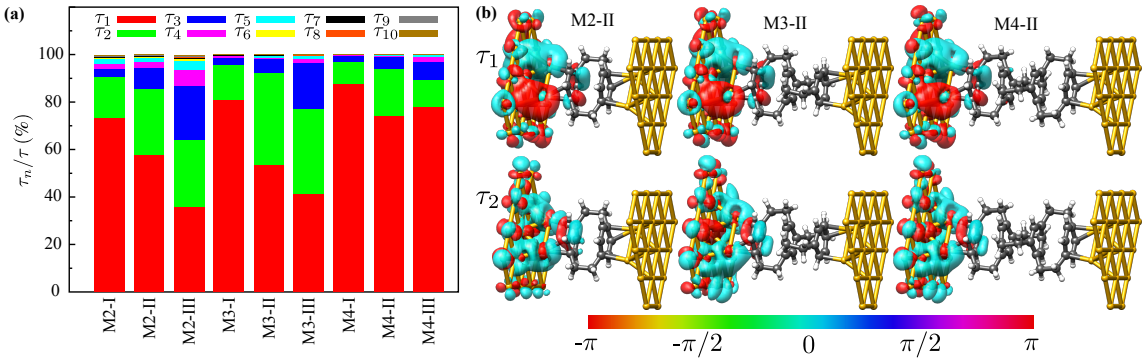

Figure 4.4: The histogram (a) shows the percentage of the 10 dominant conductance channels τ_n relative to the transmission τ. The wavefunctions of the two dominant, left-incoming transmission eigenchannels, for selected ECCs in (b). The wavefunction is mostly real. The color code shows the sign of the isosurface.

To determine the conduction mechanism, we calculate the transmission eigenchannels τ_n [65, 69]. As shown in the histogram of Fig. 4.4 (a), there are several contributing transmission channels. The first two always contribute more than 60%. From the isosurface plot of the transmission eigenwavefunctions, as shown in Fig. 4.4 (b), we find that the charge transport is due to the π-system of the benzene rings. The character of the first transmission channel is close to the HOMO of the isolated molecule M2.

4.3 Inelastic electron tunneling spectra

To show the influence of vibrational modes on the electrical properties, we plot the IETS in Fig. 4.5. In the following discussion we will focus on one selected feature of the IETS. In Fig. 4.5 we mark the features with P at about 0.13 V. It is mostly independent of the electrode geometry. The corresponding vibrational modes show a unique character. The modes that contribute most to that feature can be characterized as carbon-carbon stretch (C-C stretch) modes, while the displacement of the atoms of the benzene rings is within the benzene plane. The vibrational mode for molecules M3 and M4 is confined on the carbon atoms of a central benzene fragment, which is not connected to the electrodes. For molecule M2 a central benzene fragment is absent. In this case similar vibrational modes are observed at the benzene which is connected to the electrodes. Here we find a shift to higher energies at about 0.15 V.

More globally we see that in-plane modes (i.e. modes where the direction of motion of the carbon atoms is in the plane of the benzene fragment) dominate the IETS above voltages of 0.11 V. Below that threshold we find that vibrational modes tend to show an out-of-plane character.

We speculate that the tilted nature of the central benzene group shifts the vibrational modes with respect to the typical benzene vibration spectrum and the tilted form is easily affected by changes of the environment, such as different electrode geometries.

4.4 Conclusions

Motivated by recent experiments [60], we performed a theoretical analysis of the electric properties of molecular wires built with multilayered paracylophanes. The main focus was on analyzing their conductance eigenchannels as well as their IETS.

To probe the robustness of the calculated conductance with respect to geometric modifications, we used various junction geometries. We found that the gold benzene binding

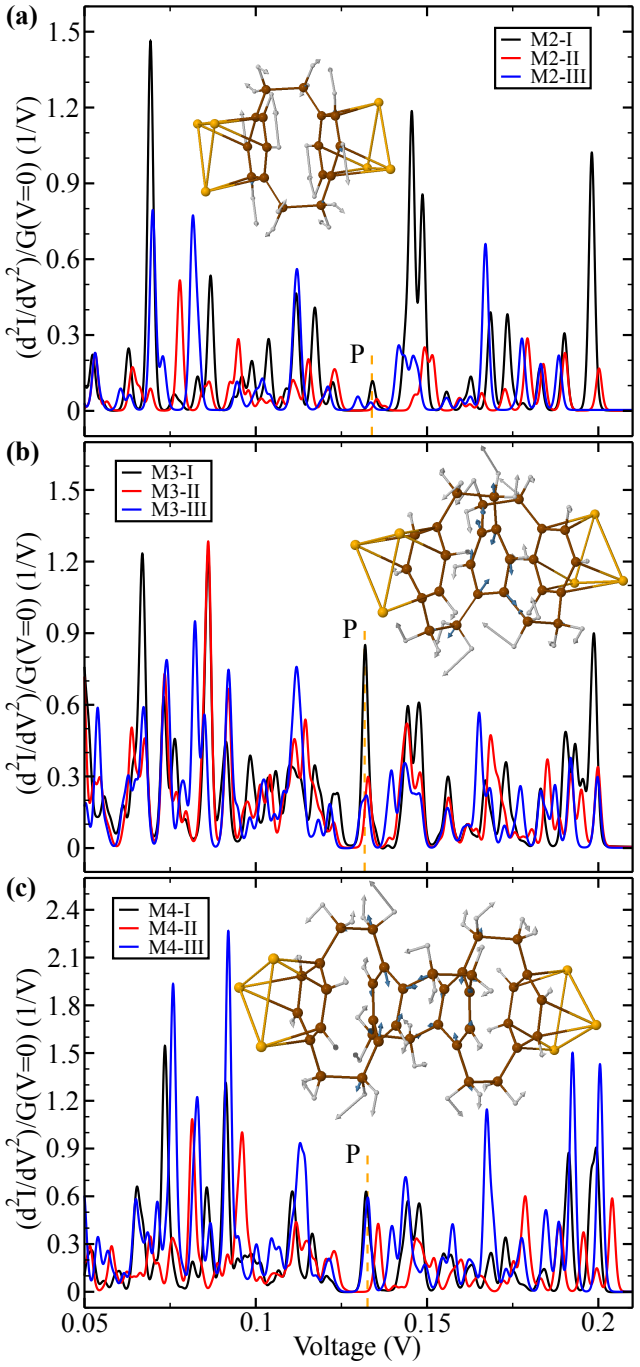

Figure 4.5: IETS for voltages in the interval $[50\,\text{mV}, 210\,\text{mV}]$ for M2 (a), M3 (b) and M4 (c). Here we use the ECC, constructed with contacts I, II and III (see Fig. 4.2). The label P indicates the position of the feature discussed in the text. The insets show the character of the vibrational modes which create the feature P.

does not affect the transmission path much. The dominant transmission channels, or their respective wavefunctions, show that transport is mainly carried by the π-system of the stacked benzene rings. By analyzing the length dependence of the conductance, we found an exponential law.

We analyzed the geometric properties of vibrational modes that create features in the IETS. Here we drew special attention to the character of one feature of this spectrum. We observed a global trend that in-plane modes are present above 110 mV and out-of-plane modes at lower energies.

5 Inelastic electron tunneling spectroscopy in molecular junctions in case of destructive quantum interference

Spectroscopic methods are widely used to characterize the molecular geometry or lattice structure of solids. In molecular junctions, optical spectroscopy cannot be applied easily due to several reasons. The electromagnetic fields is screened by the metal leads. If the electrodes absorb light, their temperature rises which eventually destroys the molecular junction because of thermal expansion of the leads. However in molecular junctions the vibrations of the molecules can be probed using the electron-vibration interaction. Measuring the inelastic electron tunneling spectroscopy (IETS) allows, in principle, to identify the vibrational modes of a molecule in a single-molecule junction. The IETS show no clear and simple selection regarding the symmetry of the vibrational modes, comparable to those known for infrared spectroscopy or Raman spectroscopy. In this chapter we will use a tight-binding model that includes the π electron orbitals of the molecule. Within that model we calculate the IETS. Previously a similar tight binding model was used to predict the quantum interference for the elastic transport through molecular junctions [70]. The quantum interference leads to a suppression of the elastic electron transmission at a resonance energy. The first experimental evidence was found in the I-V characteristics, namely the zero bias anomaly was explained by destructive quantum interference [71]. The IETS might reveal additional insight on the quantum interference features [72].

To gain further insight on the origin of the quantum interference effect, we will briefly discuss its occurrence in benzene molecular junctions. Here the quantum interference occurs for benzene coupled to the leads via the meta position [70, 73]. It is possible to give a qualitative explanation similar to the Aharonov-Bohm effect. We assume that electrons can be described by plane waves traveling along the ring with $A_+e^{ikd} + A_-e^{-ikd}$ where d was the electron path length and k the wave vector [74]. The amplitudes $A_\pm$ of the electrons traveling in the left/right direction respectively is determined by the coupling to the left lead. If the second electrode couples to a site where the wave function shows a node, the conductance is suppressed. Here we will focus on how the quantum interference affects the IETS.

The tight-binding model used to model the quantum interference is described in Sec. 5.1. Subsequently the known formulas to calculate the IETS are presented in Sec. 5.2, where we simplify them due to the tight binding model. In Sec. 5.3 we present our first principles calculations on molecular junctions that show the quantum interference feature. Finally, in Sec. 5.4, we extract the tight-binding parametrization for the π electron system from the first principles calculations.

5.1 Suppression of elastic electron transport

In this section we describe the tight-binding model that predicts the suppression in the transmission of a molecular junction [70]. This model includes sites numbered from 1 to N with on-site energy ϵ and nearest neighbor coupling t. The electrodes to the left and right are coupled at site 1 and N. Those sites are also referenced by $|\mathrm{L}\rangle$ and $|\mathrm{R}\rangle$ respectively. The transmission can be calculated using the expression introduced in Eq. (2.23). We can evaluate the transmission directly due to the coupling of the electrodes to one site only $\mathbf{\Gamma}_X = |\mathrm{X}\rangle \langle \mathrm{X}| \Gamma$ for $\mathrm{X} \in \{\mathrm{L}, \mathrm{R}\}$:

$$T = \Gamma^2 \left| \langle \mathrm{L}| \boldsymbol{G}^r |\mathrm{R}\rangle \right|^2 . \tag{5.1}$$

Here we need to determine one element of the Greens function G^r that describes electrons on the sites 1 to N. To calculate G^r we need to invert a $N \times N$ matrix. That matrix inversion is carried out by means of the Cramer's rule:

$$\langle \mathrm{R}| \boldsymbol{G}^r |\mathrm{L}\rangle = (-1)^{N+1} \frac{\det_{1N} (E - \boldsymbol{H})}{\det (E - \boldsymbol{H} - \boldsymbol{\Sigma}_L - \boldsymbol{\Sigma}_R)}, \tag{5.2}$$

where $\det_{1N}$ is the determinant of the matrix with column 1 and row N removed. The embedding self-energy is $\mathbf{\Sigma}_X = -i/2 \, |\mathrm{X}\rangle \langle \mathrm{X}| \Gamma$ of the lead $\mathrm{X} \in \{\mathrm{L}, \mathrm{R}\}$. The transmission is suppressed, if the numerator in Eq. (5.2) is zero. If this suppression appears at the Fermi energy, the conductance of the molecular junction is zero. Two simple examples for molecular geometries that show destructive quantum interference are:

1. A site that is coupled perpendicular to the current carrying link [75]:

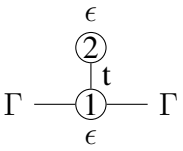

$$\Longrightarrow \boldsymbol{G} = \begin{pmatrix} E - \epsilon + i\Gamma & -t \\ -t & E - \epsilon \end{pmatrix}^{-1} \tag{5.3}$$

   here the transmission is proportional to:

$$T \sim \left| \det_{1N} (E\mathbf{1} - \boldsymbol{H}) \right|^2 = (E - \epsilon)^2 . \tag{5.4}$$

   Therefore the conductance is suppressed by the antiresonance if the Fermi energy is $E_F = \epsilon$.

2. The second example is a cyclic configuration with the geometry:

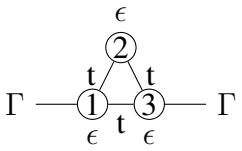

$$\Longrightarrow \boldsymbol{G} = \begin{pmatrix} E-\epsilon+i\Gamma & -t & -t \\ -t & E-\epsilon & -t \\ -t & -t & E-\epsilon+i\Gamma \end{pmatrix}^{-1} \tag{5.5}$$

The transmission is:

$$T \sim \left|\det{}_{1N}\left(E\mathbf{1}-\boldsymbol{H}\right)\right|^2 = t^2(E-\epsilon+t)^2 \tag{5.6}$$

Hence we expect to find zero conductance, if the Fermi energy is $E_F = \epsilon - t$.

5.2 Inelastic electron tunneling spectra

Due to the electron-phonon interaction it is possible to probe the vibrational spectra by measuring the inelastic signal in the IV (i.e. measuring the IETS). Here we will calculate the IETS within the tight-binding model that was described in the last section. We assume that the Fermi energy is close to the quantum interference feature and that the wide-band limit is still a good approximation. We calculate the inelastic contribution to the current as given in Eq. (2.57). The self-energies due to the electron-phonon coupling can be calculated by using non equilibrium Greens function formalism [13, 14, 76]. A closer look reveals that the contributions from δI_{el} vanish, or they depend linearly on the applied voltage at the point of destructive quantum interference. Therefore it is negligible for the IETS. For the IETS the dominant term is:

$$I_{\text{inel}} = G_0 \sum_\alpha T_\alpha^{\text{in}} \int_0^\infty \mathrm{d}E \rho_\alpha\left(E\right) \tag{5.7}$$

$$\left[2N_\alpha\left(E\right)U + \left(E-U\right)n\left(E-U\right) - \left(E+U\right)n\left(E+U\right)\right], \tag{5.8}$$

where $n\left(E\right) = 1/\left[\exp\left(\beta E\right)-1\right]$ is the Bose function and N_α is the energy distribution function of the vibrational quanta [13, 14]. We drop the term that includes N_α because it is almost linear in the applied voltage U, and therefore its contribution to the second derivative is assumed to be weak. We assume that the phonon spectral function can be approximated with a delta function $\rho_\alpha \approx \delta\left(E-\hbar\omega_\alpha\right)$. By applying these approximations, we finally find:

$$I_{\text{inel}} = G_0 \sum_\alpha T_\alpha^{\text{in}} \left[\left(\hbar\omega_\alpha - U\right)n\left(\hbar\omega_\alpha - U\right) - \left(\hbar\omega_\alpha + U\right)n\left(\hbar\omega_\alpha + U\right)\right]. \tag{5.9}$$

From Refs. [13, 14, 76]:

$$T_\alpha^{\text{in}} = \text{Tr}\left[\boldsymbol{G}^r\boldsymbol{\Gamma}_{\text{R}}\boldsymbol{G}^a\boldsymbol{\lambda}^\alpha\boldsymbol{G}^a\boldsymbol{\Gamma}_{\text{L}}\boldsymbol{G}^r\boldsymbol{\lambda}^\alpha\right]\big|_{E_F}, \tag{5.10}$$

where the electron-phonon coupling $\boldsymbol{\lambda}^\alpha$ is given in Eq. (2.54). The relative peak height in the IETS is given by T_α^{in}. Once again, we use that the coupling to the leads is given by $\boldsymbol{\Gamma}_X = \left|\text{X}\right\rangle\left\langle\text{X}\right|\Gamma$ and we can write:

$$T_\alpha^{\text{in}} = \Gamma^2\left|\left\langle\text{L}\right|\boldsymbol{G}^r\boldsymbol{\lambda}^\alpha\boldsymbol{G}^r\left|\text{R}\right\rangle\right|^2 \tag{5.11}$$

To simplify this expression, we used the cyclic permutation within the trace. This expression is similar to Eq. (5.1). At the energy of destructive quantum interference we can use the scheme developed in Ref. [70] using the replacement

$$\boldsymbol{H} \to \boldsymbol{H} + \boldsymbol{\lambda}^\alpha \tag{5.12}$$

At least to the first order expansion in $\boldsymbol{\lambda}^{\alpha}$ that replacement is valid. We find, by using the Dyson equation:

$$\langle \mathrm{R}| \boldsymbol{G}^{r}_{\alpha} |\mathrm{L}\rangle = \underbrace{\langle \mathrm{R}| \boldsymbol{G}^{r} |\mathrm{L}\rangle}_{=0} + \langle \mathrm{R}| \boldsymbol{G}^{r} \boldsymbol{\lambda}^{\alpha} \boldsymbol{G}^{r} |\mathrm{L}\rangle \,. \tag{5.13}$$

At the energy of destructive quantum interference the first term vanishes. Therefore we can calculate the IETS intensity of the mode α by:

$$\langle \mathrm{R}| \boldsymbol{G}^{r}_{\alpha} |\mathrm{L}\rangle = (-1)^{N+1} \frac{\det{}_{1N} \left(E\mathbf{1} - \boldsymbol{H} - \boldsymbol{\lambda}^{\alpha}\right)}{\det \left(E\mathbf{1} - \boldsymbol{H} - \boldsymbol{\lambda}^{\alpha} - \boldsymbol{\Sigma}_{L} - \boldsymbol{\Sigma}_{R}\right)}. \tag{5.14}$$

If we add the electron-phonon interaction to the two examples from the last section we find:

1. The IETS amplitude of mode α vanishes at the destructive quantum interference if the electron vibration coupling satisfies $\lambda^{\alpha}_{22} = 0$.

2. Here the IETS signal of mode α vanishes if the condition $(t + \lambda^{\alpha}_{21})(t + \lambda^{\alpha}_{32}) = (t + \lambda^{\alpha}_{31})(t + \lambda^{\alpha}_{22})$ is fulfilled.

5.3 Destructive quantum interference revealed by first principles calculations

In this chapter we present our first principle calculations to determine the properties of IETS close to the destructive quantum interference feature. For this purpose we investigate the destructive quantum interference features for 3 different molecules attached to leads by thiol anchors. We model the molecular junction by an ECC that includes the molecule and two gold electrodes with 20 atoms each. We used DFT as implemented in the quantum chemistry package TURBOMOLE [24] with the PBE functional [31, 32] and the def-SV(P) basis set [33]. The central part of the ECC is shown in Fig. 5.1 (a).

For the cross-conjugated (CC) molecule and the cross-conjugated molecule with blocked sigma channel (CCB) we expect to find the destructive quantum interference feature close to the Fermi energy [72, 77]. The linear-conjugated (LC) molecule serves as a test system for comparison.

The transmission obtained by first principles calculations, shown in Fig. 5.1 (b), displays a decrease when going from the CC and the LC molecule by a factor of about 10 at the Fermi energy. The destructive quantum interference is not clearly visible in the transmission of the CC molecule. However the analysis of the transmission channels for the CC molecule reveals that the destructive quantum interference lies within an energy range of 0.002 eV around the Fermi energy. But the dominant transmission channel $\mid \phi^{(1)}_{\mathrm{CC}} \rangle$ does not include the molecular π orbitals. It is rather created by the p orbitals in the molecular plane, as shown in the inset of Fig. 5.1 (b). This transmission channel can be damped if hydrogen atoms bind to the carbon chain, as realized in the CCB molecule. The CCB molecule shows the destructive quantum interference clearly in the transmission at about -5.13 eV. The dominant transmission eigenchannel $\mid \phi^{(1)}_{\mathrm{CCB}} \rangle$ is due to the π orbitals of the carbon atoms as shown in the inset of Fig. 5.1 (b).

In Fig. 5.4 we show the IETS that results from the full first principles calculations. In order to calculate this tunneling spectrum, we chose the energy of the destructive quantum resonance as Fermi energy. For the CC molecule the antiresonance is at -4.9 eV, as obtained from the transmission channel analysis. For the CCB molecule we obtain

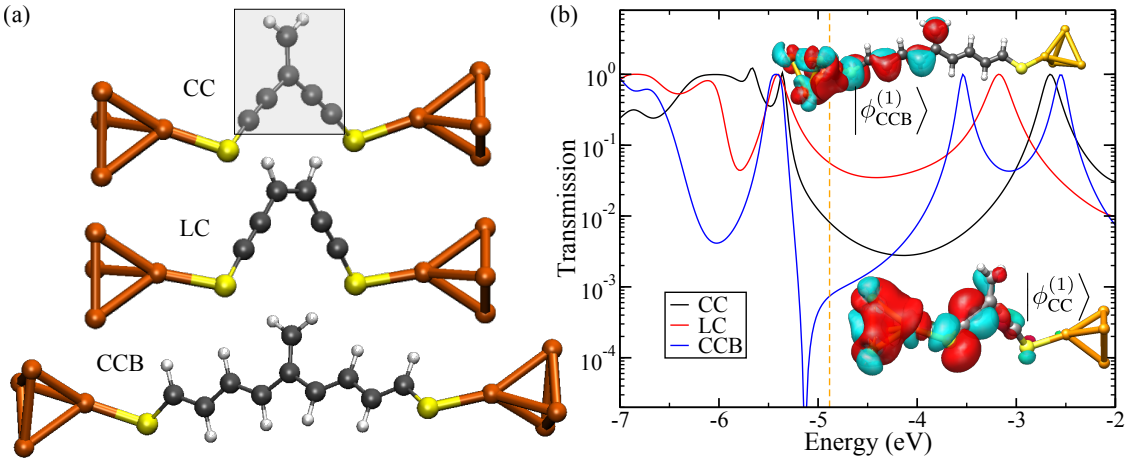

Figure 5.1: The geometry of the cross conjugated (CC), linear conjugated (LC) and the cross conjugated with blocked sigma channel (CCB) molecule in (a). In (b) we show the transmission of the full first principle calculation, with Fermi energy (orange dashed line). The inset shows the isosurface plot of the first transmission channel of the CC and CCB molecule at the Fermi energy (isoval 0.03).

-5.14 eV directly from its transmission, as shown in Fig. 5.1 (b). For the LC molecule the quantum resonance is absent, therefore we calculate the IETS at $E_F = -4.884$ eV, i.e. at the Fermi energy of the used gold ball with 429 atoms that resembles the bulk gold. Here we show the spectra for energies between 100 and 270 meV. We restrict ourselves to that energy window because we are not interested in the high energy hydrogen stretch modes at about 400 meV and at low energies the vibrational modes are not confined to several atoms.

Within the chosen energy range, we find for the CC molecule the following vibrational modes that create a feature in the IETS. They are the hydrogen wagging mode $\gamma_w\,(CH_2)$ at 108.49 meV, the double bond stretch and C-S stretch mode $\nu\,(C=C) + \nu\,(C\text{-}S)$ at 124.71 meV, the hydrogen scissor mode $\delta_s\,(CH_2)$ at 166.56 meV, the double bond stretch combined with the hydrogen scissor mode $\nu\,(C=C) + \delta_s\,(CH_2)$ at 185.19 meV and the symmetric triple bond stretch $\nu\,(C\equiv C)$ at 258.47 meV. Also we find modes that create a very small feature in the spectra. Those can be described by C-H_2 rocking mode at 123.52 meV, the antisymmetric C-S stretch combined with the C-H_2 rocking mode at 164.67 meV and the antisymmetric triple bond stretch at 257.67 meV.

For the LC molecule the IETS is dominated by the C_2H_2 twist mode $\gamma_t\,(C_2H_2)$ at 112.38 meV, the hydrogen scissor mode $\delta_s\,(C_2H_2)$ at 129.52 meV, the double bond stretch mode $\nu\,(C=C)$ at 182.92 meV and the triple bond stretch mode $\nu\,(C\equiv C)$ at 248.93 meV. Modes of the LC molecule in that energy range which couple weakly are best described by the C_2H_2 rocking at 147.41 meV, the C_2H_2 scissoring at 152.53 meV, the C_2H_2 rocking with C-C stretch at 177.87 meV and the antisymmetric triple bond stretch at 259.69 meV. The antisymmetric triple bond stretch does couple weakly and creates a dip in the IETS.

For the CCB molecule we only describe the modes that do create a feature in the IETS because there are too many modes. The C-S stretch mode $\nu\,(C\text{-}S)$ at 107.00 meV, the CH hydrogen out of plane wagging modes $\gamma^o_w\,(CH)$ at 110.88 meV, the CH hydrogen wagging modes $\gamma_w\,(CH)$ at 155.15 meV and 157.35 meV, the CH_2 hydrogen scissor mode $\delta_s\,(CH_2)$ at 171.07 meV, the double bond C-C stretch combined with the CH_2 hydrogen scissor mode $\nu\,(C=C) + \delta_s\,(CH_2)$ at 190.94 meV, the double bond C-C stretch with CH hydrogen wagging mode $\nu\,(C=C) + \gamma_w\,(CH)$ at 200.03 meV,

Generally the IETS is dominated by in-plane modes, i.e. those vibrations include only atoms which move inside the molecular plane. The out-of-plane modes are suppressed to some extent.

5.4 Tight binding model using first principles calculations

From the first principles calculations we extract the Hamiltonian that corresponds to the molecular system. This includes the six carbon atoms in the central part Fig. 5.1 (a). Then we fit the tight binding model to the extracted electronic subsystem as follows. First we identify the six molecular orbitals with energy E_i^{MO}, that involve the π orbitals, as shown in Fig. 5.2. Those eigenenergies E_i^{MO} are also obtained by diagonalizing the tight binding Hamiltonian:

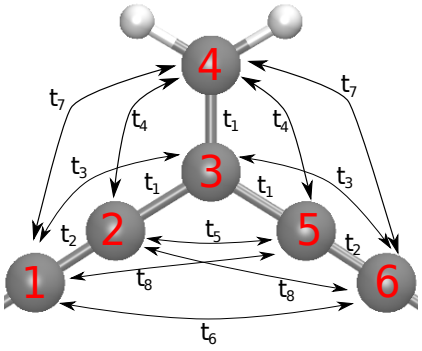

$$H^{\mathrm{TB}} = \begin{pmatrix} \epsilon & t_2 & t_3 & t_7 & t_8 & t_6 \\ t_2 & \epsilon & t_1 & t_4 & t_5 & t_8 \\ t_3 & t_1 & \epsilon & t_1 & t_1 & t_3 \\ t_7 & t_4 & t_1 & \epsilon & t_4 & t_7 \\ t_8 & t_5 & t_1 & t_4 & \epsilon & t_2 \\ t_6 & t_8 & t_3 & t_7 & t_2 & \epsilon \end{pmatrix} \tag{5.15}$$

with

$$\sum_{i,k} \left(C^T\right)_{ji} H_{ik}^{\mathrm{TB}} C_{kl} = \delta_{kj} E_k^{\mathrm{MO}} \tag{5.16}$$

The challenge is to find the inverse of the unitary transformation C of Eq. (5.16). The transformation C is calculated numerically using an iterative scheme.

We start with a guess for C. It can be used to invert Eq. (5.16). The tight binding parameters can then be approximated, while the proper symmetry from Eq. (5.15) is ensured

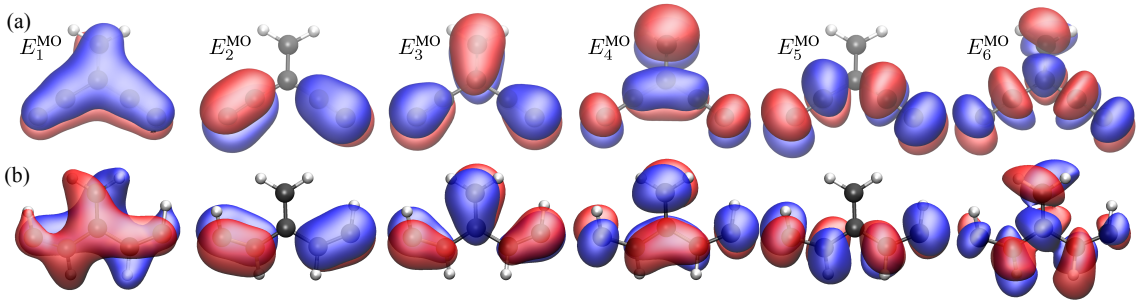

Figure 5.2: The molecular π orbitals extracted from the molecular fragments of the ECC. For CC (a) and CCB (b).

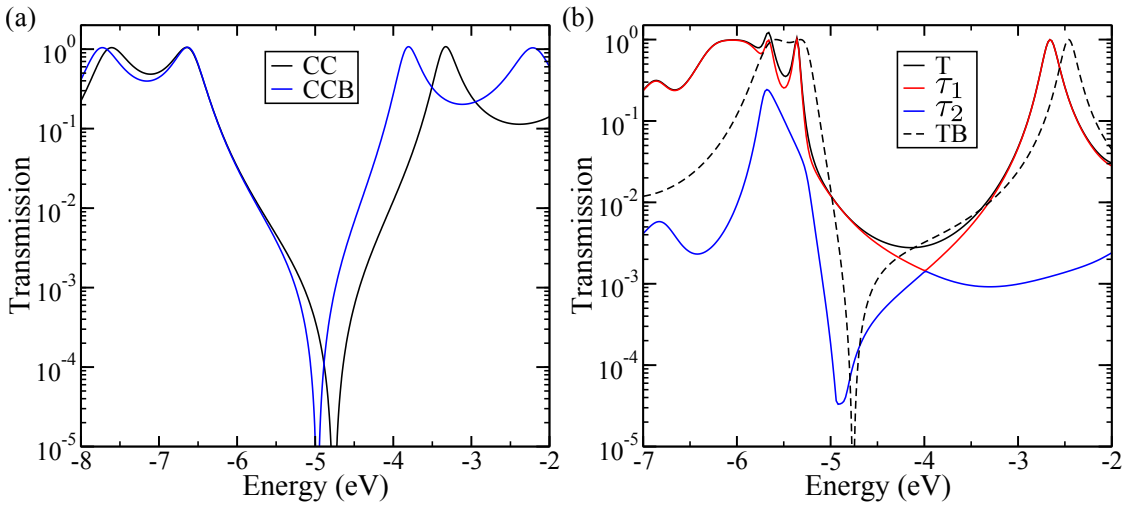

Figure 5.3: Transmission due to the tight-binding model that includes six carbon atoms (a). Transmission of the extended model for the CC molecule compared to the transmission channels of the full DFT calculation (b).

by using:

$$\epsilon = \left(H_{11}^{\mathrm{TB}} + H_{22}^{\mathrm{TB}} + H_{33}^{\mathrm{TB}} + H_{44}^{\mathrm{TB}} + H_{55}^{\mathrm{TB}} + H_{66}^{\mathrm{TB}}\right)/6 \tag{5.17}$$

$$t_1 = \left(H_{23}^{\mathrm{TB}} + H_{34}^{\mathrm{TB}} + H_{35}^{\mathrm{TB}}\right)/3 \tag{5.18}$$

$$t_2 = \left(H_{12}^{\mathrm{TB}} + H_{56}^{\mathrm{TB}}\right)/2 \tag{5.19}$$

$$t_3 = \left(H_{12}^{\mathrm{TB}} + H_{56}^{\mathrm{TB}}\right)/2 \tag{5.20}$$

$$t_4 = \left(H_{24}^{\mathrm{TB}} + H_{45}^{\mathrm{TB}}\right)/2 \tag{5.21}$$

$$t_5 = H_{25}^{\mathrm{TB}} \tag{5.22}$$

$$t_6 = H_{16}^{\mathrm{TB}} \tag{5.23}$$

$$t_7 = \left(H_{14}^{\mathrm{TB}} + H_{46}^{\mathrm{TB}}\right)/2 \tag{5.24}$$

$$t_8 = \left(H_{15}^{\mathrm{TB}} + H_{26}^{\mathrm{TB}}\right)/2 \tag{5.25}$$

These tight-binding parameters are then used to construct H^{TB} with the proper symmetries as given in Eq. (5.15). Then we obtain a new transformation C by diagonalizing H^{TB}, we use this C and start again, inverting Eq. (5.16).

This iteration is carried out until the eigenvalues E_i^{TB}, obtained by diagonalizing H^{TB}, coincide numerically with the eigenvalues from the DFT calculation E_i^{MO}. More precisely the value

$$\delta = \sum_i \mathrm{abs}\left(E_i^{\mathrm{TB}} - E_i^{\mathrm{MO}}\right)$$

shall fall below 10^{-8} eV.

Transmission

We use the tight-binding parametrization to calculate the transmission through the functional part, as shown in Fig. 5.3 (a). The functional part consists of 6 carbon atoms. In this studies we couple the electrodes via $\Sigma_X = -i\Gamma/2$ to site 1 and 6. The transmission due to the tight-binding model shows the destructive quantum interference feature. Unfortunately most of the other structure in the transmission, obtained with the full calculation, cannot be reproduced with this simple model. To reproduce the transmission obtained

from the full calculation, we need to add the additional site that accounts for the thiol anchors. In Fig. 5.3 (b) we compare this extended tight-binding model to the two dominant transmission channels of the CC molecule. We find that the channel that is suppressed at the destructive quantum interference is well described by the extended model. Since we are interested in the IETS close to the destructive quantum interference, we will stick to the tight-binding model of the functional part in the following.

IETS

To calculate the IETS within the tight-binding, model we need the electron-vibration coupling in the basis of the tight-binding model. To achieve this we use the transformation C to transform the electron-vibration coupling to the tight-binding model basis. The transformation C is obtained by the iterative scheme just described. Those electron-vibration coupling elements are then used to calculate the IETS, shown in Fig. 5.4 as dashed lines. By construction the tight-binding model only includes the π electron system and thus the IETS calculated shows only features due to modes that couple to these electron states. Therefore the comparison between the IETS of the first principles calculation and the tight-binding model reveals which modes couple to the π electron system.

We find that the IETS due to the tight-binding model shows smaller peak heights, compared to the full calculation. For the CC molecules the peaks due to $\gamma_{\mathrm{w}}\left(\mathrm{CH_2}\right)$, $\nu\left(\mathrm{C=C}\right) + \nu\left(\mathrm{C\text{-}S}\right)$ and $\nu\left(\mathrm{C\equiv C}\right)$ create a very small impact on the IETS of the tight binding model. On the other hand the modes $\delta_{\mathrm{s}}\left(\mathrm{CH_2}\right)$ and $\nu\left(\mathrm{C=C}\right) + \delta_{\mathrm{s}}\left(\mathrm{CH_2}\right)$ are observed clearly. The electron-vibration coupling matrix elements, shown in Fig. 5.4 as triangles, predict to some extent the tight-binding IETS peak heights. For the LC molecule we did not fit the tight-binding model because the destructive quantum interference is absent here.

For the CCB molecule, the tight-binding model is in reasonable agreement with the full calculations. Here modes either create a feature in both spectra or they are absent in the IETS. Therefore we conclude that although the molecular geometry is slightly twisted, the π orbital system describes the inelastic transport well.

5.5 Conclusions

To investigate the destructive destructive quantum interference feature we discussed three different molecular junctions. We showed two configurations which led to such a feature. We used a tight-binding (TB) model to describe that feature. Therefore we calculated the electronic structure with DFT and fitted the TB parameters to the p_z molecular orbitals. We focused on the transmission as well as on the IETS of the molecular junctions.

For the LC molecule the destructive quantum interference was not observed both in the model and the full calculation. For the CC molecule we found that the destructive quantum interference is suppressed because of a second transport channel. That channel does not involve the p_z molecular orbitals. The CCB molecule blocks that second transport channel found for the CC molecule. Therefore we obtained the destructive quantum interference feature in the transmission.

As we analyzed the IETS, calculated with the TB model, we found, that it fails to describe the correct peak height of the full IETS calculation. For the CCB molecule the TB model nevertheless allowed to select the modes that create a signal in the IETS. For the CC molecule the TB model did not describe IETS signal of the CH_2-wagging mode correctly. We assumed that this feature is created by the second transport channel that is not included in the TB model.

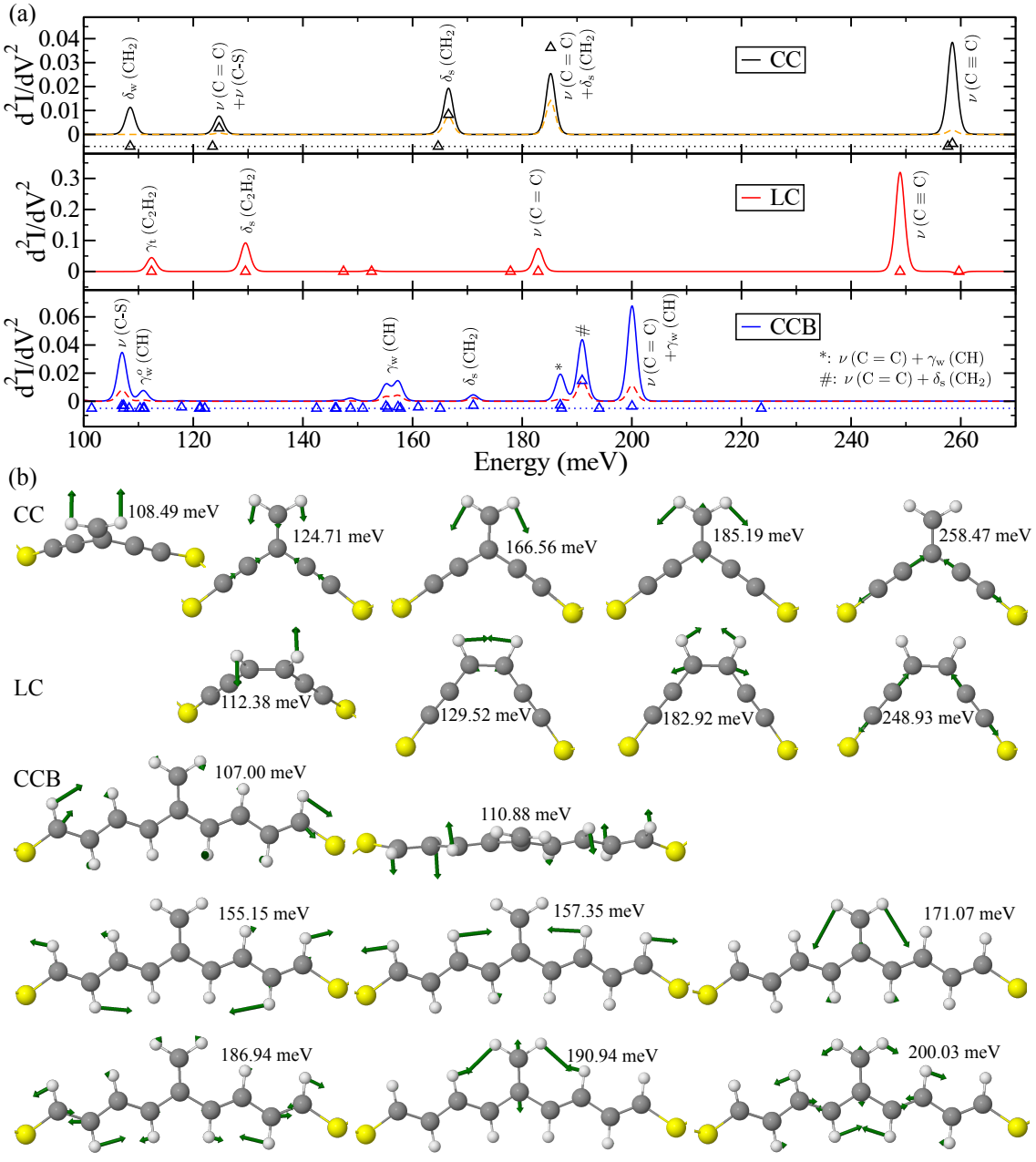

Figure 5.4: inelastic electron tunneling spectroscopy for the CC, LC and CCB molecule in (a). The full DFT calculation (solid line) are compared to the tight binding results (dashed). The value of $(\lambda_{44}^{\alpha})^2$ is depicted by the triangles; for sake of clarity those are shifted, the dotted line indicates $\lambda = 0$. In (b) we show some vibration modes.

6 Effect of dephasing on the electron transport through molecular wires

The typical size of molecules, used in molecular electronics, is about some ten Ångströms. For example the lattice constant of gold is 4.02 Å and the length of octane molecules is about 12 Å. But it is also possible to investigate much longer molecules. Polymerization techniques can control the length of molecules in a broad range. That allows to probe the crossover regime from coherent tunneling transport to incoherent hopping transport with molecular junctions, using molecules which were up to 9 nm long [78].

In this chapter we utilize a model to understand the effect of dephasing on the electronic transport through molecular junctions. We use a simple model that describes dephasing processes with the help of Büttiker probes and allows to investigate them within the Landauer Büttiker formalism without describing the scattering mechanism in detail [79–81].

6.1 Model for transport considering phase breaking processes

The Landauer-Büttiker formalism is used to describe coherent charge transport through a structure similar to these sketched in Fig. 6.1. Here the conductance from the left electrode with chemical potential μ_{L} to the right electrodes at μ_{R} is proportional to the trans-

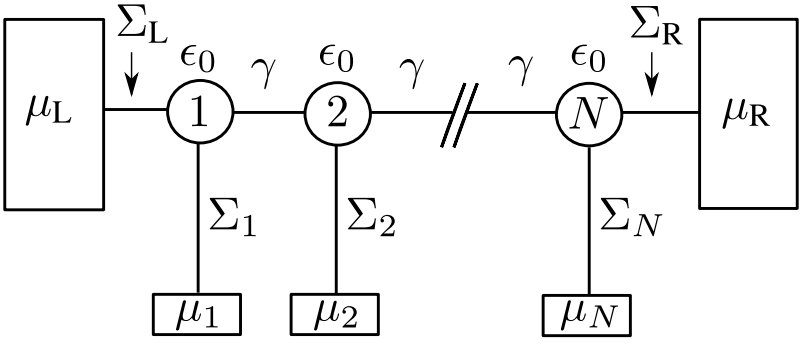

Figure 6.1: Model of the one-dimensional chain including inelastic scattering reservoirs which have a chemical potential $\mu_1, \ldots, \mu_N$, respectively.

mission at the Fermi energy

$$G = G_0 \tau \left(E_F \right). \tag{6.1}$$

The factor $G_0 = 2e^2/h$ is called the electrical conductance quantum. The magnitude of the thermopower is given by the Seebeck coefficient that can be calculated for small temperatures as

$$S = -S_0 \frac{\partial_E \tau(E)}{\tau(E)}\Big|_{E=E_F}. \tag{6.2}$$

Similar to the conductance quantum, we define $S_0 = \pi^2 k^2 T/3e$. For finite temperature the linear response expansion leads to [15, 28]

$$G = G_0 K_0 \left(T \right), \quad S = -\frac{K_1 \left(T \right)}{eTK_0 \left(T \right)}, \tag{6.3}$$

where $K_n = \int \tau \left(E \right) \left(E - E_F \right)^n \left[-\partial f \left(E, T \right) / \partial E \right] \mathrm{d}E$ was used, as derived in Eqs. 2.46 and 2.47.

To account for phase breaking effects, we couple Büttiker probes to each site i as shown in Fig. 6.1. These probes are electron reservoirs with a chemical potential μ_i adjusted such that the net current into the reservoir is zero. Thus, the electrons traveling from L to R can scatter into the channel i and are immediately replaced by a new electron with erased phase information. With this process the electrons can not change between states with different energies. How often that process occurs can be adjusted by the coupling between the Büttiker probes and the leads, determined by the embedding self energy Σ_i [80–82].

The current into reservoir i is:

$$I_i = \frac{2e}{h} \left[\left(1 - R_i \right) \left(\mu_i - \mu_\mathrm{R} \right) - \tau_{i\mathrm{L}} \left(\mu_\mathrm{L} - \mu_\mathrm{R} \right) - \sum_{\substack{l=1 \\ l \neq i}}^{N} \tau_{il} \left(\mu_l - \mu_\mathrm{R} \right) \right] \tag{6.4}$$

Here we used the definition $1 - R_i = \sum_{j \neq i} \tau_{ij}$ and the index j includes the leads L, $1 \ldots i-1, i+1 \ldots N$ and R. Using this formula, the chemical potential of the Büttiker probes μ_i can be adjusted such that the current I_i in each Büttiker probe i vanishes, as required. Subsequently the problem can be simplified and the chemical potentials μ_i are obtained by solving the linear equation

$$\underbrace{\begin{pmatrix} 1-R_1 & -\tau_{12} & \cdots & -\tau_{1N} \\ -\tau_{12} & 1-R_2 & \cdots & -\tau_{2N} \\ \vdots & \vdots & \ddots & \vdots \\ -\tau_{1N} & -\tau_{2N} & \cdots & 1-R_N \end{pmatrix}}_{=W} \begin{pmatrix} \mu_1 - \mu_\mathrm{R} \\ \mu_2 - \mu_\mathrm{R} \\ \vdots \\ \mu_N - \mu_\mathrm{R} \end{pmatrix} = \begin{pmatrix} \tau_{1\mathrm{L}} \\ \tau_{2\mathrm{L}} \\ \vdots \\ \tau_{N\mathrm{L}} \end{pmatrix} \left(\mu_\mathrm{L} - \mu_\mathrm{R} \right) \tag{6.5}$$

Here the transmission and the matrix W are symmetric because we do not apply a magnetic field.

The relative chemical potential at site m is:

$$\frac{\mu_m - \mu_\mathrm{R}}{\mu_\mathrm{L} - \mu_\mathrm{R}} = \sum_{i=1}^{N} \left(W^{-1} \right)_{mi} \tau_{i,\mathrm{L}} \tag{6.6}$$

Once the chemical potential at each Büttiker probe has been obtained we determine the current through the entire junction, using Eq. (6.4):

$$I_{\mathrm{R}} = \frac{2e}{h}\left[\tau_{\mathrm{RL}} + \sum_{l,s=1}^{N} \tau_{\mathrm{R}l}\left(W^{-1}\right)_{ls}\tau_{s\mathrm{L}}\right](\mu_{\mathrm{L}} - \mu_{\mathrm{R}})\,. \tag{6.7}$$

A comparison with Eqs. 6.1 and 2.23 allows to define an effective transmission

$$\tau_{\mathrm{eff}} = \underbrace{\tau_{\mathrm{RL}}}_{=\tau_{\mathrm{coh}}} + \underbrace{\sum_{l,s=1}^{N} \tau_{\mathrm{R}l}\left(W^{-1}\right)_{ls}\tau_{s\mathrm{L}}}_{=\tau_{\mathrm{inc}}}\,. \tag{6.8}$$

The first part is referred to as the coherent transmission τ_{coh}, because it describes electrons which pass the junction without scattering. The second part is called incoherent part τ_{inc} because it accounts for multiple scattering events.

The coherent transmission probability between site i and j can be calculated by

$$\tau_{ij} = \mathrm{Tr}\left\{\Gamma_i G^r \Gamma_j G^a\right\} \text{ for } i \neq j. \tag{6.9}$$

Here we used the Greens functions

$$G^r(E) = (E - H - \Sigma_L - \Sigma_R - \Sigma_D)^{-1} = [G^a(E)]^\dagger\,. \tag{6.10}$$

Assuming nearest-neighbor interactions with hopping parameter $\gamma > 0$ and on-site energies ϵ_0, we use the N-dimensional tight binding Hamiltonian H. The embedding self energies that couple the two leads at site L and R as well as the Büttiker probes at site i are defined as follows

$$(\Sigma_L)_{j,k} = -i\frac{\Gamma}{2}\delta_{j,1}\delta_{k,1}, \quad (\Sigma_R)_{j,k} = -i\frac{\Gamma}{2}\delta_{j,N}\delta_{k,N}, \quad (\Sigma_i)_{j,k} = -i\frac{\eta}{2}\delta_{j,i}\delta_{k,i}. \tag{6.11}$$

The scattering rate matrices are defined by $\Gamma_x = i\left(\Sigma_x - \Sigma_x^\dagger\right)$, where $x = L, 1, \ldots, N, R$.

In the following the coupling to the electrodes is set to $\Gamma = 0.5\gamma$. The phase randomization rate η adjusts the coupling of all Büttiker probes to the sites, where we use $\eta = 10^{-2}\gamma$, if not specified differently.

6.2 Incoherent transport in a one-dimensional chain

For the one-dimensional chain with N sites the coherent transport can be calculated analytically [83], and also all elements of the matrix W can be obtained analytically. Long chains develop a band with energies in the range $\epsilon_0 - 2\gamma < E < \epsilon_0 + 2\gamma$. In the limit of infinite chain length the Hamiltonian is diagonal in k-space $H_k \sim \epsilon_0 \pm 2\gamma \sin k$. Therefore we define three different transport regimes for the coherent transport.

Off-resonant transport: The energy is outside the band $E < \epsilon_0 - 2\gamma$ or $\epsilon_0 + 2\gamma < E$. Here the coherent transmission decreases exponentially with the length of the chain and the thermopower increases linearly.

On-resonant transport: The energy is inside the band $\epsilon_0 - 2\gamma < E < \epsilon_0 + 2\gamma$. The coherent transmission shows resonance energies which depend on the chain length. These resonance energies can be approximated by $E - \epsilon_0 = 2\gamma\cos\left(\frac{\pi}{\Delta N}\right)$. Where ΔN gives the period of the conductance oscillation as a function of the chain length. The thermopower as a function of chain length shows also oscillations with a period ΔN.

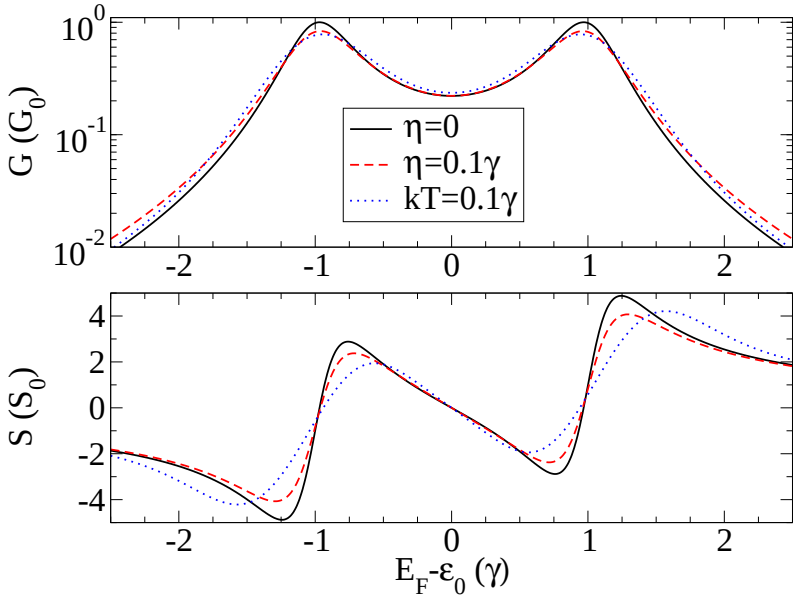

Figure 6.2: Influence of dephasing and finite temperature on transport. Conductance G and thermopower S as a functions of the Fermi energy. For a one-dimensional chain with $N = 2$.

Band-edge transport: The band edge regime is the crossover between the oscillations that occur in the on-resonant regime and the exponentially damped behavior in the off-resonant regime. In the limit of $E = \epsilon_0 \pm 2\gamma$ we find a suppression of the conductance that can be approximated by a power law $G \sim N^{-2}$ and the thermopower is $S \sim N(N+2)$, if N is big enough.

In the following discussion on incoherent transport we treat these three different regimes, as just defined, for the coherent transport separately.

Before we discuss the length dependence of the incoherent transport, we focus on one linear chain with two sites ($N = 2$). With this example we discuss the effect of incoherence as well as finite temperature on the energy-dependent transmission and Seebeck coefficient, as shown in Fig. 6.2. Adding dephasing leads to an increased transmission in the off-resonant regime, but the transmission decreases close to the resonance energies at about $\epsilon_0 \pm \gamma$. In the case of incoherent transport, the resonance becomes broader compared to the coherent transport. At finite temperature we find a qualitatively similar trend. Although the effect of finite temperatures is absent in the limit of big energies, that is not true for dephasing. The Seebeck coefficient tends to be smaller with dephasing compared to the coherent Seebeck coefficient. Finite temperature can also lead to an increase of the Seebeck coefficient.

Now we analyze the length dependence of the transmission and thermopower obtained for the one-dimensional chain. We discuss the effects of dephasing as well as finite temperature. To compare the results, we choose similar magnitudes for dephasing and finite temperature of $kT = 10^{-2}\gamma = \eta$ in our model calculation.

First we focus on the resonant transport at $E_F \approx 1.98423\gamma$ which corresponds to $\Delta N = 25$. In Fig. 6.3 (a) we find oscillation as a function of the molecular length. Finite temperature as well as dephasing damps those oscillations. In the case of incoherent transport the period of $\Delta N \approx 25$ is clearly visible, but this is not the case for finite temperature. For finite temperature the oscillation is damped before the first period is completed. The transmission as a function of energy oscillates within the band with a period of about kT for a chain longer than $N = 10$. Therefore the oscillations of the

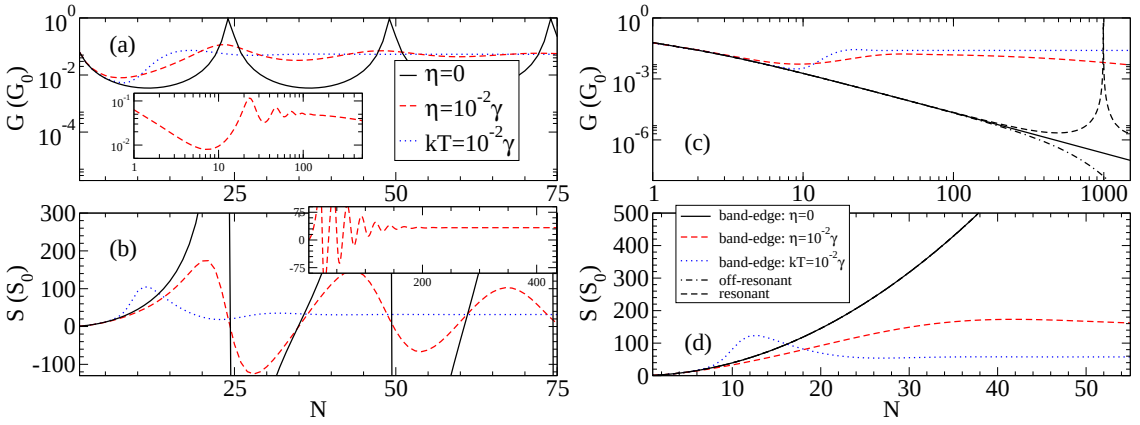

Figure 6.3: Coherent (black lines), incoherent (dashed red lines) transport for zero and finite temperature (dotted blue lines) through the one-dimensional chain as a function of the chain length. (a) Conductance and (b) thermopower for the resonant transport regime with a Fermi energy set according to the period $\Delta N = 25$. In the insets of (a) and (b) the length-dependent behavior for long chains is shown. (c) Conductance and (d) thermopower for the band edge regime at $E_F = \epsilon_0 + 2\gamma$. The limiting cases of resonant transport with $E_F = \epsilon_0 + (2 - \Delta)\,\gamma$ (dashed black) and off-resonant transport with $E_F = \epsilon_0 + (2 + \Delta)\,\gamma$ (dash-doted black) is shown, with $\Delta = 10^{-5}$.

transmission are integrated out and they cannot be observed in K_n, G or S as a function of chain length. The linear response calculations have to be treated carefully due to the strong oscillations in the transmission as a function of energy. In the inset of Fig. 6.3 (a) we show the incoherent transport in the limit of very long chains, and we find that the incoherent conductance as a function of the chain length decreases roughly as a power law for chains with length $N > 100$.

For the thermopower, as shown in Fig. 6.3 (b), we find a qualitatively similar picture as for the conductance. The oscillation is clearly visible and shows the same period in the case of coherent as well as incoherent transport, while the oscillations are damped in case of incoherence. In the limit of very long chains we find a constant value for the Seebeck coefficient shown in the inset of Fig. 6.3 (b). At finite temperature the oscillations of the Seebeck coefficient are damped, if the chain is longer than $N = 25$. However we observe an increase of the Seebeck coefficient for short chains, compared to the coherent case. That increase is obtained because the integral K_1 of Eq. (6.3) rises faster compared to K_0. The reason is that the first resonance of the band is approximately at $E_F - 3kT$. This coincides with the location of the maxima of $(E - E_F)\partial f/\partial E$. Therefore K_1 is peaked for chains with length of $N \approx 15$ and for the given Fermi energy of $E_F \approx 1.98423\gamma$.

In Fig. 6.3 (c) we plot the conductance of the band-edge regime. We observe the crossover between the oscillations of the resonant transport and the exponentially damped off-resonant transport. For the band-edge transport we find that the conductance as a function of chain length is described by a power law. From Fig. 6.3 (c) we extract an exponent of about two. If we assume finite temperature or dephasing the resonances of the transmission are broadened and the band-edge regime shows similar trends as observed for the coherent regime in the limit of long chains.

The thermopower of the band-edge regime is shown in Fig. 6.3 (d). In case of coherent transport we find that the thermopower follows approximately a $\sim N^2$ behavior. In case of incoherence or finite temperatures the Seebeck coefficient saturates in the limit of long chains. At finite temperature we also observe a quickly increasing thermopower for short

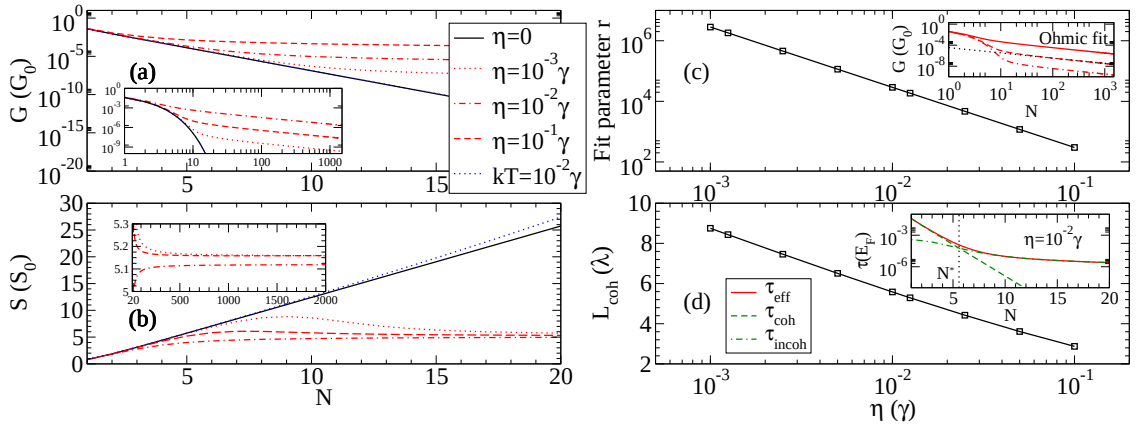

Figure 6.4: Transport in the off-resonant regime with $E_F = \epsilon_0 + 2.5\gamma$. Coherent (black lines), incoherent (dashed red lines) transport for zero and finite temperature (dotted blue lines) through the one-dimensional chain. (a) Conductance and (b) thermopower as a function of chain length. In the inset the length-dependent behavior for long chains is shown. (c) Fit parameter r of the ohmic fit as a function of the dephasing rate. The inset shows the fit using Eq. (6.12). (d) Phase coherence length over dephasing strength. The inset shows the coherent part and the incoherent part of the transmission. The intersection defines N^*.

chains. Again that is due to the contribution of resonances within the band to the integral of K_1, described in case of resonant transport.

In case of the off-resonant transport regime we find that the coherent conductance decreases exponentially with increasing chain length, as shown in Fig. 6.4 (a). If we assume a finite temperature that behavior does not change drastically. Adding dephasing effects results in a deviation from the exponential decrease. In the inset of Fig. 6.4 (a) we show a double log plot. We find that the incoherent transport follows a power law in the limit of long chains. The Seebeck coefficient, as plotted in Fig. 6.4 (b), shows a linear increase for the coherent case. Finite temperature leads to a slight increase of the Seebeck coefficient, compared to the coherence case. Incoherence leads to a saturation of the thermopower for long chains. Here the limit depends on the dephasing strength as shown in the inset. For small values of the phase randomization rate η the thermopower has a maximum at small chain length. This maximum disappears in case of $\eta > \eta_{\text{crit}} \approx 0.034\gamma$.

6.2.1 Ohmic behavior and phase coherence length

For long chains an Ohmic behavior is obtained for most macroscopic conductors. This means that the resistance of a conductor depends linearly on the length. Therefore we analyze the length dependent transport of the one-dimensional chain including dephasing effects. Here we focus on very long chains. We found already that for long chains the conductance is a straight line in the double logarithmic plot for all three energy regimes. Here we focus on the off-resonant regime. We fit the conductance of the one-dimensional chains with the following function (Ohmic fit):

$$\frac{G}{G_0} = \frac{1}{rN}, \tag{6.12}$$

where $R = rN/G_0$ is the resistance from Ohm's law. In Fig. 6.4 (c) we show the results of the fit for different dephasing strengths. We find that the resistance decreases with increasing dephasing. In the inset of Fig. 6.4 (c) we show an example of a fit of Eq. (6.12) to the calculated conductance. For the fit we use one-dimensional chains with $100 < N < 1000$.

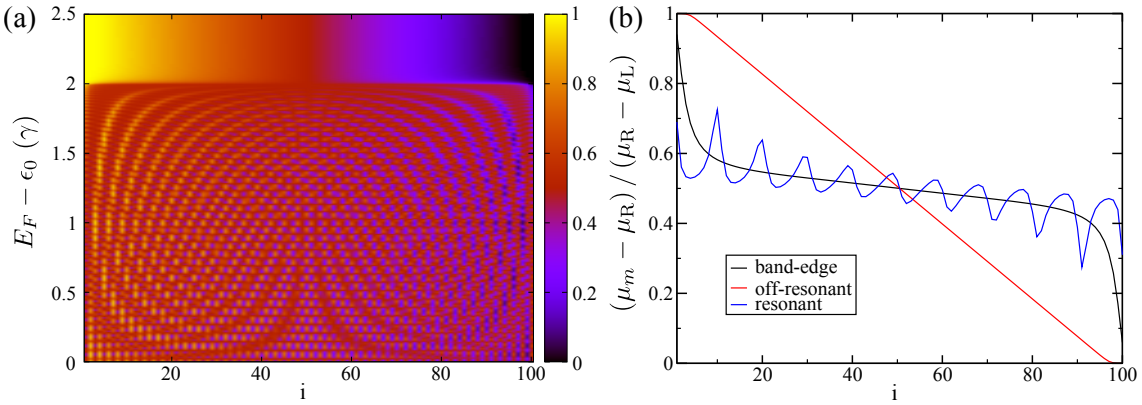

Figure 6.5: (a) Chemical potential of the Büttiker probes along the one-dimensional chain as a function of the Fermi energy. (b) Chemical potential as a function of the chain site for different Fermi energies of $E_F = \epsilon_0 + 2\gamma$ (black), $E_F = \epsilon_0 + 2.5\gamma$ (red) and $E_F = \epsilon_0 + 1.9\gamma$ (blue). We used a chain with $N = 100$ and a dephasing strength of $\eta = 10^{-2}\gamma$.

The thermopower can be derived using Eqs. 6.12 and 6.2. Here we find that the thermopower is constant in the Ohmic limit if decoherence is added.

$$\frac{S}{S_0} = \left.\frac{\partial_E r}{r}\right|_{E=E_F}. \tag{6.13}$$

If we compare the coherent τ_{coh} and incoherent τ_{inc} contribution to the transmission, we can define a phase coherence length. That is calculated as the intersection of the coherent transmission with the incoherent part, as shown in the inset of Fig. 6.4 (d). For a dephasing of $\eta = 10^{-2}\gamma$ we find a phase coherence length of $N^* \approx 6$. From this definition we obtain the coherence length as

$$L_{\text{coh}} = N^* \lambda \tag{6.14}$$

with the lattice constant λ. The calculated coherence length decreases exponentially with increasing dephasing η, as shown in Fig. 6.4 (d).

6.2.2 Chemical potential at the Büttiker probes

In Fig. 6.5 we show the chemical potential of the Büttiker probes as a function of the chain site. The color plot gives an overview on how μ_i depends on the Fermi energy E_F as well as on the chain position i. For all energy regimes the chemical potential μ_i is between μ_L and μ_R. The chemical potential oscillates as a function of the chain position, if the Fermi energy is within the band. These oscillations are interference effects between electrons from the leads as well as electrons which are scattered back from other Büttiker probes [84]. If we tune the Fermi energy to the band edge, we observe a step-like drop of the chemical potentials μ_i at the interfaces L and R of the chain. In the off-resonant case we find that the chemical potentials decrease linearly along the chain.

6.3 Dissipative transport in molecular junctions

In this section we discuss incoherent transport through single-molecule junctions. We describe the electronic structure of the molecules by using a TB Hamiltonian. This Hamiltonian includes nearest neighbor coupling. In the following we focus on the molecules which are shown in the inset of Fig. 6.6. We calculate the HOMO-LUMO gap of the molecules as a function of their length. The results from the TB scheme as well as from DFT are shown in Fig. 6.6. We find for both DFT and the TB model a finite ΔE for

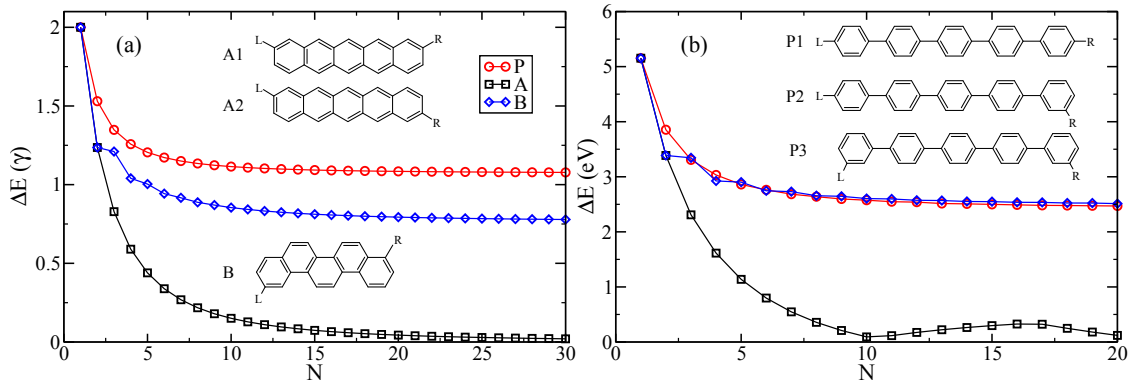

Figure 6.6: The HOMO-LUMO gap ΔE of the TB model (a) and from DFT calculations (b). The insets show schematic representations of the molecules discussed here: P1-3: oligophenylenes; A1,A2: polyacenes; B1,B2: polypenanthrenes. L and R denote the left and right electrode and indicate the geometry of the metal-molecule-metal structure.

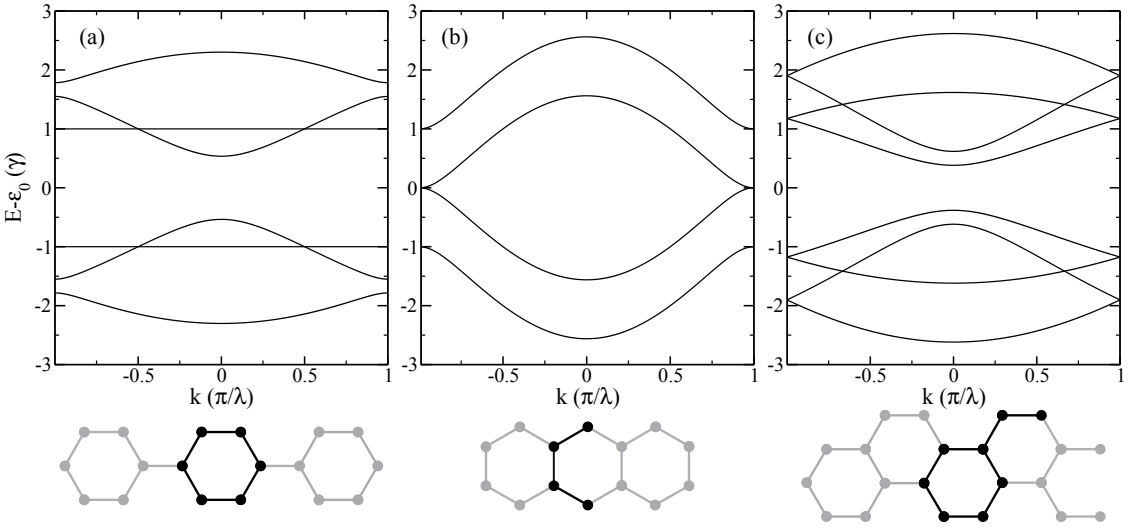

Figure 6.7: Band structure of Oligo-phenylenes (a), Poly-acenes (b) and Poly-penanthrenes (c). On the bottom we shows the primitive cell, gray atoms are for orientation.

oligophenylene (P) and polypenanthrene (B) molecules. This gap also remains in the limit of infinitely extended molecules. For the polyacenes (A) we observe that the gap vanishes as the molecular length increases.

The even-odd effect for short poly penanthrenes is observed in both DFT and TB. It is damped for longer molecules and the origin is due to the geometry of the molecule.

For the polyacenes (A) the DFT calculations predict an oscillating HOMO-LUMO gap. This can be reproduced within the TB model, assuming an inhomogeneous on-site energy. Here the on-site energy varies along the molecule, while it is symmetric around the middle of the molecule. This means that finite-size effects are the reason for the oscillations of the HOMO-LUMO gap.

6.3.1 Oligophenylenes

Following the calculations of Visontai et al. [85], we want to discuss oligophenylene molecules. These molecules consist of benzene rings coupled via the para position. We assume equal on-site energies ϵ_0 at each site. The nearest neighbor coupling inside the

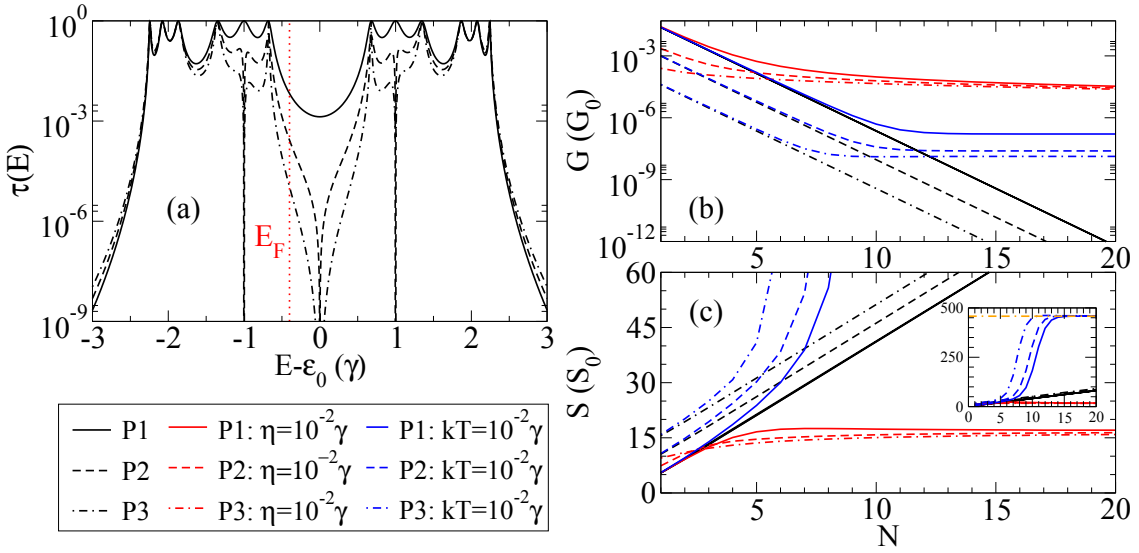

Figure 6.8: (a) Transmission, (b) Conductance and (c) Thermopower for Oligo-phenylenes with anchor positions P1-P3 as shown in inset of Fig. 6.6. (a): The length of molecules is $N = 3$ benzene rings. (b) and (c): The Fermi energy is $E_F = \epsilon_0 - 0.4\gamma$.

benzene rings is γ, the interaction between the different rings is $\gamma\prime = \gamma \cos\Phi$ with the ring tilt angle $\Phi = 40°$. For this tilt angle the band gap ΔE of long phenylene molecules shows a finite value, as shown in Fig. 6.6 (a). Form the DFT calculations we measure $\Phi \approx 34°$.

As shown in Fig. 6.6, we assume several coupling geometries for the electrodes. For the calculated conductance we used a Fermi energy inside the gap $E_F = \epsilon_0 - 0.4\gamma$, so we expect off-resonant transport. The band structure for a polymer of infinite length is shown in Fig. 6.7 (a). We find a gap of about $\Delta E = 1.06\gamma$.

In Fig. 6.8 (a) we see the transmission as a function of energy for a short phenylene molecule. Here we compare the different coupling positions. In the transmission we observe transmission antiresonances at $E - \epsilon_0 = 0$ for the P2 and P3 geometries. Those antiresonances are caused by quantum interference effects between two interfering transmission paths [70]. The antiresonances are absent for P1 [86].

As shown in Fig. 6.8 (b) and (c), the coherent conductance as a function of chain length shows an exponential decrease. Similarly, as observed previously for off-resonant transport, the Seebeck coefficient increases linearly. Adding incoherence weakens the exponential decrease and a transition to Ohmic behavior is observed in the conductance while the Seebeck coefficient saturates. At finite temperatures similar effects are observed for the conductance, where the exponential decay is absent. Here the conductance saturates at a value that is given by the band contribution to the integrals K_0 and K_1, within linear response. Similar trends are observed for the Seebeck coefficient, calculated at finite temperature. Here we find that it converges to $S/S_0 \approx 456$ for all contact geometries P1, P2 and P3, as shown in the inset of Fig. 6.8 (c).

6.3.2 Polyacenes

The polyacene molecules are built from benzene rings which are connected via two atoms (see inset of Fig. 6.6 (a)). The band structure of the infinite wire is shown in Fig. 6.7 (b). We find that the HOMO-LUMO gap vanishes for infinite length. In the following the Fermi energy is set to $E_F = \epsilon_0 - 3 \cdot 10^{-3}\gamma$.

In Fig. 6.9 (a) we show the coherent and incoherent charge transport. We get smooth

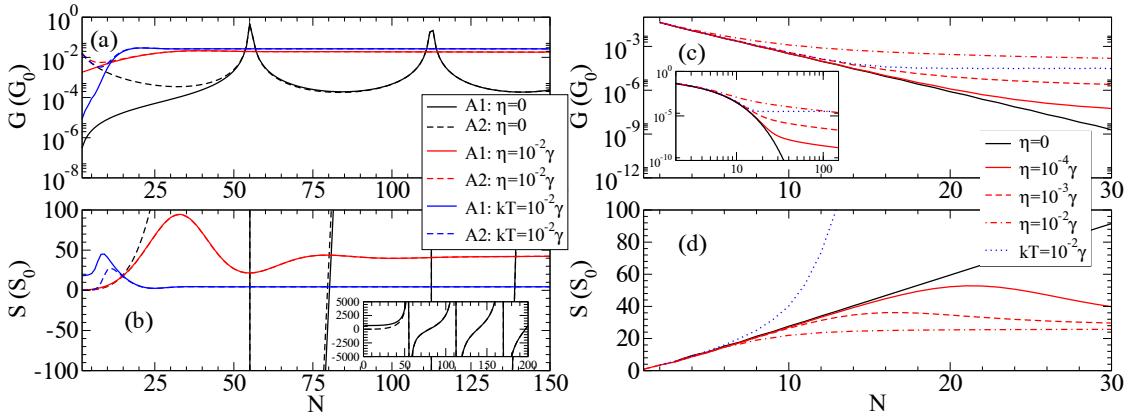

Figure 6.9: Transmission (a) and Seebeck coefficient (b) of Poly-acene for coupling position A1 and A2, Transmission (c) and Seebeck coefficient (d) of Poly-phenanthrene as a function of the chain lenght.

oscillations in the coherent conductance as a function of the length for both coupling positions. Only for short chains the coupling position matters and after the first period ($N > 25$) we do not see any difference between A1 and A2 couplings in the coherent conductance. For the incoherent transport we observe a transition to the Ohmic behavior for long chains.

By comparing the different coupling positions, we find that the conductance of the A1 molecule is much lower than for the A2 coupling position. The different coupling positions result in a similar conductance for molecules with more than 50 fragments.

6.3.3 Polyphenanthrenes

The polyphenanthrenes are similar to the polyacenes, but every second benzene is attached lopsided, as sketched in the inset of Fig. 6.6 (a). The infinite wire has a finite HOMO- LUMO gap, so we expect off-resonant transport for a Fermi energy of $E_F = \epsilon_0 - 0.3\gamma$. As expected, we find tunneling transport with an exponentially decreasing conductance and a linearly increasing thermopower as a function of the chain length (shown in Fig. 6.9 (c)). The incoherent transport is characterized by the transition to the Ohmic length dependence of the conductance and a saturating thermopower.

6.4 Conclusions

We analyzed the crossover between coherent and incoherent transport. To model dephasing effects, we used the Büttiker probes. For a linear chain we discussed the coherence length as a function of the dephasing strength. We analyzed the voltage measured at the Büttiker probes.

For molecular junctions constructed from oligophenylenes, polyacenes and polyphenanthrenes, we analyzed the incoherent transport as well as effects of finite temperature within the linear response regime.

Part II

Heat transport and thermoelectricity in molecular junctions

7 First principles approach to heat transport through molecular systems

In this chapter we want to present our approach to describe the phonon heat transport in nanoscale systems. Especially for problems in molecular electronics a first principles method is favored, since it minimizes the number of free parameters. Therefore we apply DFT to calculate electronic as well as mechanical properties, in particular the force constants, on the atomic scale.

We use TURBOMOLE [87] to calculate the second derivative of the total energy with respect to the nuclear positions, as it is implemented in the module aoforce [88, 89]. Originally those methods were developed to deal with finite systems such as molecules. In contrast we need to describe heat transport in an infinite system - that system consists of a molecular part in the center, coupled to two semi-infinite metal leads. Comparable challenges have to be overcome, when describing the electronic properties in molecular electronics [90–96]. Similar schemes have been applied to the phonon transport as well [25–27].

Here we give a sketch of the scheme used to describe phonon transport. First we calculate the vibrational properties of the ECC as shown in Fig. 7.1 (a). That ECC consists of a molecule attached to metal fragments. Therefore we can extract from the ECC geometry the force constants of the molecule and the force constants that couples the molecule and the metal. Secondly, we determine the properties of the leads. Here we extract the bulk parameters from a calculation of a big but finite metal cluster, pictured in Fig. 7.1 (b). Finally the components are coupled, assuming that the two semi-infinite leads do not interact directly. The basic formalism is described in Sec. 2.2 for a slightly more abstract case.

In Sec. 7.1 we describe the phonon structure of the leads. Next we investigate the lead molecule coupling in Sec. 7.2. Finally, in Sec. 7.3, we present our analysis of the heat transport through mono-atomic gold wires.

7.1 Phonon density of states of the bulk electrode

To model the properties of phonons in the semi-infinite lead, we calculate the force constant matrix of a spherical geometry, also referred to as ball in the following. Several examples thereof are shown in the inset of Fig. 7.2. We refer to each ball by the number of atoms it consists of. The atoms in the balls are located at the fcc lattice positions

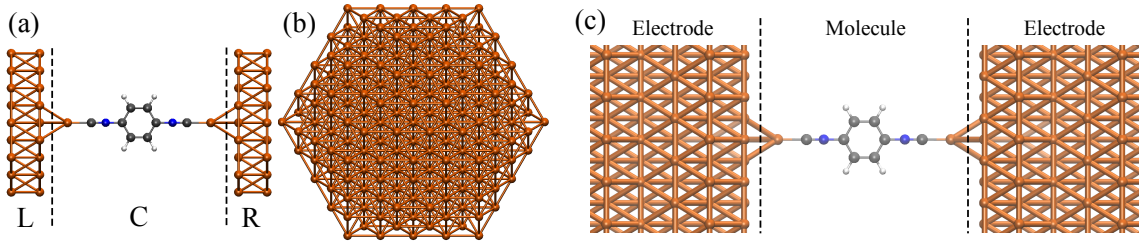

Figure 7.1: (a) Example of an ECC geometry, (b) gold ball and (c) system that models a molecular junction.

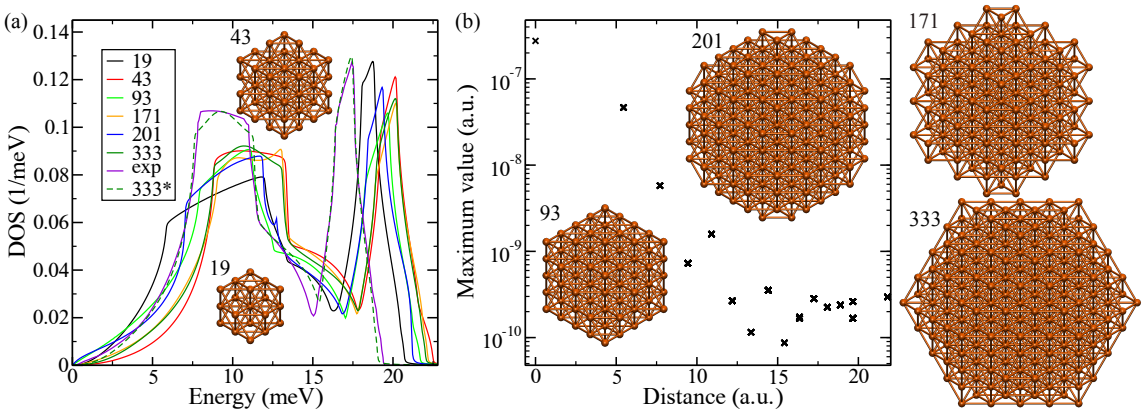

Figure 7.2: (a) Phonon density of states calculated with force constants obtained from different balls. The dashed line is scaled by 0.864, while preserving the norm. We show measured values from Ref. [97], labeled as exp. (b) Maximum absolute value of the force constant matrix as a function of the distance to the central atom, extracted from the ball with 333 gold atoms. The insets show the geometries of the gold balls which consist of 19, 43, 93, 171, 201 and 333 gold atoms as indicated next to each ball.

with a lattice constant of 4.08 Å. We do not relax those geometries, because we rather model the fcc structure of the bulk. The balls are constructed such that the O_h symmetry is conserved. Additionally, only balls can be used where the electron energy levels are filled up to the Fermi energy E_F and above E_F all energy levels are empty. Especially for electron states degenerate due to symmetry that is a constraint. To determine the electronic structure we used the PBE functional [31, 32] with the def-SV(P) [33] basis set. The electron energy is converged to a precision better than 10^{-7} a.u..

If we increase the size of the balls the central atom will feel a similar environment as in the bulk crystal. For this assumption to hold it is necessary that the force constant between atoms decreases fast as a function of their distance. To test that condition, we plot in Fig. 7.2 (b) the maximum value of the force constant matrix, connecting the central atom with each of the other atoms of the 333 ball. Here we find that the maximum force constant decreases exponentially up to a distance of about 14 a.u.. Then it saturates for bigger distances at a value below $3 \cdot 10^{-10}$ a.u.. In the 333 ball the maximum distance of an atom from the central atom is about 21.8 a.u..

We extract the force constant matrix elements, coupling the central atom to each of the atoms of the ball. From these parameters we construct the bulk Hamiltonian by imposing the translation symmetry of the lattice. The density of states (DOS), calculated from those parameters, is shown in Fig. 7.2 for several balls. It is obtained by

$$\rho(\omega) = -\frac{2\omega}{\pi} \sum_i \mathrm{Im}\left\{D^r_{ii}(\omega)\right\} \qquad \text{for } \omega > 0. \tag{7.1}$$

To calculate the Greens function, we use a finite broadening of the energy of $\eta = 10^{-6}$ a.u.. Also we use a Fourier transformation to calculate the Greens function in the reciprocal space for each k point separately. The Fourier transformation is performed using 512 k-points in total. To calculate the DOS, we use the fcc primitive cell with 1 atom, here. In the following work, to perform our transport calculations, we will use a unit cell that includes 3 atoms. Here one lattice vector points in the direction of transport and the other two span the space orthogonal to the transport direction. In Fig. 7.2 we compare our results to a measured phonon DOS, that is obtained by inelastic scattering of neutrons [97]. After scaling the calculated energies, we find good agreement with the measured values.

7.2 Coupling to the electrodes

Usually the electrodes are attached to the left and right side of the ECC structure, as shown in Fig. 7.1. Therefore the coupling K_{CX} between C and the lead $X \in \{\mathrm{L,R}\}$ is extracted from the ECC. In the next step the surface Greens function of the leads is calculated using the bulk parameters, extracted from metal balls as described in Sec. 7.1. We use a decimation scheme to calculate the surface Greens function of the lead [98]. The retarded surface Greens function d^r_X is then used in Eq. (2.39) to determine the embedding self energy Π^r_X for lead $X \in \{R, L\}$.

To investigate the influence of cutting the ECC into different fragments L, C and R, we look at the properties of a gold rod. The geometry of the gold rod is shown in the inset of Fig. 7.3 (b). The rod is cut out of a fcc lattice and the transport direction (i.e. the orientation of the rod) is along the $\langle 111 \rangle$ direction. Different possibilities for dividing the rod are indicated in the inset of Fig. 7.3 (b). The positions of the atoms in the rod are not optimized. As shown in Fig. 7.3 (a), the phonon transmission reveals a clear dependence on the position of the cut. As we increase the size of the C part, the transmission tends to decrease. Also the phonon heat conductance, shown in Fig. 7.3 (b), becomes smaller as

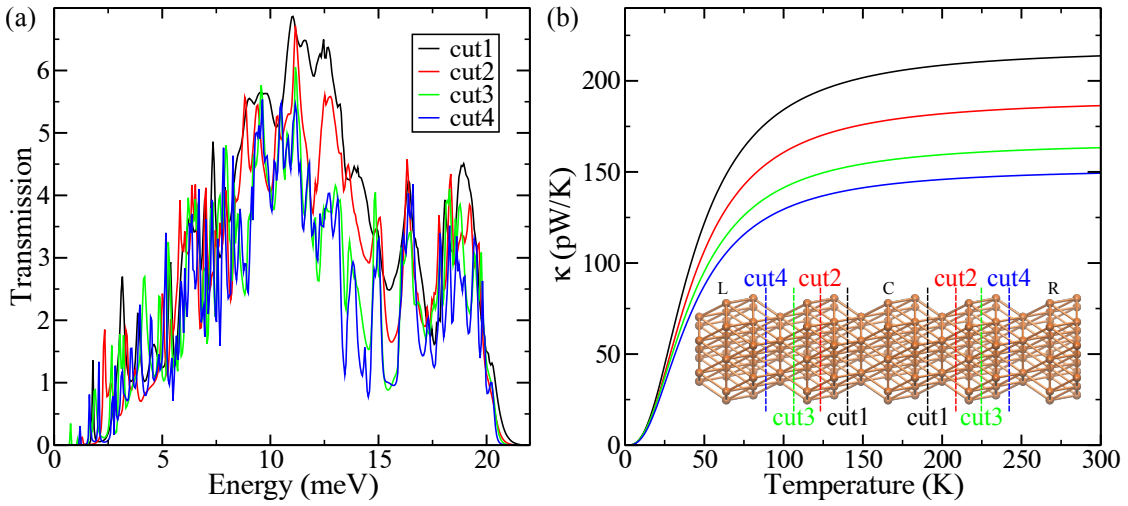

Figure 7.3: (a, b) Phonon transmission and phonon heat conductance of a gold rod. The geometry of the rod is shown in the inset of (b), where the different cuts are indicated as well.

we extend the C part. That is not unexpected since we couple a semi-infinite bulk system to the left and right - i.e. the C part represents a constriction.

Therefore we investigated, whether the observed differences in the heat conductance also occur, if we couple the C part to a semi-infinite rod instead of a semi-infinite bulk electrode. Similarly as we extract the bulk parameters from the balls in Sec. 7.1, we extract the parameters from the rod. Here the semi-infinite rod is described by a one-dimensional lattice as sketched in the inset of the Fig. 7.4. Therefore we use a crystal basis including 31 atoms. The rod as a whole consists of 5 lattice points.

To calculate the phonon transmission it was necessary to extend the transport program to allow for a lattice basis, including more than one atom. Also modifications were necessary to use the program with leads that are described by a one-dimensional lattice.

The rod is cut at the positions indicated in the inset of Fig. 7.4. Those positions are between lattice points. We find that the transmissions of cut1 and cut2, as shown in Fig. 7.4, exhibit similar behavior. Since the rod includes only 5 lattice points, the coupling between atoms is influenced by the finite length of the rod and may vary along the rod. Therefore changes in the transmission due to different cuts are expected. Nevertheless we find a heat conductance that depends weakly on the position of the cut. For higher temperature the difference is about 5 pW/K. In contrast to the bulk electrode construction, the heat conductance increases slightly if we extend the C part.

Clearly, the vibrational spectrum of the molecular junction is not affected, if we translate each atom by the same distance $\Delta\vec{R}$. To ensure this the force constant matrix K_{ls} has to fulfill the condition

$$\sum_s K_{ls} = 0. \tag{7.2}$$

In the following we will investigate to what extent the transmission changes, if this condition is violated. Therefore we extract a force constant matrix that fulfills Eq. (7.2) by construction.

Up to now we calculate the surface Greens function from parameters extracted from the center of the rod. Then the surface Greens function is coupled to the lattice point 1 and -1 for cut1. At least the on-site force constants of lattice point 0 differ from those of ± 1, therefore the condition of Eq. (7.2) is violated. To avoid that, we calculate the

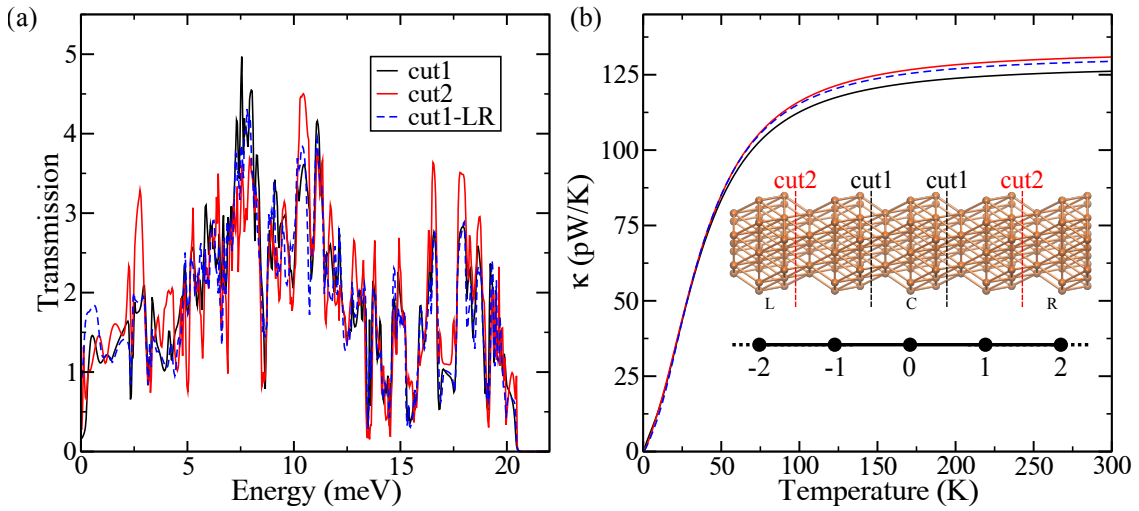

Figure 7.4: (a, b) Transmission and heat conductance of a gold rod. The geometry of the rod is shown as an inset of (b) where the different cuts are indicated as well.

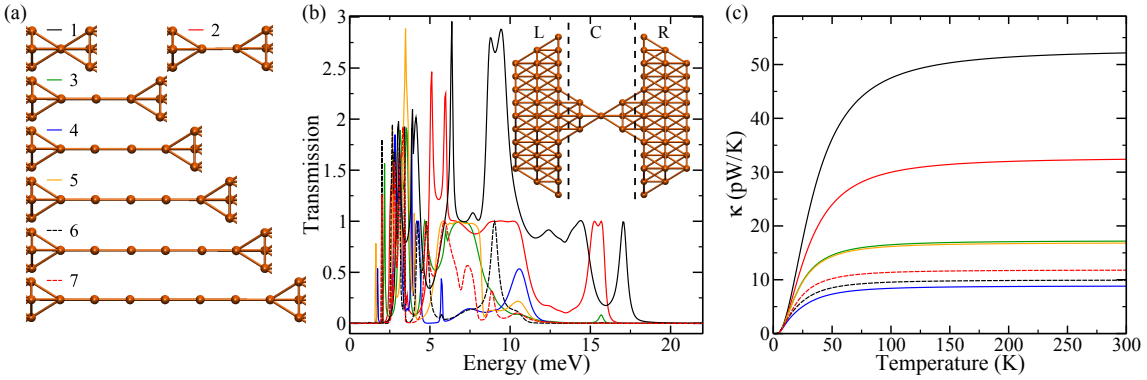

Figure 7.5: (a) Geometry of the C part of the gold chains investigated. (b, c) Transmission and heat conductance, respectively. The inset shows the full ECC geometry, it is indicated how we divide it in to L,C and R part.

surface Greens function from force constants extracted from the L and R part of the ECC. By construction these force constants then preserve Eq. (7.2). The drawback is that the extracted force constants are influenced by the ends of the rod in an asymmetric way, i.e. one end of the rod is closer compared to the other. The calculated transmission is shown in Fig. 7.4 (a), labeled as cut1-LR. The ECC is divided similarly for cut1 and cut1-LR. The resulting phonon transmission for cut1 and cut1-LR are found to be in reasonable agreement. Also the phonon heat conductance of cut1 is similar to cut1-LR, even if cut1 shows a slightly smaller value.

7.3 Heat transport through atomic gold wires

In this section we discuss the properties of atomic wires constructed from gold chains. What is attractive about that system is that it consists of gold atoms only and therefore it represents a rather simple system. An example for the ECCs used in this study is shown in Fig. 7.5 (b). In the picture we show the shortest gold chain that consists of only one atom. We extend that chain up to 7 gold atoms. We refer to each geometry by the number of atoms in the chain. The atoms in the chain possess a linear configuration. That geometry is most likely realized in experiments, shortly before the rupture of the atomic junction

Chain length	1	2	3	4	5	6	7
$E_{\max}$(meV)	16.9072	15.6787	15.3773	15.8459	15.5382	15.5405	15.3777
$E^M_{\max}$(meV)	14.1421	11.8322	11.3534	11.2274	11.1924	11.1834	11.1811

Table 7.1: Maximum vibrational energy of the geometry of the C part, $E_{\max}$, as well as for a model system $E^M_{\max}$, described in Sec. 7.4.2, using $k_C = 20$ meV^2 and $k_L = 100$ meV^2.

takes place.

The phonon transmission for the atomic wires is plotted in Fig. 7.5 (b). We find that it is always smaller than 3. For energies below 1 meV and above 20 meV the transmission is approximately zero. Additionally, the eigenvalues of the transmission (i.e. transmission eigenchannels) are always smaller than one. Geometry 1 shows tree eigenchannels at an energy of about 10 meV, which exhibit a transmission of almost 1. As we increase the length of the chains, we find that the transmission cutoff at high energies tends to become smaller. While it is about 19 meV for chain 1, it becomes about 17 meV for chain 2 and 3. It saturates for longer chains at about 12 meV. That cutoff is not due to the different vibrational spectra of the chains. As shown in Tab. 7.1, the vibrational mode with the highest energy depends weakly on the chain length. Except for the chain 1 the maximum vibrational energy is almost constant at a value of about 15.5 meV.

In Sec. 7.4 we derive a model for heat transport using a linear chain. That model only allows the atoms of the chain to vibrate in one direction along the chain (i.e. longitudinal modes). The transmission obtained from that model shows a decreasing energy cutoff for increasing chain length. Hence the model predicts that the heat conductance due to phonons decreases with increasing chain length but saturates for long chains, as shown in Fig. 7.8 (b). This saturation is not observed for the full calculation in Fig. 7.5 (b), but qualitatively the heat conductance tends to become smaller for longer chains. For the full calculation we observe an even-odd effect for the phonon heat conductance. Wires with an even number of atoms show a smaller heat conductance.

7.4 Model of heat transport in molecular junctions

In this section we investigate a model system that describes heat transport along a one-dimensional chain. While a similar model is frequently used to describe basic mechanisms in electric transport, it is less frequently used for modeling heat transport due to vibrations. As indicated in Fig. 7.6 we will assume different force constants in the central part k_C compared to the leads on the left and right sides k_L. We consider only nearest neighbor interaction.

We will first describe the properties of the semi-infinite lead in Subsec. 7.4.1. Next, we will model different molecular junctions in Subsec. 7.4.2.

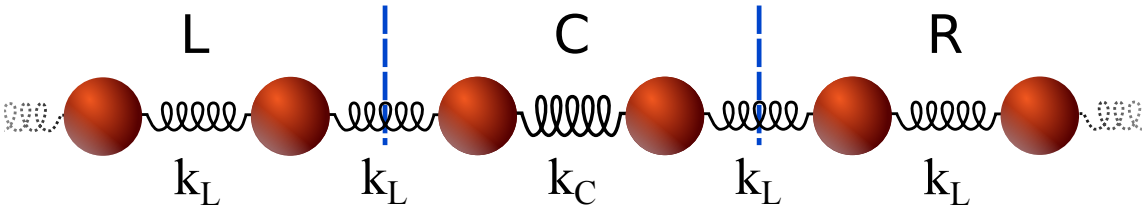

Figure 7.6: Linear chain with different force constants in part C compared to the leads in L and R. Here are 2 atoms in C, connected by a spring constant k_C. The attached leads show a different spring constant k_L.

7.4.1 Semi-infinite and infinite one dimensional chain

First we calculate the surface Greens function for a semi-infinite linear chain, assuming nearest neighbor coupling. To do so we consider the coupling to the last site of the chain as a perturbation. The force constant matrix is

$$K = K_0 + V = \begin{pmatrix} 2k & 0 & 0 & 0 \\ 0 & 2k & -k & 0 \\ 0 & -k & 2k & \ddots \\ 0 & 0 & \ddots & \ddots \end{pmatrix} + \begin{pmatrix} 0 & -k & 0 & 0 \\ -k & 0 & 0 & 0 \\ 0 & 0 & 0 & \ddots \\ 0 & 0 & \ddots & \ddots \end{pmatrix}. \tag{7.3}$$

The Greens function of the unperturbed part is

$$d = \left[\omega^2 - K_0\right]^{-1} = \begin{pmatrix} d_{00} & 0 \\ 0 & D \end{pmatrix}. \tag{7.4}$$

That Greens function describes the semi-infinite chain by D and the additional uncoupled site by d_{00}. For the full Greens function, including the interaction to the last site given by V, we can use the Dyson equation:

$$D = \left[\omega^2 - K\right]^{-1} = d + dVD. \tag{7.5}$$

Because we like to attach additional sites at the end of the chain we are interested in the surface Greens function D_{00} only.

$$D_{00} = d_{00} + d_{00}V_{01}D_{10} \tag{7.6}$$
$$(\omega^2 - 2k)D_{00} = 1 - kD_{10} \tag{7.7}$$
$$D_{10} = d_{11}V_{10}D_{00} = -kD_{00}^2 \tag{7.8}$$
$$\left(\omega^2 - 2k\right) D_{00} = 1 + k^2 D_{00}^2 \tag{7.9}$$
$$2k^2 D_{00} = \omega^2 - 2k \pm \omega\sqrt{\omega^2 - 4k} \tag{7.10}$$

The sign has to be chosen such that the density of states, given by Eq. (7.1), will be positive, and such that $D_{00}(\omega) \overset{\omega\to\infty}{\longrightarrow} 0$. The surface Greens function is plotted in Fig. 7.7 (a). Here we see that the imaginary part of the surface Greens function is zero for $\omega > 2\sqrt{k}$. The real part increases quadratically for $\omega < 2\sqrt{k}$, while for bigger energies it decreases.

Now we can couple two semi-infinite chains and determine the density of states of the resulting infinite one-dimensional chain. For this we need the Greens function of a site in the center. Additionally, we allow a different on-site element on the central site, to test the effect of violating Eq. (7.2)

$$H = \begin{pmatrix} \ddots & \ddots & 0 & 0 & 0 \\ \ddots & 2k & -k & 0 & 0 \\ 0 & -k & 2o & -k & 0 \\ 0 & 0 & -k & 2k & \ddots \\ 0 & 0 & 0 & \ddots & \ddots \end{pmatrix}. \tag{7.11}$$

That results in the Greens function for the central site

$$D_{CC}^r = \frac{2(k-o) - i\omega\sqrt{4k - \omega^2}}{4(k-o)^2 + \omega^2(4k - \omega^2)}. \tag{7.12}$$

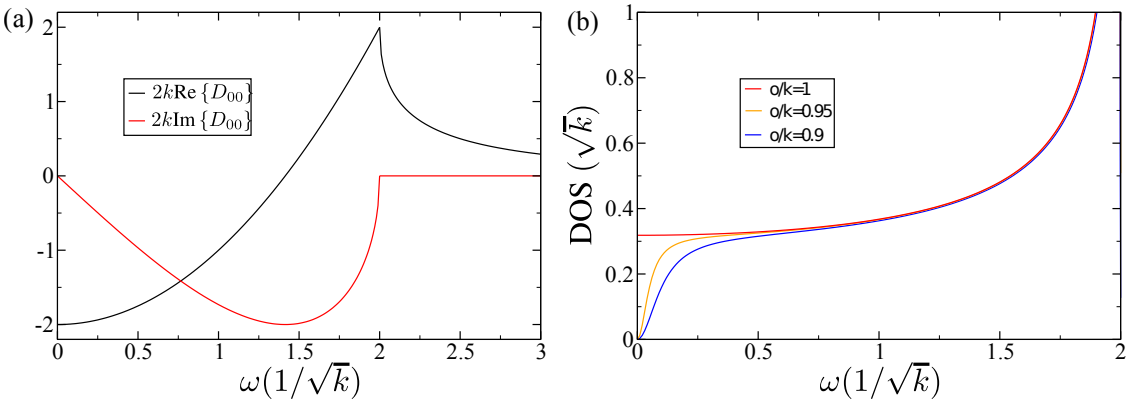

Figure 7.7: (a) Real and imaginary part of the surface Greens function of a semi-infinite chain. (b) Density of states of an infinite chain with one element in the center that shows a different onsite element.

From that we can calculate the density of states as

$$\rho = -\frac{2\omega}{\pi}\mathrm{Im}\left\{D^r_{CC}\right\} = \frac{2\omega}{\pi}\frac{\omega^2\sqrt{4k-\omega^2}}{4\left(k-o\right)^2+\omega^2\left(4k-\omega^2\right)}. \tag{7.13}$$

This expression is plotted in Fig. 7.7 (b). We find that violating Eq. (7.2) suppresses the vibrational density of states at low energy.

7.4.2 Model for a gold chain

In this subsection we describe the phonon heat transport of gold chains coupled to electrodes on both sides. As electrodes we use semi-infinite, one-dimensional chains with nearest neighbor interaction k_L. The force constant in the center is assumed to be k_C. That kind of chain is sketched in Fig. 7.6. Now it is possible to consider gold chains with different numbers of sites in the center. We will discuss geometries that consist of 1 to 4 sites in the C part. Their force constant matrices of the C part are:

$$K_1 = \left(\ 2k_L\ \right), \quad K_2 = \begin{pmatrix} k_C+k_L & -k_C \\ -k_C & k_C+k_L \end{pmatrix}, \tag{7.14}$$

$$K_3 = \begin{pmatrix} k_C+k_L & -k_C & 0 \\ -k_C & 2k_C & -k_C \\ 0 & -k_C & k_C+k_L \end{pmatrix}, \tag{7.15}$$

$$K_4 = \begin{pmatrix} k_C+k_L & -k_C & 0 & 0 \\ -k_C & 2k_C & -k_C & 0 \\ 0 & -k_C & 2k_C & -k_C \\ 0 & 0 & -k_C & k_C+k_L \end{pmatrix}. \tag{7.16}$$

For the system described by K_i we calculate the corresponding phonon transmission $T_i(\omega)$ with $i = 1, 2, 3, 4$, as plotted in Fig. 7.8 (a). Here the transmission shows a constant value for very small energies. That implies that for small temperatures, the heat conductance is proportional to the temperature. If the number of sites in C increases, the cutoff energy of the transmission decreases. In Fig. 7.8 (b) we plot the heat conductance of the model system. We find that the heat conductance converges, as we extend the C part. Visually there is no difference between the heat conductance κ_3 and κ_4 in Fig. 7.8 (b). At high

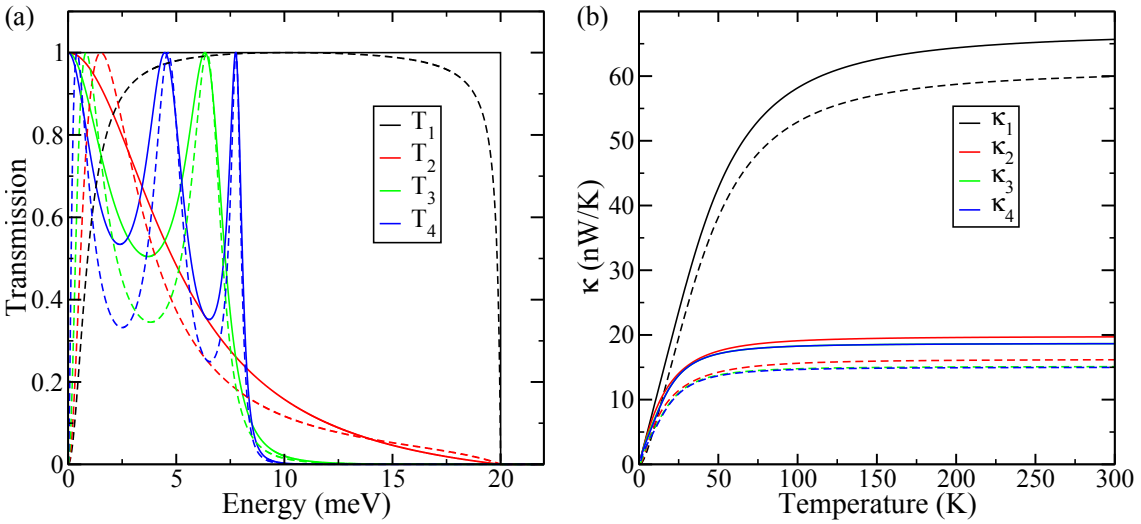

Figure 7.8: In (a) the solid lines show the transmission for $k_{\mathrm{L}} = 100\,\mathrm{meV}^2$ and $k_{\mathrm{C}} = 20\,\mathrm{meV}^2$. The dashed lines show the transmission for the case where Eq. (7.2) is violated, where we use $k_{\mathrm{L}}^{\mathrm{ECC}} = 110\,\mathrm{meV}^2$. (b) Heat conductance as a function of the temperature (solid) and with violation of Eq. (7.2) (dashed).

temperatures we find for chains, longer than three sites in the C part, a heat conductance of about $19\,\mathrm{nW/K}$.

Now we consider a violation of the condition, formulated in Eq. (7.2). To model that, we used a different force constant in the ECC as in the leads. We use $k_L \leftarrow k_L^{ECC}$ in K_i. In Fig. 7.8 (a) we find that this leads to a suppressed transmission at low energies. In Fig. 7.8 (b) we show that the heat conductance of the model system is suppressed for the case, where the condition Eq. (7.2) is violated. The heat conductance converges to a value of about $15\,\mathrm{nW/K}$.

7.5 Conclusions

We described our scheme to calculate the phononic heat transport through molecular junctions. For this purpose we used the Greens function formalism, combined with the phononic structure calculated using density functional theory (as implemented in TURBOMOLE). The coupling between the molecule and the leads was investigated. We compared the results, obtained for differently coupling positions and different structured leads. We also calculated the phonon heat transport through gold atomic contacts. For those atomic contacts we compared the results to a tight-binding model.

8 Heat transport through π-stacked molecules

In this chapter we focus on the heat transport through single-molecule junctions. We investigate the heat transport through paracyclophane molecules, caused by phonons and electrons, as well as thermoelectric effects. The electric conductance of molecular junctions with paracyclophane molecules was discussed in Chap. 4. Here we use the same ECC geometries which are described already in Chap. 4.

The electronic π system of paracyclophane molecules results in a relatively high electric conductance, as found in Chap. 4. The main reason is the delocalized nature of the π electron system. While the electronic heat conductance is mostly determined by the Wiedemann-Franz law, the phonon contribution may be expected to be low for paracyclophane molecules. Here the mechanical link due to the absence of an anchor group should be weak. At least for π-π stacked systems the heat conducting phonons which couple the stacked parts, are expected to have low energies.

This chapter begins with a discussion of the thermopower of the parayclophane molecular junctions in Sec. 8.1. Then the heat conductance is analyzed in Sec. 8.2. Finally we present the thermoelectric figure of merit of the single-molecule junctions in Sec. 8.3.

8.1 Thermopower

The thermopower, calculated for a temperature of 10 K, is shown in Fig. 8.1. Here we find a linear increase with molecular length. The results of a linear fit $S = A \cdot N + B$ are summarized in Tab. 8.1. We observe that the thermopower increases linearly with temperature up to about 300 K. We find that for the coupling at one single adatom on the gold surface the thermopower is enhanced. That might be due to a weaker coupling to the electrodes and therefore the resonances in the transmission are sharply. Thus while the conductance decreases, we find an increase in the Seebeck coefficient.

	I	II	III
A	$0.21\ \frac{\mu\mathrm{V}}{\mathrm{K}}$	$0.09\ \frac{\mu\mathrm{V}}{\mathrm{K}}$	$0.11\ \frac{\mu\mathrm{V}}{\mathrm{K}}$
B	$-0.22\ \frac{\mu\mathrm{V}}{\mathrm{K}}$	$-0.15\ \frac{\mu\mathrm{V}}{\mathrm{K}}$	$-0.20\ \frac{\mu\mathrm{V}}{\mathrm{K}}$

Table 8.1: A and B obtained by a linear fit to the thermopower, shown in Fig. 8.1.

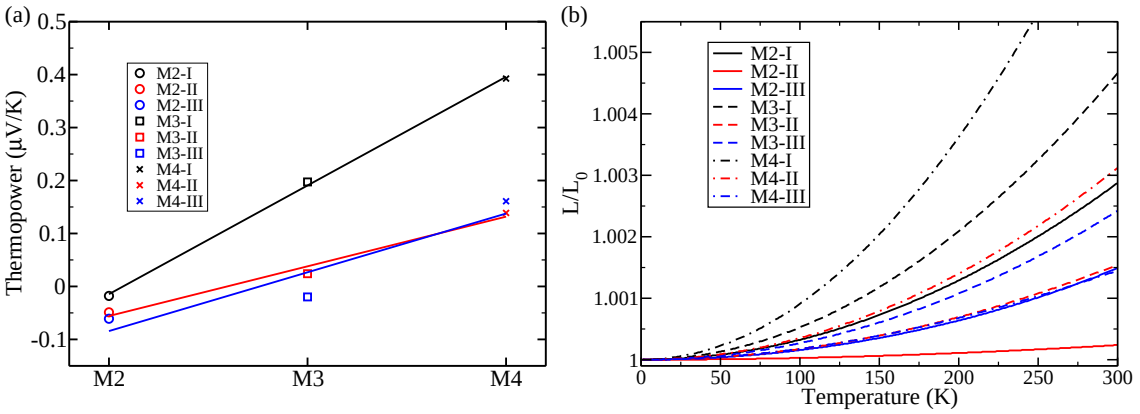

Figure 8.1: (a) Thermopower calculated using the electron transmission shown in Fig. 4.3 (a). The straight lines are fits to the numerical results (b). Deviation from the Wiedemann-Franz law.

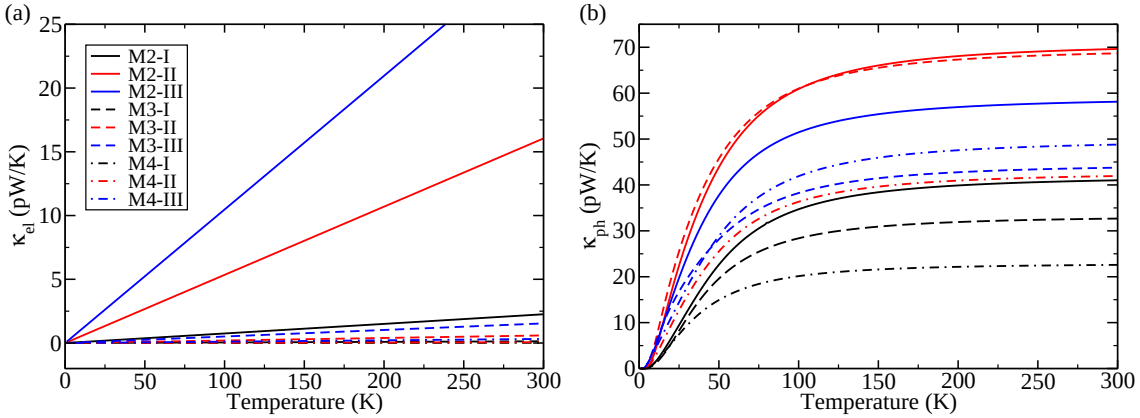

Figure 8.2: Heat conductance due to electrons (a) and phonons (b).

The thermopower, calculated for the M2 molecule, is negative for all electrode geometries. Therefore we observe a sign change of the thermopower depending on molecular length. It can be speculated that it is challenging to measure that sign change in experiments, because the value of the thermopower is rather small.

8.2 Heat conductance

In this section we analyze the heat transport properties of the molecular junctions. First we focus on the electronic heat conductance, which is compared to the Wiedemann-Franz law. Then we focus also on the phonon heat conductance.

Contribution due to electrons

The heat conductance due to the electronic degrees of freedom can be computed from the energy dependent electron transmission, via Eq. (2.48). In the case of an energy-independent transmission, it is possible to derive the Wiedemann-Franz law [99]. The Wiedemann-Franz law connects the electron heat conductance κ_{el} with the electronic conductance G [99]:

$$L = \frac{\kappa_{\mathrm{el}}}{GT}. \tag{8.1}$$

If the Wiedemann-Franz law is fulfilled, the ratio of Eq. (8.1) is given by $L = L_0 = \frac{\pi^2}{3}\left(\frac{k_{\mathrm{B}}}{e}\right)^2$. The constant L_0 is called Lorenz number.

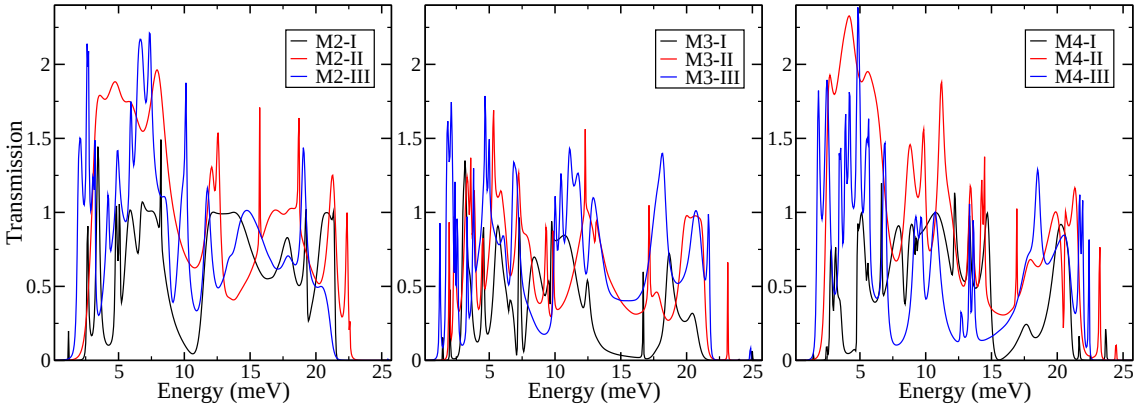

Figure 8.3: Phonon transmission as a function of energy.

We plot L/L_0 in Fig. 8.1 (b). We find that the paracyclophane molecular junctions do not violate the Wiedemann-Franz law drastically. The reason for this is that the resonances in the electron transmission is situated at about 1.5 eV above and below the Fermi energy. As a result the transmission depends weakly on energy, at least close to the Fermi energy.

The heat conductance due to the electron system is shown in Fig. 8.2 (a). Here we find that it depends linearly on the temperature up to 300 K. The heat conductance shows a rapid decrease with the length of the molecule. We find an exponential decrease of the heat conductance similar to that for the electric conductance.

Contribution due to phonons

In Fig. 8.3 we show the phonon transmission, calculated as described in Chap. 7 using Eq. (2.43). Because the gold density of states becomes very small for energies bigger than about 25 meV, the transmission through the molecular junctions is suppressed for higher energies. Also for low energies we find a suppression of the phonon transmission. That is related to the suppressed gold density of states for low energies, as well. The energy window that is important for heat conductance due to phonons reaches from 2 meV to 25 meV. The transmission as a function of energy is found to be smaller than 3 for all paracyclophanes. As we diagonalize the transmission operator, we find that the transmission eigenchannels have values between 0 and 1.

Using Eq. (2.50), we calculate the phonon heat conductance. It is shown in Fig. 8.2 (b). We find that the heat conductance depends rather on the interface geometry of the junction than on the molecular length. We find $\kappa(\mathrm{I}) < \kappa(\mathrm{III}) < \kappa(\mathrm{II})$ for all ECCs but M3-II.

For temperatures bigger than 150 K the phonon heat conductance saturates. At that temperature the heat current can be approximated by a semi infinite integral of the phonon transmission. The phonon heat conductance saturates between 20 pW/K and 65 pW/K. Therefore the phonon heat conductance is bigger compared to the heat conductance due to electrons for median temperatures, at least by about a factor of 2. Eventually the electron heat conductance is dominant for very high temperatures.

8.3 Figure of merit

A solid state thermoelectric power converter could be used to convert waste heat to electricity at places, where moving parts that need to be maintained are unwanted. The open task is to find materials that can be used in such a device and are best suited to give a high efficiency. It is assumed that nanostructures can be used to tune the efficiency. To characterize the material properties to serve in a thermoelectric device, it is common to use the figure of merit ZT [29].

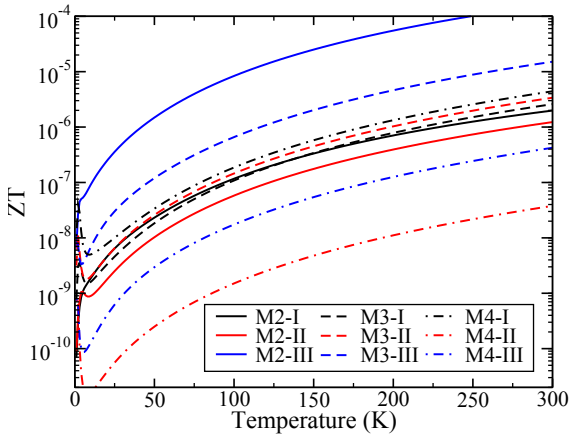

Figure 8.4: thermoelectric figure of merit as a function of energy.

In this section estimate the figure of merit ZT for a single-molecule junction. For this purpose we use the thermoelectric properties calculated in this Chapter. The figure of merit is defined as

$$ZT = \frac{GS^2T}{\kappa_{\text{el}} + \kappa_{\text{ph}}}, \tag{8.2}$$

where the heat conductance $\kappa = \kappa_{\text{el}} + \kappa_{\text{ph}}$ is dominated by the phonon contribution, for temperatures up to 300 K. The electric conductance is rather high for paracyclophanes as compared to other molecular contacts. In contrast the Seebeck coefficient S is rather small for the paracyclophane molecules discussed here. In Fig. 8.4 we plot the figure of merit ZT for the parayclophane molecular junctions. We find that those molecular junctions show rather poor values for ZT. Using chemical gating it is possible to tune the Seebeck coefficient by a factor of 10, while the electric conductance and the heat conductance show only minor changes [100].

8.4 Conclusions

In this chapter we analyzed the thermoelectric properties of parayclophane molecular junctions. We focused on paracyclophanes with different lengths. We found that the thermopower increases linearly as a function of the molecular length. Analyzing the heat conductance reveals that the phonon contributions are at least 10 then the electronic ones. We found that the figure of merit for molecular junctions with paracyclophane molecules is below 10^{-4} for temperatures up to 300 K.

9 Thermoelectricity of benzene derivatives

In this chapter we focus on the thermoelectric properties of gold-benzene-gold molecular junctions. The used anchor groups are interesting, because the dominant transmission channel changes from LUMO (electron like charge carriers) for nitrile anchors to HOMO (hole like charge carriers) for amine anchors. The molecule equipped with nitrile anchors is called 1,4-benzenediisonitrile (BDNC) and the molecule with the amine anchor is called 1,4-benzenediamine (BDA) in the following.

In this chapter we first discuss how we describe the geometry of the molecular junctions in Sec. 9.1. Then we will give a brief description of the electric properties in Sec. 9.2. Our analysis of the heat transport is presented in Sec. 9.3.

9.1 Modeling molecular junctions

In experiments the atomistic details of the Au-molecule-Au junction geometry are not accessible. Therefore we assume in this section that the molecules bind to an adatom on a clean gold surface that is perpendicular to the gold $\langle 111 \rangle$ lattice direction. This is the direction of the electric transport. To construct the ECC geometry we start from a molecule attached to one electrode. That geometry is optimized and the second electrode is attached symmetrically. This first geometry is referenced as 0.00 Å. The position of some gold atoms of the electrode are fixed during the optimization as indicated in Fig. 9.1. To model the stretching process the fixed atoms of the electrodes are displaced stepwise by about $d = 0.1058$ Å. Subsequently the ECC geometry is optimized after each step. In Fig. 9.1 we show some ECC structures of the BDA and BDNC single-molecule junctions. The gold electrodes on the left and right side consist of two layers cut out of a fcc lattice, including 37 gold atoms on each side. The position of all gold atoms but the adatom are fixed if we search for the ground state geometry. To optimize the geometries we use DFT as implemented in TURBOMOLE with the PBE functional [31, 32], employing the def-SV(P) basis set [33]. The total energy is converged to a precision better than 10^{-7} a.u., the structure optimizations are carried out till the maximum norm or the gradients were fallen below 10^{-5} a.u..

For BDNC we find a quite simple picture. Since the nitrile anchor apparently binds perpendicular to the gold surface, we find an almost linear geometry. Here we increase the electrode displacement to a value of 1.80 Å and find that the molecule tends to bind

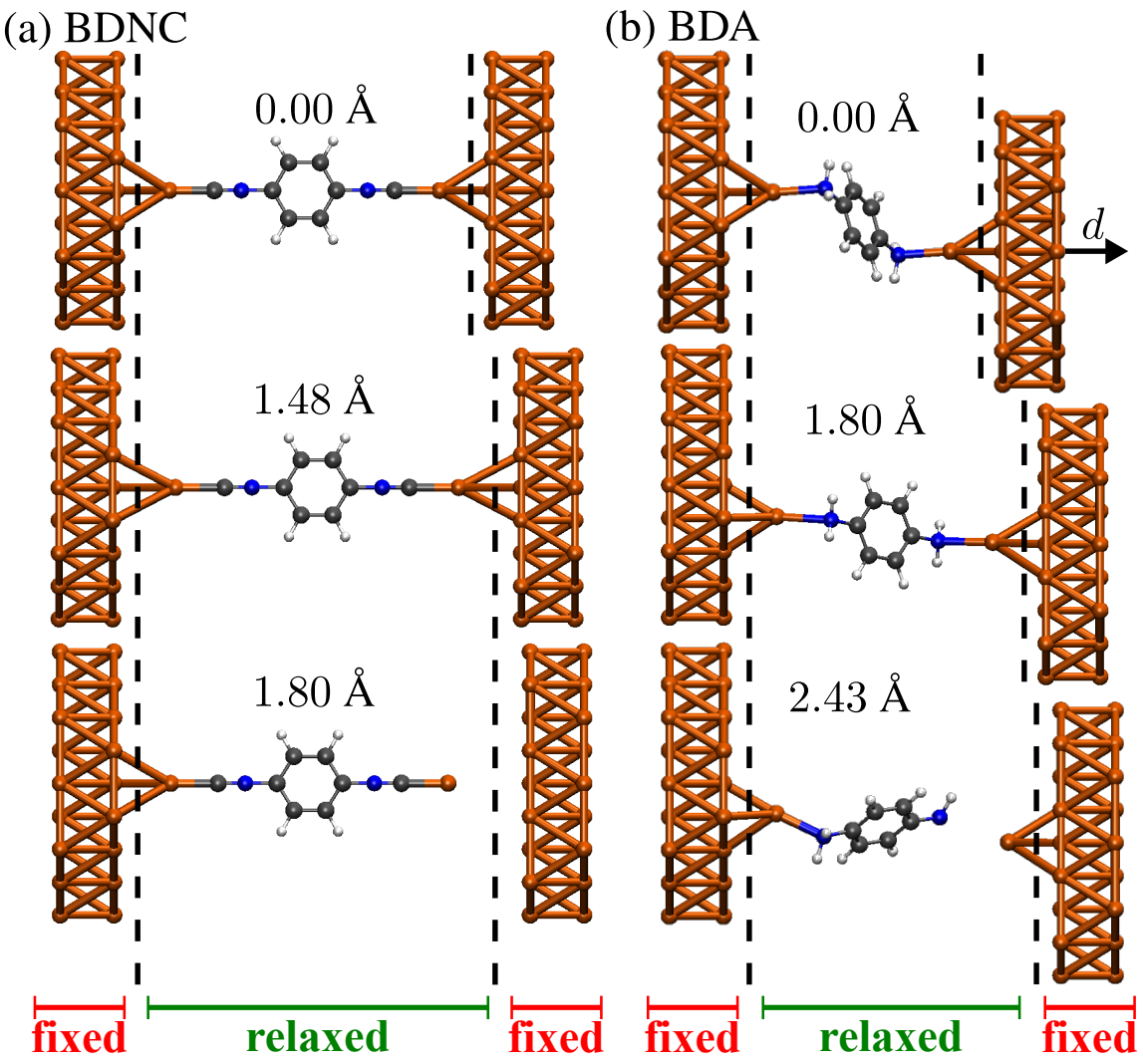

Figure 9.1: Junction geometries for BDNC (a) and BDA (b) at different electrode displacements, as indicated next to each geometry.

stronger to the left electrode. At that point the molecule takes the adatom from the surface. The picture is more complicated for the amine binding group. Here the electrodes are not exactly face to face because we find that the BDA molecule binds with an angle to the gold surface. Therefore, if the junctions are stretched, the gold adatom is dragged along the surface at a displacement of about 1.59 Å. That also induces a reorientation of the molecule inside the junction. The molecule rotates by about $15°$. The molecule develops a stronger bond to the left electrode if we increase the displacement to more than 2.43 Å. Here the distance between the gold and the amine group on the right side starts to increase faster than on the left side.

9.2 Electric properties of the stretched molecular junctions

In Fig. 9.2 (a) we show the energy-dependent transmission for small electrode displacements. Here the transmission is dominated by the first transmission channel. For both molecules the first channel contributes more than 80%.

Once again the molecules BDNC and BDA contain a benzene part that is coupled to the electrodes via different anchor groups. Having this picture in mind it is obvious to compare the transmission eigenchannels to the molecular orbitals of the isolated benzene. Here we find that the LUMO state of isolated benzene shows similar character as the

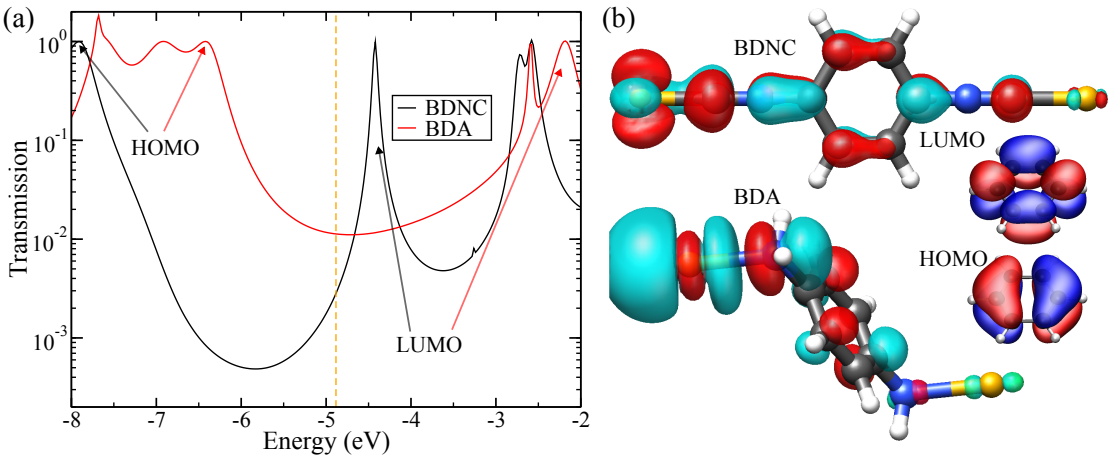

Figure 9.2: (a) Transmission as a function of energy is shown for BDNC and BDA molecular junctions with an electrode displacement of 0.212 Å. (b) Shows the first transmission channel at the Fermi energy and HOMO and LUMO of the isolated benzene.

first transmission channel of BDNC, as visible in Fig. 9.2 (b). The elastic transmission is shown in Fig. 9.2 (a). The transmission of BDNC at the Fermi energy is well described by a Lorentz-like shape centered around the resonance at about -4.5 eV.

For the Au-BDA-Au junction the transport is HOMO dominated since the HOMO resonance is about 1.5 eV below the Fermi energy and the LUMO is located about 2.5 eV above. Also the heating asymmetry of the Au-BDA-Au junction shows that the transport is HOMO dominated [11, 67]. If we analyze the dominant transmission eigenchannel of BDA we find that it is a superposition of HOMO and LUMO. That is attributed to the position of the Fermi energy between those two molecular orbitals and the fact that the LUMO resonance is comparably broad. Additionally, we find a sharp resonance at about -2.6 eV below the LUMO resonance in the energy dependent transmission of BDA. The origin of that resonance is the second LUMO of the benzene. Isolated benzene has a doubly degenerate LUMO. Here we find that the degeneracy splits in energy and one state couples to the electrodes, while the second LUMO at about -2.6 eV couples only weakly. That will result in a sharp resonance.

9.3 Heat transport properties

In the molecular junction heat can be transported via the electronic as well as via the phononic system. Here we present a comparison of both, but we neglect heat transport due to radiative processes. As discussed in Sec. 9.2 we calculate the energy-dependent electron transmission that allows us to describe the charge as well as the energy transport carried by electrons. Similarly we can calculate the energy-dependent phonon transmission. The phonons transport heat due to their intrinsic energy $\hbar\omega$. We can calculate their contribution to the heat conductance of the molecular junction. As described in Chap. 7.

In Fig. 9.3 (a) we show the phonon transmission of the molecular junctions Au-BDA-Au and Au-BDNC-Au. Here we see that the transmission vanishes for energies higher than 20 meV, due to the phonon density of states of gold. Below that cutoff energy we find about 230 modes of the full ECC geometry. The modes in this energy region are no localized modes, which can be described as a stretch of a single bond. These modes stand out due to the fact that almost each atom is displaced if we consider the corresponding eigenstate in the local displacement basis of the $\vec{Q}_i$, as discussed in Sec. 2.3.

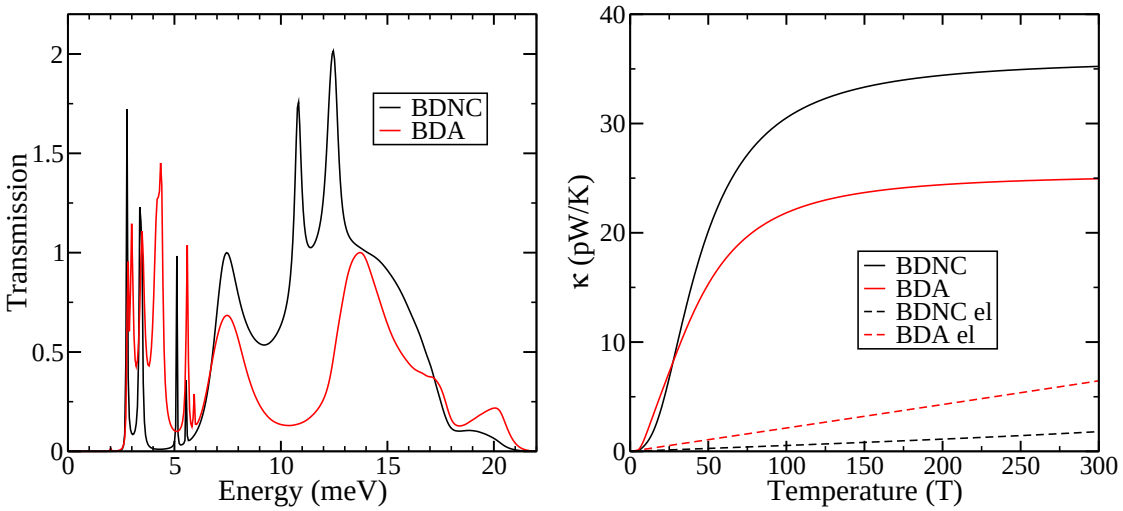

Figure 9.3: Phonon transmission (a) and heat conductance (b) for the molecular junctions with electrode displacement of 0.212 Å.

We use the phonon and electron transmission to calculate the heat conductance through the molecular junctions. For this we use Eqs. (2.50) and (2.48). The result of both is shown in Fig. 9.3 (b). The phonon contribution to the heat conductance saturates at about 200 K at a value of about 25 pW/K for BDA and about 35 pW/K for BDNC. At that temperature the heat conductance due to electrons is for BDA about a factor 6 smaller and for BDNC about a factor 30 smaller. In total the heat conductance calculated results in a high thermal resistance of $3.6 \cdot 10^{10}$ K/W for BDA and $2.8 \cdot 10^{10}$ K/W for BDNC, at about 200 K.

9.4 Electronic and phononic transport properties as a function of electrode displacement

In this section we analyze how the transport properties of the molecular junctions change if we displace the electrodes. That mimics the deformation of the contacts in molecular break junction measurements. At this point we restrict our analysis to the conductance plateau where the molecule is conducting and the electrode displacements are below the point of rupture of the contact. In Fig. 9.4 (a) we show first the conductance values of the molecular junctions BDA and BDNC. The conductance varies only weakly and is similar for both molecules, while the electrodes are separated. We find a conductance of $1 \cdot 10^{-2} G_0$ for BDA and $2 \cdot 10^{-3} G_0$ for BDNC.

We found that BDA drags a gold atom along the surface, at a electrode displacement of about 1.59 Å. At that point the BDA rotates slightly to adapt to the new electrode geometry. That reorientation does not affect the value of the conductance. But the Seebeck coefficient changes due to the reorientation. Therefore the power factor (ZT) of the molecular junction

$$ZT = \frac{GS^2T}{\kappa_{\text{el}} + \kappa_{\text{ph}}}, \tag{9.1}$$

changes at an electrode displacement of 1.59 Å. Here ZT increases due to the steeper slope of the electron transmission, that increases the thermopower S. Usually the resonances in the electron transmission become more narrow while increasing the electrode displacement. The reason for this is the decrease of the electronic coupling between the

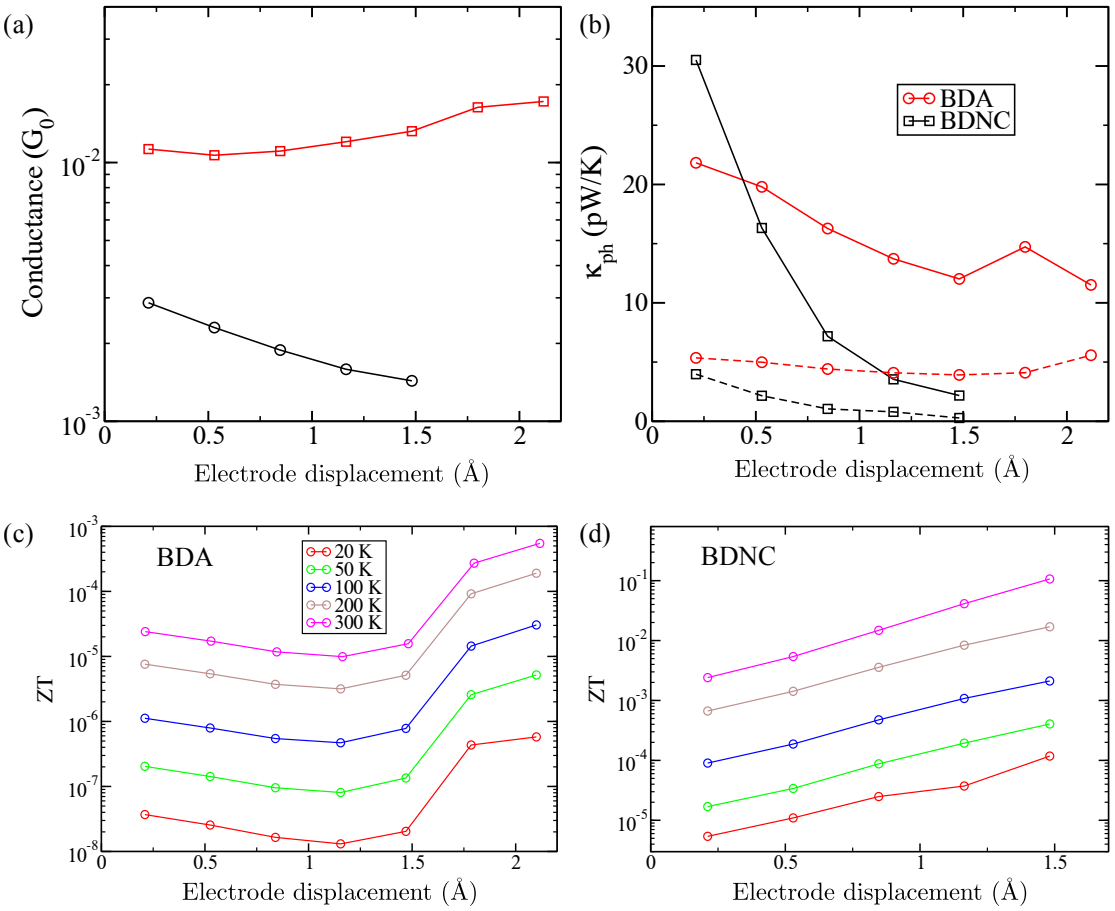

Figure 9.4: Conductance (a) and phonon heat conductance (b) as a functions of the electrode displacement, for 100 K (solid lines) and 20 K (dashed lines). (c,d) ZT for BDA and BDNC, respectively.

molecule and the metal electrodes with increasing displacement. For BDNC we find an almost linearly increasing ZT on the logarithmic plot.

9.5 Conclusions

In this chapter we presented our calculations on thermoelectric transport through molecular junctions with benzene derivatives. We analyzed two different anchor groups, namely amines and nitriles. For those we obtained different transport characteristics. While the thermopower is positive for the amines, the molecular energy levels were shifted with respect to the gold Fermi energy if nitrile anchors are used. The shifted energy levels were found to result in a negative thermopower with a rather big absolute value for the nitrile anchors.

We analyzed the heat transport properties of the molecular junctions and found that the phononic contributions are dominant as compared to those of the electrons. As we calculated the figure of merit, we found values of 0.1 at 300 K using nitrile anchors.

10 Summary

The focus of this thesis is on the theoretical description of electron and phonon transport in molecular electronics. Using the same level of ab-initio theory, we were able to determine the thermoelectric transport coefficients, including electron and phonon transport in the linear response regime. Additional inelastic effects on the electron transport due to vibrations were used to characterize the molecular junction configurations.

After giving a short introduction to the theory applied to compute transport properties in molecular electronics, we focused in Chap. 2, on the electron transport through molecular junctions in the first part of this thesis.

Supported by experiments, which were carried out in the group of Prof. Scheer (University of Konstanz), we analyzed the properties of the molecule-gold interface, as presented in Chap. 3. In this study we focused on the molecular end-groups thiol and amine, which are commonly used in experiments to attach a molecule to the metal electrodes. We found that using thiol anchors increases the breaking force by about a factor of two compared to amine anchors. Similarly the binding energy of the thiol-gold bond is twice as big as that of the amine-gold bond. Simulations of the stretching process, performed as close as possible to the realization in experiments, revealed that the thiol-gold bond deforms the electrodes upon stretching and is eventually strong enough to pull a gold atom from the electrodes. The deformation results in reorientations of the atoms in the electrode. It was found that this process causes kinks in the conductance traces. Our findings are in accordance with the measurements, where an analysis of the opening conductance traces reveals a kink feature for thiol-ended molecules that appears three times more often as compared to amines. The geometric properties of the molecular junctions were further analyzed by means of their vibrational modes. The measured and calculated inelastic electron tunneling spectra allow characterizing the vibrational modes that cause peaks in the spectra. In particular, we analyzed vibrations that are active at the molecule-metal interface.

In Chap. 4 we presented our investigations that concern π-stacked molecules. We analyzed the electron transport mechanism in the metal-molecule-metal configuration by means of the transmission eigenchannels. We found that the transport is dominated by the benzene π system of the paracyclophane molecule, while the linking ethan chains turned out to be of minor importance for the charge transport. Analyzing the inelastic electron tunneling spectra, we focused on vibrational modes with a particular character.

Namely, we focused on vibrations that displace the atoms of the benzene fragment, while the direction of displacement is within the plane of the benzene ring. The coupling of those modes to the current was found to be rather independent of the electrode geometry.

In Chap. 5 the inelastic electron tunneling spectra were analyzed in the case of destructive quantum interference. The fact that the elastic transmission is damped by quantum interference effects allows approximating the inelastic electron tunneling spectra. The basic physics is described by a tight binding model that includes the electronic π orbitals only. A comparison to a first principles calculation validates the approximations under certain conditions.

We closed our investigations on the electron transport in molecular electronics in Chap. 6, where we analyzed the crossover between coherent and incoherent transport observed for long molecular wires. The incoherence effects were included by means of Büttiker probes. That probes do not carry a current but they destroy the quantum mechanical phase information because they are coupled to the wires. The coupling strength between probe and conductor allows to tune the decoherence strength. We focused on the transition from tunneling to the ohmic regime using a linear chain. We found that the decoherence length depends exponentially on the coupling strength. The effect of finite temperature was found to be negligible in the off-resonant regime.

In the second part of this thesis we extended our theoretical investigations to heat transport through molecular junctions. We had to include phononic degrees of freedom in our analysis because phonons dominate the heat conductance. To calculate the heat conductance we used a consistent theory of electron and phonon transport. That allowed to explore the thermoelectric properties of molecular electronic devices. On that basis we were able to characterize the ability of single molecules to perform as thermoelectric heat converters.

In Chap. 7 we introduced our newly developed first principles scheme to describe phonon transport. Similarly as in the case of the electron transport, we used the Greens function scheme to describe the phonon heat transport. To obtain the phononic as well as the electronic structure, we applied density functional theory as implemented in TURBOMOLE. In case of atomic wires we compared the ab-initio results to a tight binding scheme and found reasonable agreement. While the heat conductance of the full calculations showed an even-odd effect, that feature was not recovered by the simple tight binding scheme.

In Chap. 8 we investigated the heat transport through π-stacked molecules. The basic idea is that the phonon transport through the molecular system is blocked because of the properties of the stacking mechanism. This expectation is based on the assumption that the stacking force could be described by a very low spring constant. Our findings for the paracyclophanes revealed a phonon heat conductance that is about a factor of 5 higher as compared to the electronic contribution, assuming a temperature of 50 K. We predict that molecular devices which include paracyclophanes should show a low figure of merit.

In the last Chap. 9 of this thesis we discussed the thermoelectric properties of benzene molecules, coupled via their para position to the electrodes using two different anchor groups. We found a heat conductance for the covalently bonded molecules that is of the same order of magnitude as for the direct π electron binding position, in case of the paracyclophane molecules. We analyzed the heat transport properties of those junctions under the mechanical strain caused by electrode displacements. We found that mechanical strain tends to suppress the phononic heat conductance.

On this basis, we could further analyze the thermoelectric potential of molecular elec-

tronic devices. In this respect we can tune the thermopower by means of chemical gating mechanisms. A second point is to suppress the heat transport due to phonons by using a big mass ratio between lead atoms and those of the molecular components. In this respect junction geometries like gold-H_2-gold might be promising candidates.

Bibliography

[1] G. Binnig, H. Rohrer, C. Gerber, and E. Weibel, Phys. Rev. Lett. **49**, 57 (1982).

[2] G. Binnig, C. F. Quate, and C. Gerber, Phys. Rev. Lett. **56**, 930 (1986).

[3] A. Aviram and M. A. Ratner, Chem. Phys. Lett. **29**, 277 (1974).

[4] G. Rubio, N. Agraït, and S. Vieira, Phys. Rev. Lett. **76**, 2302 (1996).

[5] H. Ohnishi, Y. Kondo, and K. Takayanagi, Nature **395**, 780 (1998).

[6] T. Kizuka, Phys. Rev. B **77**, 155401 (2008).

[7] B. Xu and N. J. Tao, Science **301**, 1221 (2003).

[8] M. A. Reed, C. Zhou, C. J. Muller, T. P. Burgin, and J. M. Tour, Science **278**, 252 (1997).

[9] J. M. van Ruitenbeek, A. Alvarez, I. Piñeyro, C. Grahmann, P. Joyez, M. H. Devoret, D. Esteve, and C. Urbina, Rev. Sci. Instrum. **67**, 108 (1996).

[10] P. Reddy, S. Y. Jang, R. A. Segalman, and A. Majumdar, Science **315**, 1568 (2007).

[11] W. Lee, K. Kim, W. Jeong, L. A. Zotti, F. Pauly, J. C. Cuevas, and P. Reddy, Nature **498**, 209 (2013).

[12] F. Pauly, J. K. Viljas, U. Huniar, M. Häfner, S. Wohlthat, M. Bürkle, J. C. Cuevas, and G. Schön, New J. Phys. **10**, 125019 (2008).

[13] M. Bürkle, J. K. Viljas, T. J. Hellmuth, E. Scheer, F. Weigend, G. Schön, and F. Pauly, Phys. Status Solidi B **250**, 2468 (2013).

[14] J. K. Viljas, J. C. Cuevas, F. Pauly, and M. Häfner, Phys. Rev. B **72**, 245415 (2005).

[15] J. C. Cuevas and E. Scheer, *Molecular Electronics: An Introduction to Theory and Experiment*, edited by M. Reed (World Scientific Publishing Company, 2010).

[16] F. Giustino, *Materials Modelling using Density Functional Theory: Properties and Predictions* (Oxford University Press, 2014).

[17] P. Hohenberg and W. Kohn, Phys. Rev. **136**, B864 (1964).

[18] R. G. Parr and W. Yang, *Density-Functional Theory of Atoms and Molecules* (Oxford University Press, 1989).

[19] R. M. Dreizler and E. K. U. Gross, *Density Functional Theory: An Approach to the Quantum Many-Body Problem* (Springer-Verlag, 1990).

[20] A. Szabo and N. S. Ostlund, *Modern Quantum Chemistry: Introduction to Advanced Electronic Structure Theory* (Dover Publications, Inc., 1996).

[21] W. Koch and M. C. Holthausen, *A Chemist's Guide to Density Functional Theory* (WILEY-VCH Verlag, 2002).

[22] M. Born and J. R. Oppenheimer, Ann. Phys. **84**, 457 (1927).

[23] T. Kato, Comm. Pure Appl. Math. **10**, 151 (1957).

[24] R. Ahlrichs, M. Bär, M. Häser, H. Horn, and C. Kölmel, Chem. Phys. Lett. **162**, 165 (1989).

[25] N. Mingo and L. Yang, Phys. Rev. B **68**, 245406 (2003).

[26] T. Yamamoto and K. Watanabe, Phys. Rev. Lett. **96**, 255503 (2006).

[27] J.-S. Wang, J. Wang, and J. T. Lü, EPJ B **62**, 381 (2008).

[28] U. Sivan and Y. Imry, Phys. Rev. B **33**, 551 (1986).

[29] G. J. Snyder and E. S. Toberer, Nat. Mater. **7**, 105 (2008).

[30] Y. Kim, H. Song, F. Strigl, H.-F. Pernau, T. Lee, and E. Scheer, Phys. Rev. Lett. **106**, 196804 (2011).

[31] A. D. Becke, Phys. Rev. A **38**, 3098 (1988).

[32] J. P. Perdew, Phys. Rev. B **33**, 8822 (1986).

[33] F. Weigend and R. Ahlrichs, Phys. Chem. Chem. Phys. **7**, 3297 (2005).

[34] G. Rubio-Bollinger, S. R. Bahn, N. Agraït, K. W. Jacobsen, and S. Vieira, Phys. Rev. Lett. **87**, 026101 (2001).

[35] C. Fiolhais, F. Nogueira, and M. A. Marques, *A Primer in Density Functional Theory* (2003).

[36] S. Y. Quek, L. Venkataraman, H. J. Choi, S. G. Louie, M. S. Hybertsen, and J. B. Neaton, Nano Lett. **7**, 3477 (2007).

[37] R. B. Pontes, A. R. Rocha, S. Sanvito, A. Fazzio, and A. J. R. da Silva, ACS Nano **5**, 795 (2011).

[38] M. Strange, C. Rostgaard, H. Häkkinen, and K. S. Thygesen, Phys. Rev. B **83**, 115108 (2011).

[39] C. A. Martin, D. Ding, H. S. J. van der Zant, and J. M. van Ruitenbeek, New J. Phys **10**, 065008 (2008).

[40] Y. Kim, T. J. Hellmuth, M. Bürkle, F. Pauly, and E. Scheer, ACS Nano **5**, 4104 (2011).

[41] P. K. Hansma, Phys. Rep. **30**, 145 (1977).

[42] J. Klein, A. Léger, M. Belin, D. Défourneau, and M. J. L. Sangster, Phys. Rev. B **7**, 2336 (1973).

[43] H. Song, Y. Kim, Y. H. Jang, H. Jeong, M. A. Reed, and T. Lee, Nature **462**, 1039 (2009).

[44] M. Paulsson, C. Krag, T. Frederiksen, and M. Brandbyge, Nano Lett. **9**, 117 (2009).

[45] W. Wang, T. Lee, I. Kretzschmar, and M. A. Reed, Nano Lett. **4**, 643 (2004).

[46] J. G. Kushmerick, J. Lazorcik, C. H. Patterson, R. Shashidhar, D. S. Seferos, and G. C. Bazan, Nano Lett. **4**, 639 (2004).

[47] C. R. Arroyo, T. Frederiksen, G. Rubio-Bollinger, M. Vélez, A. Arnau, D. Sánchez-Portal, and N. Agraït, Phys. Rev. B **81**, 075405 (2010).

[48] D. P. Long, J. L. Lazorcik, B. A. Mantooth, M. H. Moore, M. A. Ratner, A. Troisi, Y. Yao, J. W. Ciszek, J. M. Tour, and R. Shashidhar, Nat. Mater. **5**, 901 (2006).

[49] N. Okabayashi, M. Paulsson, H. Ueba, Y. Konda, and T. Komeda, Nano Lett. **10**, 2950 (2010).

[50] D. P. Long and A. Troisi, J. Am. Chem. Soc. **129**, 15303 (2007).

[51] J. Jiang, M. Kula, W. Lu, and Y. Luo, Nano Lett. **5**, 1551 (2005).

[52] G. C. Solomon, A. Gagliardi, A. Pecchia, T. Frauenheim, A. Di Carlo, J. R. Reimers, and N. S. Hush, J. Chem. Phys. **124**, 094704 (2006).

[53] A. Pecchia, A. Di Carlo, A. Gagliardi, S. Sanna, T. Frauenheim, and R. Gutierrez, Nano Lett. **4**, 2109 (2004).

[54] M. Bai, J. Liang, L. Xie, S. Sanvito, B. Mao, and S. Hou, J. Chem. Phys. **136**, 104701 (2012).

[55] Y. Morisaki, S. Ueno, A. Saeki, A. Asano, S. Seki, and Y. Chujo, Chem. Eur. J. **18**, 4216 (2012).

[56] G. C. Solomon, J. Vura-Weis, C. Herrmann, M. R. Wasielewski, and M. A. Ratner, J. Phys. Chem. B **114**, 14735 (2010).

[57] G. C. Solomon, C. Herrmann, J. Vura-Weis, M. R. Wasielewski, and M. A. Ratner, J. Am. Chem. Soc. **132**, 7887 (2010).

[58] A. Mishchenko, D. Vonlanthen, V. Meded, M. Bürkle, C. Li, I. V. Pobelov, A. Bagrets, J. K. Viljas, F. Pauly, F. Evers, M. Mayor, and T. Wandlowski, Nano Lett. **10**, 156 (2010).

[59] L.-L. Lin, J.-C. Leng, X.-N. Song, Z.-L. Li, Y. Luo, and C.-K. Wang, J. Phys. Chem. C **113**, 14474 (2009).

[60] S. T. Schneebeli, M. Kamenetska, Z. Cheng, R. Skouta, R. A. Friesner, L. Venkataraman, and R. Breslow, J. Am. Chem. Soc. **133**, 2136 (2011).

[61] S. Grimme, J. Antony, S. Ehrlich, and H. Krieg, J. Chem. Phys. **132**, 154104 (2010).

[62] D. Henseler and G. Hohlneicher, J. Phys. Chem. A **102**, 10828 (1998).

[63] S. Grimme, Chem. Eur. J. **10**, 3423 (2004).

[64] F. Pauly, J. K. Viljas, J. C. Cuevas, and G. Schön, Phys. Rev. B **77**, 155312 (2008).

[65] M. Bürkle, J. K. Viljas, D. Vonlanthen, A. Mishchenko, G. Schön, M. Mayor, T. Wandlowski, and F. Pauly, Phys. Rev. B **85**, 075417 (2012).

[66] M. Bürkle, L. A. Zotti, J. K. Viljas, D. Vonlanthen, A. Mishchenko, T. Wandlowski, M. Mayor, G. Schön, and F. Pauly, Phys. Rev. B **86**, 115304 (2012).

[67] L. A. Zotti, M. Bürkle, F. Pauly, W. Lee, K. Kim, W. Jeong, Y. Asai, P. Reddy, and J. C. Cuevas, New J. Phys. **16**, 015004 (2014).

[68] T. Markussen, C. Jin, and K. S. Thygesen, Phys. Status Solidi B **250**, 2394 (2013).

[69] M. Paulsson and M. Brandbyge, Phys. Rev. B **76**, 115117 (2007).

[70] T. Markussen, R. Stadler, and K. S. Thygesen, Nano Lett. **10**, 4260 (2010).

[71] C. M. Guedon, H. Valkenier, T. Markussen, K. S. Thygesen, J. C. Hummelen, and S. J. van der Molen, Nat. Nanotechnol. **7**, 305 (2012).

[72] J. Lykkebo, A. Gagliardi, A. Pecchia, and G. C. Solomon, J. Chem. Phys. **141**, 124119 (2014).

[73] P. Sautet and C. Joachim, Chem. Phys. Lett. **153**, 511 (1988).

[74] D. Rai, O. Hod, and A. Nitzan, J. Phys. Chem. C **114**, 20583 (2010).

[75] D. Q. Andrews, G. C. Solomon, R. H. Goldsmith, T. Hansen, M. R. Wasielewski, R. P. V. Duyne, and M. A. Ratner, J. Phys. Chem. C **112**, 16991 (2008).

[76] F. Haupt, T. Novotný, and W. Belzig, Phys. Rev. B **82**, 165441 (2010).

[77] J. Lykkebo, A. Gagliardi, A. Pecchia, and G. C. Solomon, ACS Nano **7**, 9183 (2013).

[78] R. Yamada, H. Kumazawa, S. Tanaka, and H. Tada, Appl. Phys. Express **2**, 025002 (2009).

[79] S. Datta, *Electronic Transport in Mesoscopic Systems* (Cambridge University Press, Cambridge, 1997).

[80] D. Nozaki, C. Gomes da Rocha, H. M. Pastawski, and G. Cuniberti, Phys. Rev. B **85**, 155327 (2012).

[81] C. J. Cattena, R. A. Bustos-Marún, and H. M. Pastawski, Phys. Rev. B **82**, 144201 (2010).

[82] J. L. D'Amato and H. M. Pastawski, Phys. Rev. B **41**, 7411 (1990).

[83] V. Mujica, M. Kemp, and M. A. Ratner, J. Chem. Phys. **101**, 6856 (1994).

[84] M. Büttiker, Phys. Rev. B **40**, 3409 (1989).

[85] D. Visontai, I. M. Grace, and C. J. Lambert, Phys. Rev. B **81**, 035409 (2010).

[86] J. K. Viljas, F. Pauly, and J. C. Cuevas, Phys. Rev. B **77**, 155119 (2008).

[87] TURBOMOLE, is a development of University of Karlsruhe and Forschungszentrum Karlsruhe, 1989-2007, TURBOMOLE GmbH, since 2007; available from `http://www.turbomole.com`.

[88] P. Deglmann, F. Furche, and R. Ahlrichs, Chem. Phys. Lett. **362**, 511 (2002).

[89] P. Deglmann and F. Furche, J. Chem. Phys. **117**, 9535 (2002).

[90] Y. Xue, S. Datta, and M. A. Ratner, J. Chem. Phys. **115**, 4292 (2001).

[91] J. Taylor, H. Guo, and J. Wang, Phys. Rev. B **63**, 245407 (2001).

[92] M. Brandbyge, J.-L. Mozos, P. Ordejón, J. Taylor, and K. Stokbro, Phys. Rev. B **65**, 165401 (2002).

[93] K. S. Thygesen, M. V. Bollinger, and K. W. Jacobsen, Phys. Rev. B **67**, 115404 (2003).

[94] F. Evers, F. Weigend, and M. Koentopp, Phys. Rev. B **69**, 235411 (2004).

[95] G. C. Solomon, J. R. Reimers, and N. S. Hush, J. Chem. Phys. **121**, 6615 (2004).

[96] A. R. Rocha, V. M. García-Suárez, S. Bailey, C. Lambert, J. Ferrer, and S. Sanvito, Phys. Rev. B **73**, 085414 (2006).

[97] J. W. Lynn, H. G. Smith, and R. M. Nicklow, Phys. Rev. B **8**, 3493 (1973).

[98] F. Guinea, C. Tejedor, F. Flores, and E. Louis, Phys. Rev. B **28**, 4397 (1983).

[99] N. W. Ashcroft and N. D. Mermin, *Solid state physics* (New York, 1976).

[100] M. Bürkle, T. J. Hellmuth, F. Pauly, and Y. Asai, preprint (2015).

List of abbreviations

BDA 1,4-benzenediamine.

BDNC 1,4-benzenediisonitrile.

DFT density functional theory.

DOS density of states.

ECC extended central cluster.

GGA generalized gradient approximation.

HK Hohenberg-Kohn.

HOMO highest occupied molecular orbital.

IETS inelastic electron tunneling spectroscopy.

KS Kohn-Sham.

LDA local density approximation.

LUMO lowest unoccupied molecular orbital.

MCBJ mechanically controllable break-junction.

ODA octane-diamine.

ODT octane-dithiol.

TB tight-binding.